

# **Optical and Magnetic Investigations on Lanthanide-Doped Nanoparticles as Dual Imaging Contrast Agents**

Inaugural-Dissertation

to obtain the academic degree

Doctor rerum naturalium (Dr. rer. nat.)

submitted to the Department of Biology, Chemistry, and Pharmacy

of Freie Universität Berlin

by

**Shih-Hao Kung**

from Taipei, Taiwan

February 2015

The research work presented herein was carried out in the time period August 2009 - July 2013, and September 2014 – February 2015 in the research group of Prof. Dr. E. Rühl at the Institute of Chemistry and Biochemistry of the Freie Universität Berlin.

1<sup>st</sup> Reviewer: Prof. Dr. E. Rühl

2<sup>nd</sup> Reviewer: Prof. Dr. C. Graf

Date of defense: 24. 04. 2015

# Acknowledgement

I sincerely thank my supervisor Prof. Dr. E. Rühl for offering me the opportunity to work in his supportive research group. His calmness and efficiency in conducting all kinds of issues has given me much help. I deeply thank him for his efforts on reviewing my thesis manuscript.

I would like to express my special thanks to Prof. Dr. C. Graf who gave me the research topic of this thesis. Her opinions always clarify the situation when I get confused in the research. Her efforts in reviewing my thesis manuscript are deeply appreciated.

I would like to acknowledge people who were involved in the different characterization measurements of this thesis. I thank Dr. H. Renz (Institute of Oral Structural Biology in Charité) for his assistance in the TEM measurements, both Dr. K. Siemensmeyer (Department of Quantum Phenomena in Novel Materials in HZB) and Dr. F. Wiekhorst (Division of Medical Physics and Metrological Information Technology in PTB) for their support in the SQUID characterizations, Dr. L. Schröder and Dr. C. Witte (Leibniz-Institut für Molekulare Pharmakologie im Forschungsverbund Berlin e.V.) for their help in the relaxometry measurements, Dr. C. Boeglin (Institut de Physique et Chimie des Matériaux de Strasbourg) and Prof. Dr. F. Nolting (Paul Scherrer Institute) for their assistance in the X-ray absorption measurements, D. Klier and Prof. Dr. M. Kumke for the cooperation in the upconversion measurements, and G. Bukalis as well as Dr. D. Alber for the neutron activation analysis data.

My thanks also go to people who shared the same group, the same lab or the same office during my PhD studies, especially Suguna, Valerie, Peter, Benni, Daniel, Xin, Yan, Beate and Christian. They have offered me a pleasant working atmosphere and useful discussions. My special thanks also go to Mr. S. Thierbach for his useful suggestions and constant support in the lab equipments issues.

Finally, I would like to thank my parents, my brother and my husband for their unlimited support and love.

# Contents

<b>Chapter 1 Introduction .....</b>	<b>1</b>
<b>Chapter 2 Research Background.....</b>	<b>4</b>
2.1 Nanoparticles .....	4
2.1.1 Definition of Nanoparticles .....	4
2.1.2 Magnetic Nanoparticles .....	4
2.1.3 Fluorescent Nanoparticles .....	7
2.2 Methods .....	10
2.2.1 Relaxometry Measurements .....	10
2.2.2 Fluorescence Spectroscopy and Upconversion Measurements .....	15
2.2.3 Magnetic Property Measurement System.....	25
2.2.4 X-ray Absorption Spectroscopy and X-ray Magnetic Circular Dichroism Spectroscopy (XAS and XMCD).....	32
<b>Chapter 3 Experimental Details.....</b>	<b>39</b>
3.1 Characterization Methods.....	39
3.1.1 Transmission Electron Microscopy .....	39
3.1.2 Relaxometry Measurements .....	39
3.1.3 Fluorescence Spectroscopy and Upconversion Measurements .....	40
3.1.4 Magnetic Property Measurement System .....	40
3.1.5 X-ray Absorption Spectroscopy and X-ray Magnetic Circular Dichroism Spectroscopy.....	41
3.2 Preparation of Nanoparticles .....	42

3.2.1 General Procedures for Nanoparticles and Ligands Preparation .....	42
3.2.2 Chemicals .....	42
3.2.3 Synthesis of Lanthanide Oxide Nanoparticles .....	43
3.2.4 Synthesis of Lanthanides Fluoride Nanoparticles .....	44
3.2.5 Synthesis of PEO-monophosphonate Ligands.....	44
3.2.5.1 Synthesis of $\text{Me}(\text{OCH}_2\text{CH}_2)_{11}\text{SO}_3\text{C}_6\text{H}_4\text{Me}_p$ .....	44
3.2.5.2 Synthesis of $\text{Me}(\text{OCH}_2\text{CH}_2)_{11}\text{NHMe}$ .....	45
3.2.5.3 Synthesis of $\text{Me}(\text{OCH}_2\text{CH}_2)_{11}\text{NMeCH}_2\text{PO}(\text{OH})_2$ .....	45
3.2.6 Synthesis of PEO-diphosphonate Ligands.....	46
3.2.6.1 Synthesis of $\text{Me}(\text{OCH}_2\text{CH}_2)_{11}\text{NH}_2$ .....	46
3.2.6.2 Synthesis of $\text{Me}(\text{OCH}_2\text{CH}_2)_{11}\text{N}(\text{CH}_2\text{PO}(\text{OH})_2)_2$ .....	46
3.2.7 Ligand Exchange .....	47

## **Chapter 4 Results and Discussions ..... 48**

4.1 Magnetic Studies on $\text{Gd}_2\text{O}_3$ Nanoparticles .....	48
4.1.1 X-ray Absorption Spectra Studies.....	49
4.1.2 X-ray Magnetic Circular Dichroism Spectra Studies .....	53
4.1.3 Superconducting Quantum Interference Device Studies.....	62
4.1.4 Conclusions .....	68
4.2 Magnetic Studies on Lanthanide-Doped $\text{NaGdF}_4$ Nanoparticles.....	69
4.2.1 Superconducting Quantum Interference Device Studies.....	69
4.2.2 Relaxometry Measurements .....	73
4.2.3 Conclusions .....	77
4.3 Optical Studies on Eu-, Er-, and Yb-Doped $\text{NaGdF}_4$ Nanoparticles	78
4.3.1 Eu Ions in $\text{NaGdF}_4$ Nanoparticles .....	78
4.3.2 Eu and Er Ions in $\text{NaGdF}_4$ Nanoparticles .....	84
4.3.3 Variation of Dopants .....	94
4.3.4 Size Effects.....	99

4.3.5 Annealing Effects.....	108
4.3.6 Conclusions .....	116
<b>Chapter 5 Conclusions .....</b>	<b>120</b>
<b>Summary .....</b>	<b>i</b>
<b>Zusammenfassung .....</b>	<b>iii</b>
<b>References.....</b>	<b>v</b>

# Chapter 1

## Introduction

The fast developing and advancing life sciences including clinical diagnosis require corresponding progress in analytical techniques. Therefore, there is a growing demand to create a series of easy to use, sensitive, and reliable analytical approaches which allow one single sample to be measured by different analytical approaches so that information in different aspects of the sample can be obtained. Fluorescence imaging and magnetic resonance imaging (MRI) are two of the most frequently applied techniques in clinical studies for the directly scanning of animal bodies. Due to different image production mechanisms, the fluorescence imaging technique is frequently used for targeting various parts of organisms, whereas the MRI technique is able to probe details of soft tissues. Therefore, multifunctional imaging agents that can be applied in both fluorescence imaging as well as magnetic resonance imaging are of great interest.

Lanthanide nanoparticles are potential candidates for multifunctional imaging agents because they can be fluorescent which is applicable in fluorescence imaging to localize target cells, and they can also be magnetic which can be used to alter relaxation times of proton spins in magnetic resonance imaging to enhance contrasts in images.<sup>1,2</sup> The fluorescent and magnetic properties of lanthanide nanoparticles depend on the lanthanide elements that are chosen to be included within the particles.

When Eu-containing nanoparticles are applied as luminescent nanoparticles, they have been regarded as efficient luminescence agents especially for tumor detections by *in vivo* molecular imaging using X-ray luminescence optical tomography (XLOT).<sup>3,4</sup> The sufficient signal-to-noise ratio can be obtained from XLOT despite the fact that only a relatively small number of photons can be generated.<sup>3</sup> Er- and Yb- containing nanoparticles are used as upconversion materials in bio-imaging.<sup>5</sup> They are receiving enormous attention because they can absorb photons in the near infrared regime and emit photons in the visible regime. The advantages of near infrared light as excitation

light sources for fluorescent particles in biological systems are not only their ability to penetrate deep into tissues without causing severe damages, but also to reduce autofluorescence from biological systems since biological species have a limited ability to absorb the near infrared light. As a result, the signal-to-noise ratio of such approach is enhanced compared to those materials which are excited by ultraviolet or visible light.<sup>6</sup> In addition, due to the electronic structure of lanthanides, they show sharp and intense fluorescence emissions and long lifetimes compared to organic dyes and quantum dots.<sup>6</sup> Therefore, lanthanides are promising candidates for being a powerful fluorescence source.  $Gd^{3+}$  ions having seven unpaired valence electrons are regarded as a potential  $T_1$ -weighted MRI contrast agent. Nowadays, Gd-chelates are used as MRI contrast agents in clinical diagnostics, but they show limitations at long-term tracking in organisms because of their low molecular weight which causes short circulation times. To increase the local contrast and relaxivity, Gd-containing nanoparticles have been regarded as a new class of  $T_1$ -weighted contrast agents since one nanoparticle easily contains thousands of Gd ions which give rise to a high relaxivity.<sup>7-9</sup>

The aim of this thesis is to develop a new class of multifunctional nanoparticles which can be used not only as MRI contrast agents but also fluorescent imaging agents that can be excited by both ultraviolet and near infrared radiations. Therefore, nanoparticles containing Gd, Eu, Er, and Yb are investigated. There are two main parts in the work besides the synthesis of the particles, which concern the characterization of their magnetic and optical properties.

The magnetic studies are further divided into two parts. The first part focuses on annealing effects of Eu-doped  $Gd_2O_3$  nanoparticles. Two samples have been prepared: the unannealed sample and an annealed one. The annealed sample has been obtained from an additional annealing process of the unannealed one. The two samples have been investigated by the method of X-ray absorption spectra which provide elemental information by probing the local electronic structure at the Eu and Gd absorption edges. Furthermore, X-ray magnetic circular dichroism spectra provide local magnetic properties of Eu and Gd, and superconducting quantum interference device (SQUID) gives the magnetic contribution over the complete sample. The second part confirms annealing effects on the Er-, Eu-, and Yb-doped  $NaGdF_4$  nanoparticles by SQUID

studies. In addition, a short comparison on the relaxometry measurements between Magnevist<sup>®</sup> and Er-, Eu-, and Yb-doped NaGdF<sub>4</sub> nanoparticles is presented, so that the particles developed in this work are compared to a commercial sample.

The optical studies are focused on the Er-, Eu-, and Yb-doped NaGdF<sub>4</sub> nanoparticles. Firstly, two samples, NaEuF<sub>4</sub> and Eu-doped NaGdF<sub>4</sub> nanoparticles, are compared to understand the influence of the diluted Eu content regarding their fluorescent properties. Secondly, the nanoparticle systems are characterized regarding both fluorescence (downconversion) and upconversion aspects by studying Er-, Eu-, and Yb-doped NaGdF<sub>4</sub> nanoparticles. Thirdly, the influence of the variation of dopant ratios, the annealing, and the particle size of Er-, Eu-, and Yb-doped NaGdF<sub>4</sub> nanoparticles are investigated regarding the downconversion and upconversion efficiencies as well as their excited state lifetimes.

# Chapter 2

## Research Background

### 2.1 Nanoparticles

#### 2.1.1 Definition of Nanoparticles

Nanoparticles are particles with sizes ranging between 1 and 100 nm in at least one of the three dimensions. They have a large surface-to-volume ratio, a large proportion of atoms at the surface, and an ability to possess quantum confinement effects. Due to these characteristics, nanoparticles have distinguished chemical and physical properties compared to bulk materials.<sup>10</sup>

#### 2.1.2 Magnetic Nanoparticles

The most extensively studied magnetic nanoparticles contain metals, rare earth metals, magnetic alloys, or magnetic oxides.<sup>11</sup> They are applied in a wide range of applications, such as catalysis,<sup>12</sup> magnetic fluids,<sup>13</sup> magnetic resonance imaging,<sup>2</sup> and data storage.<sup>14</sup>

In most of applications, magnetic nanoparticles can be applied efficiently with a size range between 10 and 20 nm.<sup>15</sup> An important issue of nanoparticles in this size range is their intrinsic stability as a function of time which may lead to particle aggregation. This is mostly because small particles tend to reduce their surface-to-volume ratio in order to reach their thermal equilibrium state. To avoid inhomogeneous physical and chemical properties of magnetic nanoparticles which are likely dependent on the particles size due to quantum confinement effects, it is usually important to chemically stabilize these particles by grafting or coating the particle surface with organic or inorganic species so that the aggregation is successfully prevented.

When mentioning featured properties of magnetic nanoparticles, there are two main types of effects which lead to significant properties of magnetic nanoparticles. One is finite-size effects and the other one is surface effects.<sup>15</sup>

Two of the most well-known finite-size effects of magnetic nanoparticles are the single domain effect and the superparamagnetic effect which are briefly summarized in the following paragraph.<sup>15</sup>

Firstly, particles below their critical diameter have a single domain state. The critical diameter is usually in the nanometer range and is material-dependent. A single domain state is determined by the balance between the magnetostatic energy and the domain-wall energy. The magnetostatic energy is the magnetic potential energy which is generated due to the classical interactions between magnetic dipoles when a magnetic species is present in a magnetic field. The magnetostatic energy must be minimized in order to minimize the total magnetic energy. This can be achieved by decreasing the external demagnetizing field by dividing the material into domains. There is a critical volume if the sample size is reduced. As the domain volume is below the critical volume, it requires more energy to create a domain wall than to support the external magnetostatic energy of the single-domain state. Thus, single domain particles occur when their volume is below their critical size. All spins in the single domain particles are aligned in the same direction, and the magnetization of the particles will be reversed by spin rotations. Therefore, the single domain particles have a high coercivity.<sup>16</sup>

Secondly, ferromagnetic or ferrimagnetic particles which are smaller than their corresponding critical size and have a temperature higher than their corresponding blocking temperature are superparamagnetic. In sufficiently small nanoparticles, the direction of magnetization flips randomly under the influence of the temperature. The period of time between two flips is called the Néel relaxation time. If the time used to measure the magnetization of nanoparticles is longer than the Néel relaxation time in the absence of an external magnetic field, the magnetization of these nanoparticles appears to be zero in average. As a result, these particles are in a superparamagnetic state. In this state, an external magnetic field is able to magnetize these nanoparticles in

the same way as it is possible for a paramagnet, but the magnetic susceptibility of superparamagnetic particles is much larger than that of paramagnets.

A large proportion of atoms in a small particle are the surface atom. Therefore, surface and interface effects in nanoparticles are of great importance. For example, an oxidized-surface layer on a nanoparticle is possible to cause a reduction of magnetization; the surface anisotropy is able to alter the magnetic anisotropy in small particles.<sup>17</sup> In addition, surface coatings may also influence the magnetization of magnetic nanoparticles. A magnetically inert coating on magnetic nanoparticles can separate particles,<sup>18</sup> and avoids a cooperative magnetic switching among particles. Finally, organic ligands can alter the anisotropy and the magnetic moment of metal atoms on the surface.<sup>19</sup>

Useful magnetic nanoparticles with desired magnetic properties can be properly designed and produced when taking advantages of above mentioned effects on magnetic nanoparticles.

### 2.1.3 Fluorescent Nanoparticles

A number of fluorescence microscopy techniques enhance the possibility for distinguishing between different species and observing dynamic processes on the molecular level in medicinal and biological applications. Organic dyes are frequently applied as biolabeling agents or used to develop fluorescence sensing systems which can be investigated by fluorescence microscopy techniques.

However, organic dyes have many drawbacks when they are applied in such techniques. Their low absorption coefficients limit the detection sensitivity when the incoming excitation light is of insufficient intensity. There may be also a poor photobleaching resistance, which reduces the application of organic dyes due to the limited long-term stability. To overcome these drawbacks of organic dyes, fluorescent nanoparticles are regarded as potential candidates for the substitution of organic dyes in fluorescence microscopy.

It is already known that encapsulating organic dyes into a nanoparticle matrix is able to enhance the brightness of a fluorophore compared to a single dye molecule, since one nanoparticle may contain several organic dye molecules, which may also be more photostable in nanoparticle matrices.<sup>20</sup> Some nanoparticles, such as quantum dots, are intrinsically fluorescent and their sizes are in general in the nanoscale. Their small size provides an opportunity for the high signal-to-noise ratio response and the signal amplification for single molecular imaging and long-term tracking of biological molecules *in vivo* since their small size minimizes physical perturbations of living cells.<sup>20</sup> In addition, the potential of fluorescent nanoparticles to be applied in multicolor studies makes them even more attractive.<sup>21</sup>

There are two main types of fluorescent nanoparticles. One is intrinsically fluorescent nanoparticles, such as quantum dots, whereas the other is dye-doped fluorescent nanoparticles.

Quantum dots are semiconductor nanoparticles which are composed of atoms of the groups II and VI, III and V, or IV and VI in the periodic table. The particle size of

quantum dots is usually in the range of 2-10 nm and the fluorescence emission of quantum dots is size-dependent because of quantum confinement effects. An exciton is an electron-hole pair and the exciton bound energy is the energy quantum dots require for the fluorescence emission. When the particle size of semiconductor nanoparticles approaches the exciton Bohr radius, the exciton in the particles is confined so that the coulomb interaction energy which is size-dependent dominates the exciton bound energy of quantum dots. Therefore, the size-dependent exciton bound energy leads to size-dependent fluorescence emissions in quantum dots.<sup>22</sup> The fluorescence emission spectra of quantum dots are typically narrow and symmetric, and they usually have a broad excitation range and a large Stokes shift so that a single light source is able to excite multicolor quantum dots.<sup>23</sup> Quantum dots also have high extinction coefficients as well as strong fluorescence and these characteristics make them available to be applied in single molecule fluorescence studies and long-term tracking.<sup>21</sup>

Dye-doped fluorescent nanoparticles are usually composed of luminescent dye molecules which are encapsulated, embedded, or coated on the particle matrix, such as silica or polymer nanoparticles.<sup>21</sup> In comparison with the single dye molecule, the dye-doped nanoparticles can have higher amplified optical signals which enhance their analytical sensitivity. Also the nanoparticle matrix provides a chemically and mechanically stable environment which can protect the fluorescing dye molecules from the harsh surrounding environment. Such properties make dye-doped nanoparticles promising fluorescent labels in applications for bio-analysis and bioimaging.<sup>24</sup>

An alternative type of dye-doped nanoparticles for biolabeling studies is based on lanthanide-doped nanoparticles. Their fluorescent properties originate from their  $4f$  electrons which give the possibility of intra- $4f$  and  $4f-5d$  transitions. The color of these particles can be tuned by varying the dopants, such as Ce, Tb, Eu, Er, and Dy.<sup>25</sup> Generally, lanthanide-doped nanoparticles give sharp emission spectra and large Stokes shifts, i.e. the widths of their emission peaks are smaller than 10 nm and their Stokes shifts are usually larger than 150 nm. They exhibit a high photostability and high photobleaching resistance, which enable them for a convenient surface modification without altering their luminescence properties. Also, lanthanide-doped nanoparticles have long fluorescence lifetimes of up to milliseconds. The above mentioned

characteristics make these lanthanide-doped particles suitable for applications in biolabeling and imaging.<sup>24</sup>

## **2.2 Methods**

In this Section, basic principles of characterization methods used in this work are summarized.

### **2.2.1 Relaxometry Measurements**

#### **Magnetic resonance imaging<sup>26</sup>**

Magnetic resonance imaging is a technique which is based on the principles of nuclear magnetic resonance. It is used in medical diagnosis to take images inside the human body. Water, proteins, and fat are the main components of the human body, and consequently, about 63% of the human body is composed of hydrogen atoms when calculated in molar concentrations. Magnetic resonance imaging technique takes primarily advantage of the nuclear magnetic properties of hydrogen atoms to produce images.

A magnetic resonance imaging setup is composed of a superconducting magnet of 0.5-3 T in medical applications, three sets of gradient magnets, radio frequency coils, and a computer system.

Usually, the magnetic moments of the protons in the human body have random orientations. As a human body is placed in the magnetic field, the orientations of these magnetic moments all align parallel or anti-parallel to the magnetization direction depending on if the proton itself contains excess energy. The magnetic moments of the protons that align parallel to the direction of the magnetic field correspond to the lower energy state, whereas those aligning anti-parallel to the direction of the magnetic field correspond to the higher energy state. Therefore, more magnetic moments of the protons align parallel to the direction of magnetic field, and a net magnetization toward this direction results. This net magnetization is called longitudinal magnetization. Instead of being still, all hydrogen protons precess at Larmor frequency which is proportional to the strength of the magnetic field as well as the gyromagnetic ratio which is a

fundamental intrinsic physical constant for a material (See Figure 2.2.1 a). The larger the magnetic field which is applied on the hydrogen atoms, the faster they precess.

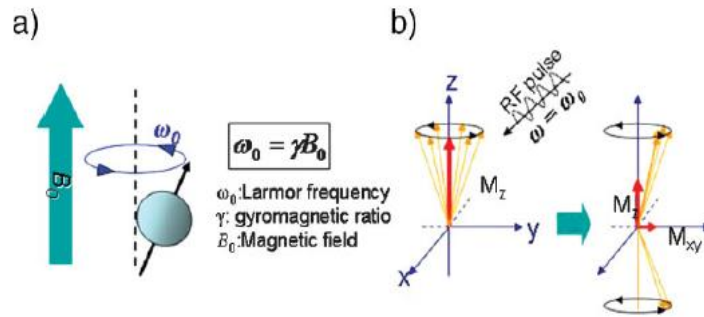


Figure 2.2.1: (a) Proton spins align parallel to the magnetic field, and precess at Larmor frequency. (b) Proton spins are stimulated by radio frequency pulse, and the net magnetization of proton spins goes from longitudinal direction (parallel to the magnetic field) to transverse direction when sufficient energy is absorbed by the measurement area.<sup>2</sup>

However, without the three sets of gradient magnets in the magnetic resonance imaging setup, only a total summation of spin magnetization is obtained, i.e. the contribution of each differently located proton magnets cannot be distinguished in a measurement cycle, because all proton magnets precess with the same frequency. In other words, the human body is measured as a whole magnet, and the differences between the different parts in the human body cannot be distinguished. To specify the contributions from differently located proton magnets in the human body, three set of gradient magnets are applied, along the x, y, and z axis. Two sets of the gradient magnet (x, z axis) are able to slightly adjust the magnitude of the magnetic field applied on the investigated region linearly, and proton magnets at different locations are influenced by the gradient magnets. Due to the different magnetic field, proton magnets at different locations are able to precess at their Larmor frequency accordingly. In addition, a set of gradient magnets (y axis) is applied shortly to the investigated region in order to alter phases of proton magnets. Owing to different precessions and phases of hydrogen protons, it is possible to orientate the contribution of differently located proton magnets in a three-dimensional

measurement. The three gradient magnets give the possibility for magnetic resonance imaging measurement to map hydrogen contributions in the human body.

Moreover, the signal of each hydrogen proton cannot be obtained directly because the magnetic moments of hydrogen protons are minute compared to that of the external magnetic field. To obtain magnetic contributions of hydrogen atoms, a magnetic flux induced detector is applied so that a magnetization change can be detected. A pulse with radio frequency is applied to stimulate proton magnets. As the radio frequency is turned on, proton magnets absorb the energy from the radio frequency pulse which is resonance with the corresponding magnetic field (42.58 MHz/Tesla) and some of proton magnets are excited to the high energy state which makes the proton magnets being anti-parallel to the direction of the magnetic field (see Figure 2.2.1 b). When sufficient energy is absorbed by the investigated region, the proton magnets will be in the same phase synchronizing with the radio frequency. At this moment, there will be no longitudinal magnetization and only transverse magnetization occurs. The transverse magnetization is perpendicular to the longitudinal magnetization and it can be detected. After removal of the radio frequency, proton magnets start to relax back to their original equilibrium state. During their relaxation, the transverse magnetization decreases, and the changes in the magnetization induce a current in the detection loop as well as produce free induction decay signals. As a result, a total signal of magnetization differences from all proton magnets is produced. This signal can be resolved to give magnetic contributions at each position by Fourier transform by a computer, which is due to different Larmor frequencies. The frequency of the resolved signal depends on the external field whereas the amplitude of the resolved signal before it starts to decay depends on the nature of the tissue. Tissues with different hydrogen contents give different amplitudes of the resolved signal. This provides a map of different nuclear magnetic resonance signals.

Nuclear magnetic resonance signals are not sufficient to give magnetic resonance images. After the radio frequency is removed, proton magnets start to dephase because of their magnetic repulsions. The dephase process is only associated with the proton spin themselves. It is called spin-spin relaxation or also  $T_2$  relaxation. In this process, the transverse magnetization is vanishing but there is no energy transfer. Meanwhile,

the excited proton magnets at the high energy state goes back to the low energy state by transfer their energy to the surrounding lattice. This process is called spin-lattice relaxation, which is also called  $T_1$  relaxation. Energy transfer takes place and all proton magnets go back to their original state so that the longitudinal magnetization recovers.

Magnetic resonance images can be obtained from taking advantages of  $T_1$  and  $T_2$  relaxations which depend on the tissue nature. To accentuate the  $T_1$  and  $T_2$  differences between various tissues,  $T_R$  and  $T_E$  sequences are applied.  $T_R$  is the repetition time. It stands for how quickly the radio frequency is turned on which is also the time interval between two radio frequency pulses.  $T_E$  is the echo time. It means how quickly we choose to measure to the signal coming back from transverse magnetization.

In a comparison between hydrogen atoms associated with fatty acids and water, hydrogen atoms bound in fatty acids are fixed tighter compared to those associated with water. Thus, the magnetic repulsions force them to have faster  $T_2$  relaxation which also speeds up their  $T_1$  relaxation. On the other hand, the free water molecules tend to hold the absorbed energy longer. As a result,  $T_2$  relaxation is slower which also delays  $T_1$  relaxation. The repetition time is fixed and the echo time is varied during  $T_1$  measurements so that the long  $T_1$  relaxation tissue is not fully recovered when the second pulse is applied. The second pulse excites more proton magnets to the high energy state and the transverse magnetization is smaller compared to those fully recovered ones. In addition, a negative longitudinal magnetization takes place. In contrast, the echo time is fixed and the repetition time is varied for  $T_2$  measurements, so that the second pulse does not interfere with  $T_2$  relaxation. The faster  $T_2$  relaxed tissues have smaller transverse magnetization since it decays faster than the slower  $T_2$  relaxed tissues. The fast  $T_2$  decayed tissues are assigned to be dark whereas the slow  $T_2$  decayed tissues are assigned to have a light color in the image. Sequences of  $T_1$  or  $T_2$  measurements are transformed by computer systems into magnetic resonance images.

### **Contrast agents for magnetic resonance imaging**

There are two classes of magnetic resonance contrast agents. There are  $T_1$ -weighted contrast agent and  $T_2$ -weighted ones.  $T_1$ -weighted contrast agents are paramagnetic

materials whereas  $T_2$ -weighted contrast agents are superparamagnetic materials. In principle, both  $T_1$ -weighted and  $T_2$ -weighted contrast agents enhance both  $T_1$  relaxation and  $T_2$  relaxation simultaneously because  $T_1$  relaxation and  $T_2$  relaxation are two processes which are influenced by each other.<sup>27</sup> The difference is that the superparamagnetic materials have a much higher magnetization compared to the paramagnetic materials and they have a stronger influence on the water molecules in the tissues under investigation, so that they can already speed up the proton relaxation from the initial relaxation step which is dominated by the  $T_2$  relaxation process. The paramagnetic materials do not have such strong magnetization compared to the superparamagnetic materials, so that they have a smaller influence on the fast relaxation process, the  $T_2$  relaxation, but due to their not negligible magnetization they can also enhance the  $T_1$  relaxation process.

The magnetic field of an electron is about 600 times stronger than that of a proton. A gadolinium atom has 7 unpaired electrons. Therefore, it is the most suitable paramagnetic atom for being a  $T_1$  contrast agent. The frequently used commercial  $T_1$ -weighted contrast agent is a complex of gadolinium. To enhance the  $T_1$  relaxation, the commercial gadolinium complex behaves as a catalyst.<sup>28</sup> Water molecules approach the contrast agent. Then the oxygen atoms in the water molecules get into contact with the gadolinium atom and the proton spins relax. The water molecules leave the contrast agent and another water molecules approach the contrast agent. As a result, one gadolinium atom can relax many water molecules. On the other hand, the superparamagnetic  $T_2$ -weighted contrast agents can enhance  $T_2$  relaxation without contacting water molecules. The best-known  $T_2$ -weighted contrast agents are based on magnetite ( $Fe_3O_4$ ) or maghemite ( $\gamma-Fe_2O_3$ ) in the form of water insoluble iron oxide crystals with typical diameters of 5-10 nm.<sup>27,29</sup>

## 2.2.2 Fluorescence Spectroscopy and Upconversion Measurements

Conventional fluorescence emitters follow the principle of Stokes law which states that the exciting photons have a higher energy than the corresponding emitting photons. These emitters are common since their output energy is smaller than their input energy.

The energy transfer processes are often described by a Jablonski diagram (Figure 2.2.2). Initially, a fluorophore absorbs an incident photon and an electron is excited from the ground state ( $S_0$ ) into an excited state ( $S_1/S_2$ ). This absorption step takes typically place within femtoseconds.<sup>30</sup> Then, the electron is likely to undergo vibrational relaxation or internal conversion, both are fast processes. Vibrational relaxation and internal conversion are non-radiative processes, which occur typically within picoseconds.<sup>30</sup> In a vibrational relaxation process, an electron relaxes from an upper vibrational level to a lower vibrational level at the same electronic state which may result in kinetic energy. This kinetic energy can stay within the excited molecule, or migrate to other surrounding molecules, which is significantly depending on the sample under investigation. Internal conversion occurs by interactions of different electronic states, leading to relaxation. Another possible route of relaxation is the emission of fluorescent photons. Fluorescence processes may occur in the nanosecond regime.<sup>30,31</sup> It is unlikely that these processes happen at the energy level above the first excitation state, above which non-radioactive processes often dominate. In the first excitation state, fluorescence processes are able to compete with non-radiative processes, so that the observed fluorescence often corresponds to a transition from the first excited state to the electronic ground state.

The Jablonski diagram shown in Figure 2.2.2 also describes the less probable non-radiative process within the excited molecules, which is called intersystem crossing.<sup>33</sup> In an intersystem crossing process, an electron changes its spin multiplicity from an excited singlet state to an excited triplet state. Usually, this is a forbidden transition, which is not allowed according to dipole selection rules. However, in some fluorophores, triplet state vibrational energy levels overlap with the lowest energy level at the first excitation singlet state. Under this circumstance, intersystem crossing processes are able to compete with fluorescence processes. An intersystem crossing

process takes usually  $10^{-8}$ - $10^{-7}$  s.<sup>31,33</sup> After the electron reaches an excited state triplet, there are two frequently observed paths to release the absorbed energy, i.e. by phosphorescence or delayed fluorescence.<sup>33</sup>

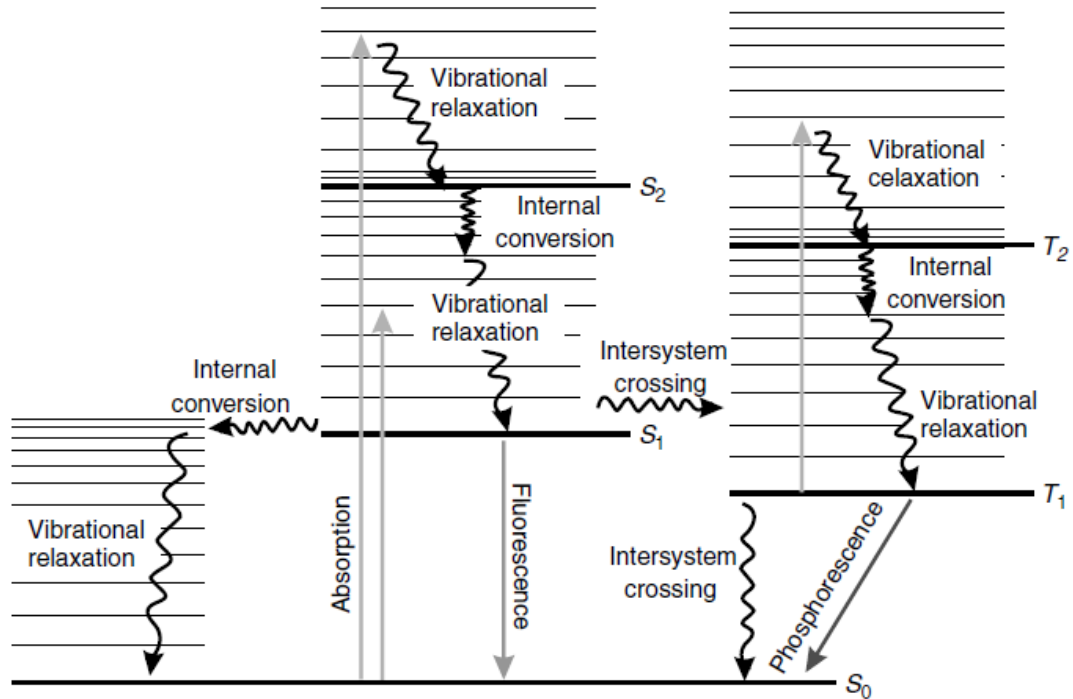


Figure 2.2.2: Jablonski diagram.<sup>30,32</sup>

Phosphorescence occurs if the excited electron directly relaxes from a triplet state to the electronic ground state. It is a radiative process but it is a much slower process than a fluorescence process with typical lifetimes of  $10^{-2}$ - $10^2$  s.<sup>31</sup> On the other hand, delayed fluorescence is also a radiative process, but it happens when the excited triplet electron or an electron at an undefined metastable state returns to the singlet excited state and releases the energy from the singlet excited state to the electronic ground state.<sup>34,35</sup> There are two characteristics to distinguish between fluorescence and delayed fluorescence. Firstly, the energy of the excited electron in delayed fluorescence is transferred to a triplet excited state or an undefined metastable state which usually has a lower energy than the firstly excited singlet state and then the energy may be transferred back to the singlet excited state. The energy migration between the singlet excited state and the triplet excited state or an undefined metastable state is in a kinetic equilibrium

which is affected by several parameters, such as temperatures and external magnetic fields. Unlike delayed fluorescence, fluorescence processes are usually independent of these parameters. Secondly, the major differences between fluorescence and delayed fluorescence are their lifetimes. Unlike fluorescence processes with typical lifetimes <1.5 ns, the lifetimes of delayed fluorescence processes are much longer and quite diverse.<sup>34</sup>

There are two types of known delayed fluorescence processes that are related to triplet excited states. E-type delayed fluorescence is thermally activated, and requires only one excited triplet electron. The lifetime of this type of delayed fluorescence will be equal to that of the concomitant phosphorescence. Such an energy transfer usually happens at room temperature in an inert medium. P-typed delayed fluorescence is not thermally activated, and it requires two excited triplet electron. The two excited triplet electrons undergo fusion and give one excited singlet electron as well as one ground state electron. Such delayed fluorescence is observed in solutions under intense excitation conditions. This process has a lifetime which is half of the lifetime to the corresponding concomitant phosphorescence process.<sup>34,36</sup>

However, the Jablonski diagram only describes one single excitation system. There are also fluorescence emitters which have anti-Stokes emissions. Such light emissions are also called upconversion process.<sup>37</sup>

Upconversion processes require two or more photons absorption, but unlike to multi-photon absorption processes, the photons in upconversion process can be absorbed sequentially instead of simultaneously. An efficient upconversion process also requires that the absorbing center having a metastable state which is in between the ground state and the emitting state. These metastable states play an important role as energy reservoirs.<sup>38</sup>

A number of different energy transfer processes have been recognized to take place in upconversion processes either as an independent phenomenon or as a part in a combination behavior. The most well-known mechanisms in upconversion processes include two-photon absorption (TPA), second-harmonic generation (SHG), multistep

excitation, which is caused by excited state absorption (ESA), sequential energy transfer which is also called APTE (Addition de Photon par Transfers d'Énergie), cooperative sensitization, cooperative luminescence, and avalanche effect. The abovementioned seven mechanisms are described in detail in the following paragraphs.<sup>5,37-41</sup>

It should also be noted in advance that all efficiencies described below are not usual efficiencies which are defined in percent since upconversion processes are non-linear - they absorb more photons than they emit. Upconversion fluorescence is only produced when a single ion absorbs more than two photons. Here, the relative efficiency  $\eta$  is normalized to the incident flux and is therefore given in  $\text{cm}^2/\text{W}$ . The higher efficiency indicates the probability of resonances between the incoming photons and the sample.<sup>37</sup>

- Two-Photon Absorption

Two photons with identical or different energy are absorbed within one ion simultaneously. The two-photon absorption upconversion in a two-level ion is illustrated in Figure 2.2.3. The energy gap between the two states, usually the ground state and an excited state of the ion is identical to the summation of the energy of the two absorbed photons. Typically, this type of excitation mechanism has the least efficiency among all seven mechanisms mentioned above.<sup>37</sup>

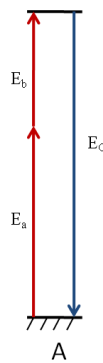


Figure 2.2.3: Two-photon absorption upconversion in a two-level ion. Two photons with energy  $E_a$  and  $E_b$ ,  $E_a$  and  $E_b$  can be either identical or different, are absorbed by an electron in the ion A simultaneously. The excited electron is then relaxed to its ground

state and emits light with  $E_c$ , where  $E_c$  is equal to  $E_a + E_b$ . The relative efficiency  $\eta$  of this process is of the order of  $10^{-13} \text{ cm}^2/\text{W}$ .<sup>37,38</sup>

- Second-Harmonic Generation

Two photons of the same energy interacting in a nonlinear crystal, such as potassium dihydrogen phosphate (KDP), are effectively converted together, to form new photons of twice the energy. In the second-harmonic generation process, there is no certain excitation states, simply two photons interact simultaneously with the crystal and one photon is released (Figure 2.2.4). Generally, second-harmonic generation of KDP is not an efficient upconversion process.<sup>42</sup>

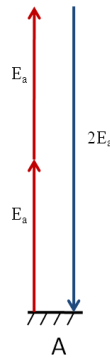


Figure 2.2.4: Second harmonic generation upconversion in an ion. The relative efficiency  $\eta$  of this process is of the order of  $10^{-11} \text{ cm}^2/\text{W}$ .<sup>37,40</sup>

- Excited State Absorption

Excited state absorption is also called two-steps absorption. A scheme illustrating this upconversion process, in which fluorescence is produced by excited state absorption, is shown in Figure 2.2.5. In such type of an upconversion process, the first incident photon excites an electron from the ground state to an intermediate state. The lifetime of this excited state is sufficiently long to absorb another photon and the electron is excited to the second excited energy level and then relaxes releasing upconversion fluorescence.<sup>39</sup> In short, two incident photons are absorbed by an ion

sequentially, and the absorbed energy is released by an emitting photon yielding upconversion fluorescence. Possible ions for excited state absorption usually have a ladder-like structure for their multi-energy level systems. Some lanthanide elements, such as  $\text{Er}^{3+}$ ,  $\text{Ho}^{3+}$ ,  $\text{Tm}^{3+}$ ,  $\text{Nd}^{3+}$ , have this characteristic energy level structure.<sup>5</sup> Also, they can be excited efficiently by commercially available diode lasers, which emit at 975 nm or 808 nm.<sup>5</sup> The relative efficiency  $\eta$  of this process is of the order of  $10^{-5} \text{ cm}^2/\text{W}$ .<sup>37</sup>

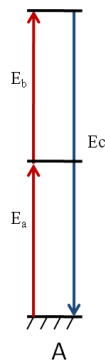


Figure 2.2.5: Excited state absorption on a single ion. Two photons are sequentially absorbed via a real intermediate energy level.<sup>38-40,43</sup>

- Energy transfer upconversion (Addition de Photon par Transfers d'Énergie)

Energy transfer upconversion is the most frequently observed upconversion mechanism in lanthanides crystals. Another well-known upconversion mechanism in lanthanides crystals is excited state upconversion (see above).<sup>43</sup> A scheme describing energy transfer upconversion fluorescence is shown in Figure 2.2.6. In energy transfer upconversion, at least two different kinds of ions, sensitizer (A) and activator (B), are involved. Initially, the sensitizer ion absorbs the incident photon individually and each of them transfers their energy to the activation ion.<sup>44</sup> Just like in excited state absorption upconversion, energy transfer upconversion also includes an excited state absorption step. The difference between excited state absorption upconversion and an energy transfer upconversion is that the activator ion absorbs the energy from the neighboring ion instead of incident light. The energy transfer upconversion process is important in upconversion nanoparticles for nanomedicine.<sup>5</sup> The most frequently

utilize sensitizer/activator pairs are  $\text{Yb}^{3+}/\text{Er}^{3+}$ ,  $\text{Yb}^{3+}/\text{Tm}^{3+}$ , and  $\text{Yb}^{3+}/\text{Ho}^{3+}$ . The advantage for  $\text{Yb}^{3+}$  being a sensitizer is that less non-radiative processes take place in  $\text{Yb}^{3+}$  ions because they have only two energy levels. In addition, the excitation wavelength for  $\text{Yb}^{3+}$  ions, which is around 975 nm, is within the optical transparency window for biological tissues.<sup>5</sup> The upconversion efficiency of an energy transfer upconversion process is related to the average distance between the sensitizer ion and the activator ion.<sup>5</sup> The relative efficiency  $\eta$  of this process is of the order of  $10^{-3} \text{ cm}^2/\text{W}$ .<sup>37</sup>

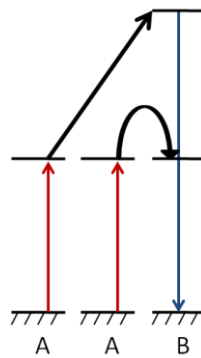


Figure 2.2.6: The energy transfer upconversion process between sensitizer ions (A) and an activator ion (B).<sup>39</sup>

- Cooperative Sensitization

There are at least three ions involved in cooperative sensitization upconversion. The scheme describing its mechanism is shown in Figure 2.2.7. Initially, the excited photons are absorbed by the sensitizer ions (A). Usually, these two ions have the same energy difference between their ground state and excited state, but this is not a fixed rule. After the two sensitizer ions being excited, both of them transfer their energy to the activator ion (B) simultaneously. Unlike energy transfer upconversion in which the sensitizer ions can transfer their energy to the activator sequentially, in this process the energy is transferred from the two sensitizer ions to the activator ion simultaneously in a cooperative sensitization process because there is no intermediate energy level in the activator ion. This process evidently involves the interactions between three ions. Thus, this is less likely to occur compared to the excited state absorption upconversion and the

energy transfer upconversion. The reported ion-pairs to date for cooperative sensitization are  $\text{Yb}^{3+}/\text{Tb}^{3+}$ ,<sup>45</sup>  $\text{Yb}^{3+}/\text{Eu}^{3+}$ ,<sup>46</sup> and  $\text{Yb}^{3+}/\text{Pr}^{3+}$ .<sup>47</sup> The relative efficiency  $\eta$  of this process is of the order of  $10^{-6} \text{ cm}^2/\text{W}$ .<sup>37</sup>

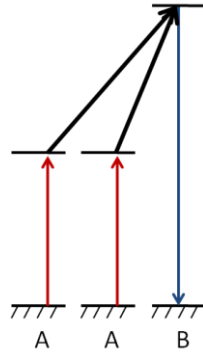


Figure 2.2.7: Cooperative sensitization upconversion: two sensitizer ions (A) transfer their energy to the activator ion simultaneously.<sup>5,37,39,40</sup>

- Cooperative Luminescence

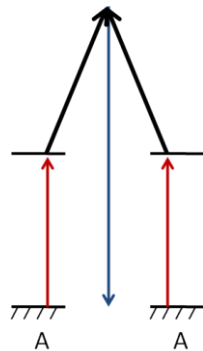


Figure 2.2.8: Cooperative luminescence. Two excited ions at short distance ( $5 \text{ \AA}$ ) release an upconversion photon.<sup>37</sup>

Cooperative luminescence upconversion involves interactions between two ions. Figure 2.2.8 shows the energy transfer route in cooperative luminescence upconversion. The process requires the close proximity of the interacting lanthanide ions. It can be a signature of clusters consisting of ions with distances of less than about  $5 \text{ \AA}$ .<sup>37</sup> Here, two

ions absorb two incident photons and both of them are excited to their excited state. Afterwards, the two ions interact with each other and produce a photon without transferring their energy to a certain energy state.<sup>40</sup> The most studied ion pair for cooperative luminescence is  $\text{Yb}^{3+}/\text{Yb}^{3+}$ .<sup>37</sup> The relative efficiency  $\eta$  of this process is of the order of  $10^{-8} \text{ cm}^2/\text{W}$ .<sup>37</sup>

- Photon Avalanche

Photon avalanche is an efficient upconversion process, but it requires a special condition. A schematic representation of the energy transfer route in a photon avalanche process is shown in Figure 2.2.9.

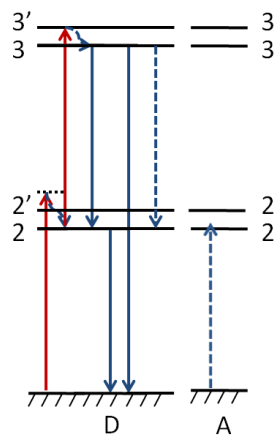


Figure 2.2.9: Photon avalanche upconversion between a donor ion (D) and an acceptor ion (A).

Initially, before the incident photon hits the target, an electron in the donor ion is thermally excited or non-resonantly excited from its ground state (level 1) to a higher meta-stable excited state (level 2') and then undergoes a fast relaxation to its excited state (level 2). After turning on the incident light, the energy difference between level 3' and level 2 is resonant with the incident light, and the electron at the level 2 is excited to level 3. Before reaching a certain threshold, the excited donor ion at level 3 relaxes to level 1 which makes it similar to an excited state absorption upconversion process. However, after reaching the threshold, another energy transfer route, cross relaxation, occurs. A

cross relaxation process transfers part of the donor energy to the acceptor ion and produces two ions at the level 2. In short, one excited electron at level 2 plus an incident photo gives two excited electrons at level 2. This is the so-called photon avalanche, where more and more electrons accumulate at level 2 which also increases the probability of upconversion fluorescence from level 3 to level 1. The threshold value of photon avalanche depends on the electron population at level 3, the rate coefficient at level 3, and the cross relaxation rate coefficient between donor ions and acceptor ions.<sup>37-39</sup>

### 2.2.3 Magnetic Property Measurement System

Field-dependent magnetization curves and temperature-dependent magnetization curves are obtained from using a magnetic property measurement system.

Superconductivity is of importance to a magnetic property measurement system. A superconducting material has no electrical resistance at the temperature under its characteristic superconducting critical temperature when an electrical current is passing through. There is no energy loss at such conditions, so that the electrical current is able to sustain for unlimited time without any application of voltages and there will be no measurable reduction of the current.<sup>48</sup> The reason for the absence of any electrical resistance in a superconducting material are paired electrons in the metal which are called Cooper pairs. Electrons repel other electrons because of their negative charge, and they are also attracted by positive ions which form a rigid metal lattice. When an electron is moving in the lattice, it attracts the neighboring positive charge which leads to a distortion in the ionic lattice. The attracted ion is moved slightly toward the electron and causes a zone with increasing positive charge density of the lattice. This part attracts an electron with an opposite spin compared to the moving one. The two involved electrons form a Cooper pair with a high binding energy. The paired electrons are dropping into a lower energy state, and increase the energy barrier for being scattered by the vibrating crystal lattice. As the temperature is lowered, the energy of the vibrating crystal lattice is also decreased, so that these Cooper pairs are more difficult to be scattered. Therefore, there is no energy loss in the crystal lattice, which also means that the electrical resistance of the superconducting material is zero in this superconducting state. In addition, superconducting materials expulse the magnetic field in this state, which is called the Meissner effect. Due to the Meissner effect the surrounding magnetic field is excluded from the inside superconducting material due to the establishment of an electrical current which is located near the surface (London penetration depth). The magnetic field created by the electrical current cancels the surrounding magnetic field.<sup>49</sup> Note that, the magnetic field is not fully canceled by the Meissner effect at a surface which is not deeper than London penetration depth.

The superconducting parts in a magnetic property measurement system provide stable magnetic field as well as the ability to measure small magnetic changes which are 14 orders of the magnitude smaller than the magnetic field.<sup>50</sup> There are four superconducting components in a magnetic property measurement system. These are a superconducting magnet which is an electromagnet consisting of coils made by superconducting wires, a superconducting detection coil which couples inductively to the sample, a superconducting quantum interference device which is connected to the detection coil, and a superconducting magnetic shield surrounding the superconducting quantum interference device by taking advantage of the Meissner effect in superconductors.<sup>50</sup>

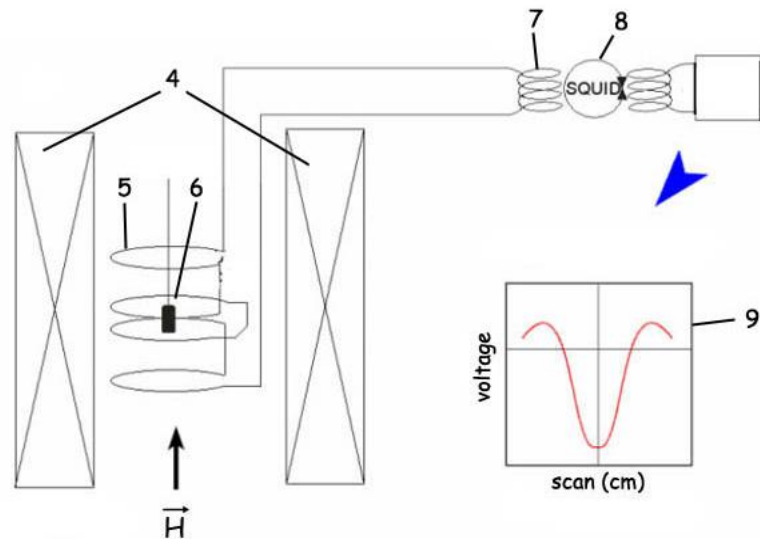


Figure 2.2.10: The different functional parts in a magnetic property measurement system.<sup>51</sup>

Magnetic moments of samples are obtained from a magnetic property measurement system according to the procedure described below (see Figure 2.2.10). The sample (6) is shifted through the detection coil (5) which is in the center of the superconducting coils of the magnet (4) and located outside of the sample chamber. As the sample is moving, the magnetic moment of the sample couples with the superconducting detection coil and an inductive electrical current is produced. The detection coil is connected with the input coil (7) of the superconducting quantum interference device (8)

and forms a closed superconducting loop, so that any changes in the magnetic moment of the sample will lead to a change in the produced electrical current which flows into the input coil of superconducting quantum interference device (SQUID).

The superconducting quantum interference device (SQUID, Figure 2.2.10, 8) in the magnetic property measurement system linearly converts the input current into an output voltage. It plays a crucial role in the magnetic property measurement system although it does not measure the magnetic moment of the sample directly. It contains superconducting loops and at least one Josephson junction. A Josephson junction consists of three layers of different materials as a sandwich. They are two superconducting thin layers which are separated from each other by a layer of non-superconducting material or insulator. When the input current is smaller than the critical current of the Josephson junction, there is no voltage across the Josephson junction. As the current reaches the critical value of the Josephson junction and is strong enough to overcome the energy gap of the two superconducting layers, a voltage, which depends linearly on the input current, is converted across the Josephson junction. Therefore, a Josephson junction is a current-voltage converter.

After the inductive current of the sample is converted into an output voltage by the superconducting quantum interference device, the output voltage signal (Figure 2.2.10, 9) can be transformed to yield the corresponding magnetic moment of the sample.

## **Magnetism**

When the magnetic field or the temperature is systematically varied, the field-dependent magnetization curve and the temperature-dependent magnetization curve of the sample can be obtained, providing its magnetic properties. Usually, magnetic behavior obtained from a magnetic property measurement system can be sorted as following: paramagnetic, diamagnetic, ferromagnetic, anti-ferromagnetic, and ferrimagnetic. Each type of magnetisms is briefly introduced in the following.

## Paramagnetism

The simplest type of magnetisms is paramagnetism. In a magnetic property measurement system, the paramagnet is attracted by the external magnetic field, so that the flux density (B) within the sample is larger than the applied magnetic field (H). The most obvious features in paramagnetism are shown in the field-dependent magnetization curves. They are linear, reversible, and there is no magnetization when the applied magnetic field is zero. The magnetic susceptibility is an important parameter to describe paramagnetism. Equation 2.2.1 shows the definition of magnetic susceptibility.

$$\chi = \frac{M}{H} \quad (\text{Equation 2.2.1})$$

where  $\chi$  is the magnetic susceptibility, M is the magnetic moment, and H is the applied magnetic field. There are many kinds of paramagnetism, such as Curie-type paramagnetism, Curie-Weiss paramagnetism, Pauli paramagnetism, and Van Vleck paramagnetism.<sup>50</sup> Among them, Currie paramagnetism is the most basic one. It results from the presence of atoms with unpaired electrons. The featured Curie behavior is shown in Equation 2.2.2.

$$\chi_c(T) = \frac{C}{T} \quad (\text{Equation 2.2.2})$$

where C is the Curie constant and T is the absolute temperature (K).

The effective magnetic moment,  $\rho_{\text{eff}}$ , of the Curie paramagnets are calculated from the experimentally determined magnetic susceptibility. It is a dimensionless quantity and is often expressed in units of Bohr magneto.<sup>52</sup> The further application is discussed in Chapter 4.1.3.

## Diamagnetism

Unlike paramagnetism, diamagnetism arises from paired electrons and the magnetization of a diamagnet is extremely small. Diamagnetic materials are repelled by

a magnetic field, so that the flux density ( $B$ ) is smaller than the applied field in a magnetic property measurement system. They have negative magnetic susceptibilities. Note that, superconducting materials are special cases of diamagnetic materials. They have the largest possible magnetic moments in diamagnetism.<sup>50</sup>

## **Ferromagnetism**

The so-called magnets which are able to be attracted by iron or permanent magnets are ferromagnets. Ferromagnetism is the strongest type of magnetism. Unlike paramagnets, ferromagnets have nonlinear and irreversible field-dependent magnetization curves. The irreversibility in the field-dependent magnetization curves is called magnetic hysteresis (Figure 2.2.11). Figure 2.2.11 shows that the measurement starts from the zero point and as the magnetic field ( $H$ ) is increased, the magnetization ( $M$ ) gradually reaches a maximum magnetization value, which is called saturation magnetization ( $M_S$ ). Saturation magnetization is an intrinsic property which is independent of the preparation and treatment history of the material. As the magnetic field is reduced back to zero, ferromagnets do not follow the former route of the magnetization curve. The curve does not reach the zero point when the applied magnetic field goes back to zero. The magnetization at zero fields is called remanent magnetization ( $M_{rem}$ ). The remanent magnetization depends on the preparation and treatment history of the material. Materials with large remanent magnetizations are called hard ferromagnets and they are useful in magnetic recording, whereas materials with small remanent magnetizations are called soft ferromagnets and they can be used in magnetic transformer cores. The magnetic field which can reduce the magnetic moment back to zero is called coercive field ( $H_C$ ). A coercive field depends on the rate of magnetic field changes. The major difference between ferromagnets and paramagnets is that all the magnetic moments in a ferromagnet have the same orientation. Thus, if one knows the orientation of one of the moment in a ferromagnet, one can predict the orientations of the rest of the moments. Instead of having all moments in the same orientation, each single moment in a paramagnet is nearly independent of the other moments in the same paramagnet, in spite of a high potential for a moment to align to the applied magnetic field. In addition, ferromagnets act like paramagnets above their Curie temperature. Below the Curie temperature, the magnetic susceptibility depends not only on the applied field but also

on the history of the magnet. Therefore, one uses saturated magnetization to describe the magnetic behavior of ferromagnets.<sup>50</sup>

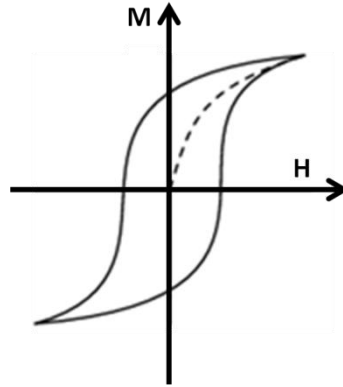


Figure 2.2.11: Magnetic hysteresis on magnetic field-dependent magnetization curves.<sup>53</sup>

### **Ferrimagnetism**

Ferrimagnets are also related to ferromagnets. Ferrimagnetism is similar to ferromagnetism, since the field- and temperature-dependent magnetic behavior of ferrimagnets is nearly same as that of ferromagnets. However, on the atomic level, the magnetic moments of ferrimagnets are not all pointing into the same direction. Adjacent magnetic moments having different magnitudes are locked in opposite directions.

### **Antiferromagnetism**

In antiferromagnetic magnets, the adjacent magnetic moments are also in different orientations, but all moments have the same magnitudes. The field-dependent behavior of antiferromagnets is similar to that of paramagnets, but the magnetic moments inside are locked together.

### **Superparamagnetism**

Superparamagnetism appears in small ferromagnetic or ferrimagnetic nanoparticles with a single domain. A short description of superparamagnetism is given in Chapter 2.1.2. The magnetic behavior of a superparamagnet is similar to that of a paramagnet, in the

sense that both materials show no remanent magnetization. However, the magnetic susceptibility of a superparamagnet is much larger than that of a paramagnet.

Due to the different magnetic behavior discussed above, it is essential to describe the magnetic behavior by a temperature-dependent magnetization curve. Furthermore, temperature-dependent magnetization curves can be transferred into temperature-dependent susceptibility curves simply by dividing the magnetization by the magnitude of the applied magnetic field. The obtained curves can be correlated to the Curie behavior or Curie-Weiss behavior in order to derive the Curie constant. The Curie constant is used for calculating the effective magnetic moment of the corresponding samples. A detailed discussion is given in Chapter 4.1.3.

## 2.2.4 X-ray Absorption Spectroscopy and X-ray Magnetic Circular Dichroism Spectroscopy (XAS and XMCD)

This chapter is divided into two parts: X-ray absorption and X-ray magnetic circular dichroism. The wavelengths of X-rays are in the range of  $10^{-2}$  nm to 10 nm which corresponds to the photon energy in the range of 0.1 keV to 100 keV. X-rays with energy between 0.1 keV and 2 keV are called soft X-rays whereas those with energy between 2 and 7.5 keV are called tender X-rays.<sup>54</sup> X-rays with energy above 7.5 keV are called hard X-rays.

### X-ray absorption

Due to the fact that X-rays are ionizing radiation, it is straightforward that X-rays have sufficient energy to eject a core electron from matter. X-ray absorption is the process in which the energy from incident X-rays is absorbed and a core electron is either excited to an unoccupied orbital or into the continuum.<sup>55</sup>

There are four important features of the X-ray absorption technique. Firstly, it is element specific. Secondly, it measures the partial density of the empty state which yields information on the electronic structure of the absorbing atom. Thirdly, it is sensitive to the local bonding of the atom which absorbs the incident photon energy (site selectivity). Lastly, one can derive information on the geometrical order of the material under study by X-ray absorption studies.<sup>56</sup> In fact, the radiation source for X-ray absorption is usually a storage ring at a synchrotron radiation facility. This is because synchrotron radiation sources produce highly brilliant X-rays. In addition, synchrotron radiation sources also provide a broad energy range that can range over the entire electromagnetic spectrum.

There are three possible recording paths of the X-ray absorption measurement: transmission, electron yield, and X-ray fluorescence detection. The transmission method is similar to the UV-Vis or IR techniques, so that quantitative information is obtained from the use of Beer-Lambert law.<sup>57</sup> There, the absorption coefficient is determined, which is sensitive to the bulk of the sample. The thickness of the sample should be

sufficiently thin, so that the incident photon can penetrate the sample and the transmitted photon can be measured by a detector to yield sufficient X-ray absorption signal. Alternatively, one can take the electron yield, which is frequently done for practical reasons, since no attenuation of the photon beam by the absorber needs to be measured. The incident photons impinge on the sample, core electrons with binding energies corresponding to the energy of the incident photon are excited to unoccupied orbitals or continuum states. At the same time, a core hole is created. An electron from the outer electronic shell is relaxed to refill the core hole. This is accompanied by the emission of Auger electrons. Auger electrons are surface sensitive since the escape path of the ejected electrons has only a length of a few nanometers. Photoelectrons may be emitted from the bulk involving inelastic scattering, which is corresponding to the probing depth of the sample, especially if the photon energy is varied.<sup>58</sup> Also, the thickness of the sample is less critical because the incident photon does not necessarily penetrate the sample. The third detection method relies on X-ray fluorescence which takes advantages of the decays of core holes. It is especially suitable for diluted alloys and thin films.<sup>59,60</sup>

In atoms the electrons bound in different orbitals have their own characteristic binding energies. When tunable X-ray scans through the binding energies of core electrons, there will be several abrupt increases in the absorption cross section (Figure 2.2.12). Those increases are called absorption edges. Each absorption edge corresponds roughly to the core-electron binding energy of a specific orbital of the absorbing element. These edges are named from K to Q according to the principal quantum numbers, 1-7, of the excited core electrons, but only K to M edges are frequently studied.<sup>55</sup>

L edge includes three edges (Figure 2.2.12 inset) which are L<sub>1</sub>-edge, L<sub>2</sub>-edge and L<sub>3</sub>-edge. L<sub>1</sub>-edge corresponds to an excitation of a 2s core electron and the excitations of 2p core electrons splits into 2 edges, i.e. L<sub>2</sub>- and L<sub>3</sub>-edges, due to spin-orbit-splitting. Spin-orbit-splitting occurs due to interactions between electron spins and the angular momentum generated by the orbital around the nucleus. Similarly, the M-edge includes 5-edges due to spin-orbit-splitting of the 3p and 3d core electrons.

The absorption features at edges in inner-shell excitation follow dipole selection rules, i.e.,  $\Delta l = \pm 1$ . The electric quadrupole allowed transitions which are corresponding to  $\Delta l = 0, \pm 2$  are possible as well, but the intensity of these transitions are weak compared to the allowed dipole transitions.

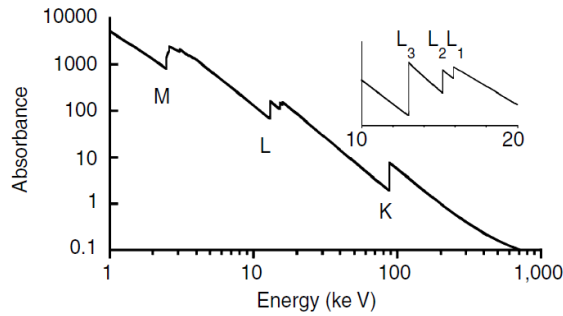


Figure 2.2.12: A schematic example of an X-ray absorption spectrum in which core electrons at different orbitals are excited. The inset shows the enlarged spectrum at the L absorption edge which includes the  $L_1$ ,  $L_2$ , and  $L_3$  edges corresponding to the excitations of  $2s$  and  $2p$  electrons.<sup>55</sup>

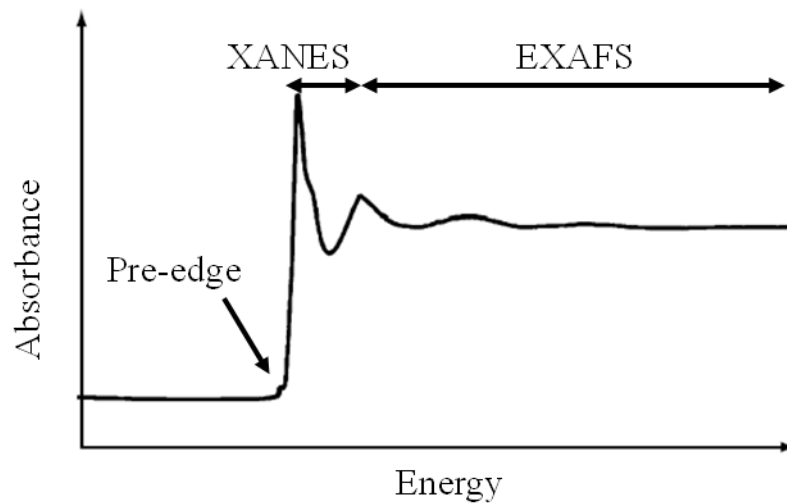


Figure 2.2.13: A schematic example of a typical absorption edge in an X-ray absorption spectrum. The absorption edge includes three regimes: pre-edge, X-ray absorption near edge structure (XANES) and extended X-ray absorption fine structure (EXAFS). This Figure is modified from the work of Penner-Hahn.<sup>55</sup>

Figure 2.2.13 shows a schematic absorption edge in an X-ray absorption spectrum. The absorption edge usually includes three regions: the pre-edge regime, the X-ray absorption near edge structure (XANES), and the extended X-ray absorption fine structure (EXAFS).<sup>55</sup>

The pre-edge regime is located below the onset of the absorption edge and it can be either flat or structured. Small structured features in the pre-edge regime are caused by electronic transitions to empty bound states. The energy position, the splitting and the intensity distribution of the structure in the pre-edge regime were found to be sensitive to the spin state, the oxidation state, and the geometry of absorbing atom.<sup>61</sup>

The X-ray absorption near edge structure is also called near edge X-ray absorption fine structure (NEXAFS) or X-ray absorption spectrum (XAS). The X-ray absorption spectrum is ranged from the onset of the absorption edge to about 50 eV into the continuum. X-ray absorption edges map out the electron densities of the empty states. For example, they measure the electron densities of the conduction band for a semiconductor, they measure the electron densities above the Fermi level for a metal, or they measure the electron densities of the lowest unoccupied molecular orbitals for molecules.<sup>62</sup> The region of the X-ray absorption near edge structure is caused by the process that core electrons are photo-excited into empty valence states. Therefore, the shapes and intensities of the X-ray near edge structure are influenced by the oxidation state of the element under study. One important application of X-ray absorption near edge structure is the investigation of oxidation states of elements.<sup>57</sup> It is known that the energy of an absorption edge increases if the oxidation state of the absorbing site is increased. This can be explained by an electrostatic model. The atoms with higher oxidation states are highly charged, and they are more stable, so that they require X-rays of higher energy to eject a core electron.

As the energy of incident X-rays increase, the excited core electrons have sufficient energy to leave the atoms under study. The outgoing electrons have the kinetic energy depending on the excess energy. They interact with the nearest neighboring atoms, and then, they are scattered by the electrons of those neighboring atoms. The interactions

between the backscattered electron and outgoing electron from the atom under study gives rise either to constructive or destructive interferences, so that the X-ray absorption cross section produces small oscillations above the absorption edge. These oscillations occur up to about 1000 eV above the absorption edge. The oscillations in this region are independent of the electronic structure and rely mostly on the number and distance of the nearest neighbor shell. Thus, the EXAFS-analysis provides the number, type of neighboring atoms, as well as their distance to the absorber.<sup>57</sup>

### **X-ray magnetic circular dichroism**

When symmetry of the absorbing atom is broken or the bonding of the absorbing atom is at the interfaces, a variety of anisotropy phenomena are taken place. The charge density, the spin density, and the orbital moment become anisotropic. These anisotropy effects can be detected by X-ray magnetic circular dichroism. The outstanding capabilities that belong to X-ray magnetic circular dichroism are its element specificity and that the spin and orbital magnetic moments of the absorbing site can be determined.<sup>63</sup>

X-ray magnetic circular dichroism is the measurement that is derived from X-ray absorption. X-ray magnetic circular dichroism spectra are obtained from calculating the difference between two X-ray absorption spectra taken at different helicity of the incident radiation. Specifically, one X-ray absorption spectrum is excited by right-handed circular polarized X-rays, whereas the other one is excited by left-handed circular polarized X-rays.<sup>64</sup>

The handedness of circular polarized X-ray is not uniquely defined. Usually, it is differentiated by the direction of the photon spin and the direction of the magnetic field. When the direction of the incident photon spin is parallel to the direction of the magnetic field, the incident radiation is called left-handed circular polarized radiation, whereas when the direction of the incident photon spin is anti-parallel to the direction of the magnetic field, it is called right-handed circular polarized radiation. This definition is summarized according to the literature published by Stöhr in 1995.<sup>65</sup> Therefore, the

measurements can be taken by either fixing the magnetization direction, changing the helicity of the X-ray, or by fixing the X-ray helicity and switching the magnetic field.

The process in X-ray magnetic circular dichroism is usually described by a two-step model which was proposed by Stöhr and Wu.<sup>63</sup> At the first step, the incident circular polarized photons transfer their energy to both, the orbital and the spin of the excited photoelectron if the photoelectron originates from a spin-orbit split level. In fact, a large amount of the photon angular momentum is transferred to the electron spin and this yields spin polarized electrons.<sup>63</sup>

When spin-orbit interactions are taken place, the orbital and the spin moments can either be parallel or anti-parallel to each other, so that the spin-orbit interaction usually splits the electrons into two different states. The spin and the orbital moments of the excited core electrons are parallel to each other at the energy level which is further from the nucleus whereas the spin and the orbital moments of the excited core electrons are anti-parallel to each other at the energy level which is closer to the nucleus. In other words, it requires more energy to excite a core electron when the spin and the orbital moments are anti-parallel to each other. Therefore, there are more electrons being excited with the spin and the orbital moments parallel to each other compared to the other case, where both quantities are anti-parallel to each other. Also, although the amount of spin-up and spin-down electrons should be same at each energy level because the net spin magnetic moment in a completely filled orbital should be zero, an additional effect of the spin-orbit interaction makes the spin-up (spin-down) electrons easier to be excited than the spin-down (spin-up) electrons at an energy level where the spin and the orbit are parallel (anti-parallel) to each other. Moreover, the differently polarized radiation has a different potential to excite electrons with different spins. The above mentioned three reasons are the first step of the X-ray magnetic circular dichroism.<sup>63</sup>

The magnetic properties are associated with the second step of the X-ray magnetic circular dichroism. The unoccupied valence orbitals act as detectors for the spin and orbital momentum of the excited core electrons. If the metal is ferromagnetic, there will be an imbalance between the unoccupied spin-up state and the unoccupied spin-down state. Therefore, the probabilities of the electrons being excited to the unoccupied

orbital by the differently polarized soft X-rays will be different, and hence, the unoccupied orbital can be regarded as a spin detector. Similarly, if there is an imbalance of states with different magnetic quantum number, the unoccupied orbital can be regarded as an orbital momentum detector. For example, the magnetic dichroism effects only occur in the summed  $M_4$  and  $M_5$  spectra when there are orbital moments in the unoccupied orbital. In short, X-ray magnetic circular dichroism spectra can be obtained from calculating the difference between the two polarized X-ray absorption spectra. The application of sum rules in the X-ray magnetic circular dichroism spectra can yield spin magnetic moments and orbital magnetic moments of the excited atoms separately. See Chapter 4.1.2 for further details.

# Chapter 3

## Experimental Details

### 3.1 Characterization Methods

This work was carried out by using the following equipment, consumables, and experimental conditions.

#### 3.1.1 Transmission Electron Microscopy

Sizes and shape of nanoparticles were analyzed by a transmission electron microscope (TEM) operating at 80 kV in the research division of oral structural biology, Charité-Universitätsmedizin Berlin. The TEM is an EM 902 from Zeiss. Specimens for TEM measurements were prepared by dropping a dilute dispersion of nanoparticles, either in chloroform or in water, on a copper grid. The copper grids are 400 mesh, coated by carbon films (Quantifoil). After evaporation of the solvent, the samples were ready to be studied in the TEM.

#### 3.1.2 Relaxometry Measurements

Relaxation times,  $T_1$  and  $T_2$ , are obtained from a nuclear magnetic resonance device (NMR) in the Leibniz-Institut für Molekulare Pharmakologie (FMP), Campus Berlin-Buch. The NMR studies made use of an AVANCE 400 spectrometer (Bruker) with a widebore UltraShieldPlus magnet. The operating field was 9.4 Tesla. Nanoparticles were dispersed in water in conventional NMR tubes and subsequently homogenized by five minutes ultrasonication. Five different concentrations of a sample along with another two blank solutions were fixed together with a rubber band and measured simultaneously in the NMR spectrometer.

### 3.1.3 Fluorescence Spectroscopy and Upconversion Measurements

Upconversion measurements were carried out in the research division of Prof. Dr. Kumke (Physical Chemistry, Potsdam University). The arrangement of the experimental setup is shown in Figure 3.1.1. A Nd:YAG laser/optical parametric oscillator system (Quantaray, Spectra-Physics, Mountain View, CA, USA) that the laser pumps at 355 nm and 1064 nm and the optical parametric oscillator produces the desired excitation radiation by a nonlinear crystal (NLK). This radiation is used to excite the sample and the luminescence emitted from the sample was focused by two lenses ( $f = 10$  cm) and detected by an iCCD camera (intensified charge coupled device, Andor Technology). The signal was transferred from the iCCD camera to a computer to be further processed. The samples were measured as dry powders on a sample holder with a quartz window.

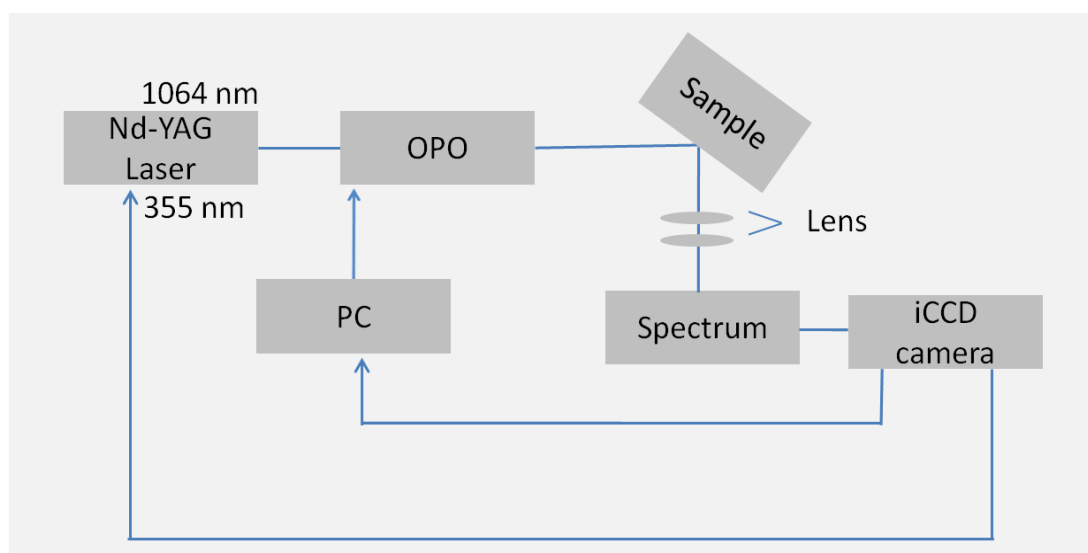


Figure 3.1.1: The arrangement of the experimental setup for upconversion measurements in the research division of Prof. Dr. Kumke (Physical Chemistry, Potsdam University).

### 3.1.4 Magnetic Property Measurement System

The field-dependent and temperature-dependent magnetizations are recorded using a Magnetic Property Measurement System (MPMS) manufactured by Quantum Design. This setup is located at Lise Meitner Campus, Helmholtz Zentrum Berlin. The magnetic

field is tunable from 0 to 5 T, and the temperature range is 2-400 K. The dried solid powder is fixed in a capsule and the capsule is fit into a simple commercial plastic straw (see Fig 3.1.2), as shown in Fig 3.1.2.

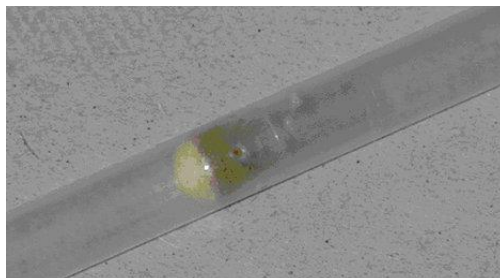


Figure 3.1.2: The hand-made sample holder for SQUID measurements.

### **3.1.5 X-ray Absorption Spectroscopy and X-ray Magnetic Circular Dichroism Spectroscopy**

Gadolinium and europium  $M_{4,5}$  XAS and XMCD measurements were carried out at the X11MA beam line at the Swiss Light Source at the Paul Scherrer Institute in Villigen/Switzerland using circularly polarized, tunable soft X-rays. The experimental end station consists of a  $^4\text{He}$  cryostat which is equipped by 7 T superconducting coil. All measurements were carried out in ultra-high vacuum of  $p < 10^{-7}$  Pa at 5 K. The samples were prepared by depositing and drying a droplet containing the corresponding nanoparticles on a Cu-substrate.

## 3.2 Preparation of Nanoparticles

### 3.2.1 General Procedures for Nanoparticles and Ligands Preparation

All chemicals were purchased and used without further purification, otherwise it will be mentioned. All glassware was cleaned by aqua regia, 8% solution of hydrogen fluoride and neutralized by 2% Mucosol solution. After rinsing the glassware with ultra-pure water several times and dried in an oven (333 K), the glassware is ready for nanoparticles preparations.

### 3.2.2 Chemicals

Table 3.2.2.1 lists all chemicals used in this work, including the product numbers of the production company.

Table 3.2.2.1: Chemical lists.

Chemical	Company Name (product number)	Purity	Remarks
Diethylene glycol	Sigma-Aldrich (32160)	99%	-
Dialyzer membrane	ZelluTrans/Roth (E660)	-	Cellulose, MWCO: 6000-8000.
1-Octadecene	Aldrich (O806)	90%	Colorless liquid
Ammonium fluoride	Fluka (09737)	≥ 98.0%	White solid, under argon
Chloroform	VWR (22706.361)	≥ 99.0%	-
Dichloromethane	Sigma-Aldrich (320269)	≥ 99.5%	-
Dimethylformamide	Carl Roth	≥ 99.5%	-
Diethylene glycol	Sigma-Aldrich (32160)	≥ 99.0%	-
Erbium(III) chloride hexahydrate	ABCR (AB113023)	99.9%	Pink solid
Ethanol	Berkel AHK (0511U)	100%	-
Europium(III) chloride hexahydrate	Aldrich (212881)	99.9%	White solid
Formaldehyde	Sigma-Aldrich(25.254-9)	37%	In water
Gadolinium(III)	Aldrich (G7532)	99%	White solid

chloride hexahydrate			
Hydrochloric acid	Carl Roth (4625.1)	37%	-
Hydrogen fluoride	Sigma-Aldrich (01066)	40-45%	Hazardous
Methylamine	Aldrich (534102)	33%	In absolute ethanol
Mucosol	Sigma-Aldrich (Z637181)	-	Detergent
Nitric acid	Carl Roth (4989.1)	≥ 65%	-
Oleic acid	ABCR (AB110607)	90%	White solid at 4°C
Phosphorous acid	Sigma-Aldrich (21.511-2)	99%	-
Polyethylene glycol	Aldrich (202487)	Mn 550	-
Sodium azide	Sigma-Aldrich (S2002)	≥ 99.5%	-
Sodium hydroxide	Carl Roth (6771.1)	≥ 65%	White pellets
Tetrahydrofuran	Sigma-Aldrich (186562)	≥ 99.0%	-
Thionyl chloride	Riedel-de Haën (18438)	≥ 98%	-
Toluene	Sigma-Aldrich (244511)	99.8%	Anhydrous
p-Toluenesulfonyl chloride	Sigma-Aldrich (T35955)	≥ 98%	-
Triphenylphosphine	Sigma-Aldrich (T84409)	99%	-
Ytterbium(III) chloride hexahydrate	ABCR (AB122265)	99.9%	White solid
Yttrium(III) chloride hexahydrate	ABCR (AB106773)	99.9%	White solid

### 3.2.3 Synthesis of Lanthanide Oxide Nanoparticles

Lanthanide oxide nanoparticles were synthesized by a colloidal method modified by Petoral in 2009.<sup>66</sup> 3 mmol of lanthanide chloride hexahydrate and 15 mL of diethylene glycol were mixed in a 50-mL, three-necked round bottom flask. The reaction mixture was stirred and evacuated at room temperature to reduce the oxygen concentration. Afterwards, the temperature was raised to 140°C under Ar atmosphere for 1 h. Next, 3.75 mmol of NaOH in 15 mL diethylene was added. After complete dissolution of the reactants, the temperature was raised to 180°C for another 4 h. The excess amount of diethylene glycol was removed by dialysis against ethanol.<sup>67</sup> The reaction mixture was introduced in a tubular membrane of cellulose (MWCO = 6-8 kDa), and immersed in a

beaker filled with ethanol. The solution in the beaker was replaced every 24 h for 3 days. The particles were stored in the mixture of ethanol and diethylene glycol.

### **3.2.4 Synthesis of Lanthanides Fluoride Nanoparticles**

Lanthanides fluoride nanoparticles were prepared according to a procedure reported by Wang et al.<sup>68</sup>  $\text{LnCl}_3 \cdot 6\text{H}_2\text{O}$  (Ln: lanthanide elements, 2 mmol), oleic acid (15 g, 53 mmol) and octadecene (35 mL) were added into a three necked round bottom flask equipped with a magnetic stir bar. The temperature sensor was adjusted to a suitable position, which allows a direct contact with the reaction mixture. The entire reaction system was closed and evacuated at 40 °C by an oil pump to remove the air until the air bubbles disappeared. Then, the temperature was raised to 80 °C to remove the water. Afterwards, an argon flow was applied and the temperature was raised to 160 °C until all salts were dissolved. The reaction system was then cooled down to room temperature. After cooling down, a fine powder mixture of sodium hydroxide (0.2 g) and ammonium fluoride (0.3 g) was added. The temperature was then raised to 160 °C and the reaction mixture was stirred at this temperature until the solution became clear. Subsequently, the temperature was increased to 300 °C for 1.5 h. Then, the system was cooled down to room temperature and stirred overnight. The particles were obtained from removal of the excess organic reactants. This was accomplished by centrifugation at 1500 rpm for 20 min in a solvent mixture of ethanol and THF for three times. The particles were stored in THF.

### **3.2.5 Synthesis of PEO-monophosphonate Ligands**

#### **3.2.5.1 Synthesis of $\text{Me}(\text{OCH}_2\text{CH}_2)_{11}\text{SO}_3\text{C}_6\text{H}_4\text{Me}_p$ <sup>69</sup>**

A mixture of sodium hydroxide solution (2.05 g, 51.25 mmol, in 10.5 mL Millipore water) and polyethylene glycol 550 solution (10 g, 18.18 mmol, in 10.5 mL THF) were cooled in an ice-water bath and a solution of 4-toluenesulfonyl chloride (6.32 g, 33.15 mmol, in 10.5 mL THF) was added into the reaction mixture dropwisely over 2 h. The

reaction mixture was stirred for another 2 h at 5 °C. The resulting mixture was poured into iced water (100 mL) and extracted with dichloromethane (50 mL, twice). The organic phases were combined, washed with water (50 mL, twice) and saturated brine (50 mL), dried over magnesium sulfate, and finally dried by a rotary evaporator. The final product is in a colorless oily form with 97.4% yield. <sup>1</sup>H NMR (CDCl<sub>3</sub>) δ = 7.81 (2H, C<sub>6</sub>H<sub>4</sub>, d), 7.37 (2H, C<sub>6</sub>H<sub>4</sub>, d), 4.07 (2H, CH<sub>2</sub>, t), 3.7-3.6 (42H, CH<sub>2</sub>, m), 3.39 (3H, OCH<sub>3</sub>, s), and 2.47 (3H, CH<sub>3</sub>-Ar, s).

### 3.2.5.2 Synthesis of Me(OCH<sub>2</sub>CH<sub>2</sub>)<sub>11</sub>NHMe<sup>69</sup>

Me(OCH<sub>2</sub>CH<sub>2</sub>)<sub>11</sub>SO<sub>3</sub>C<sub>6</sub>H<sub>4</sub>Me-*p* (12.47 g, 17.71 mmol) was dissolved in 33% methylamine in ethanol (10.8 ml). The temperature was raised to 74 °C for 48 h. The reaction mixture was dried by rotary evaporator. The resulting residue was dissolved with 5% HCl (6 mL), and extract with chloroform (10 mL, three times). The chloroform extracts were washed separately with 5% HCl (8 mL, twice), and all the HCl extracts were combined, made basic with 30% sodium hydroxide solution (8 mL) and extracted with chloroform (15 mL, three times). The chloroform extracts were washed separately with water (5 mL) and the solvent was dried by rotary evaporator to give pale yellow oil. The yield was 92.5%. <sup>1</sup>H NMR (CDCl<sub>3</sub>) δ = 3.38-3.26 (44H, CH<sub>2</sub>, m), 3.10 (3H, CH<sub>3</sub>O, s), and 2.17 (3H, CH<sub>3</sub>N).

### 3.2.5.3 Synthesis of Me(OCH<sub>2</sub>CH<sub>2</sub>)<sub>11</sub>NMeCH<sub>2</sub>PO(OH)<sub>2</sub><sup>70</sup>

Me(OCH<sub>2</sub>CH<sub>2</sub>)<sub>11</sub>NHMe (4 g, 7.15 mmol), phosphorous acid (0.59 g, 7.15 mmol) and 6.5M HCl (1.1 mL) were heated to reflux. Afterwards, 40% formaldehyde solution (1.25 g) was added to the above mentioned reaction mixture over 0.5 h under magnetic stirring. The reaction mixture was refluxed overnight. The resulting product was dried by freeze-drying, and recrystallized in acetone. The yield was 31%. ESI negative [M-H]<sup>-</sup> = 622.32 g/mol.

## 3.2.6 Synthesis of PEO-diphosphonate Ligands

### 3.2.6.1 Synthesis of $\text{Me}(\text{OCH}_2\text{CH}_2)_{11}\text{NH}_2$ <sup>71</sup>

Polyethylene glycol 550 (10 g, 18.18 mmol) was degassed at 80°C for 1 h. An Ar flow was applied and the reaction system was cooled in an iced-water bath while thionyl chloride (2 mL, 27.54 mmol) was added dropwisely. The reaction temperature was then raised to 25°C and stirred for 4 h. The reaction mixture was diluted by dimethyl formamide, and the resulting mixture was dried by a rotary evaporator. This step was repeated three times to remove all residue of thionyl chloride to give intermediate 1.

Sodium azide (1.77 g, 27.23 mmol) and the obtained intermediate 1 were dissolved in DMF (100 mL), and the reaction mixture was stirred overnight at 85°C. The solvent was removed by a rotary evaporator and dichloromethane (200 mL) was added. The resulting solid was filtered and the solvent was removed by a rotary evaporator to give intermediate 2.

The intermediate 2 was dissolved in THF (150 mL), and triphenylphosphine (7.15 g, 27.26 mmol) was added to the mixture. The obtained solution was stirred at 25°C for 4 h before adding 1 mL of water and then the reaction system was stirred overnight. Afterwards, the solvent was removed by a rotary evaporator. 100 mL of water was added to the resulting residue and the solid was removed by filtration. The water phase was washed by toluene (25 mL, three times) and the water phase was removed to yield light yellow oily product. The overall yield after 3 stages was 95%. <sup>1</sup>H NMR ( $\text{CDCl}_3$ )  $\delta$  = 3.46-3.69 (44H,  $\text{CH}_2$ , m), 3.37 (3H,  $\text{CH}_3$ , s) and 2.85 (2H,  $\text{NH}_2$ , t).

### 3.2.6.2 Synthesis of $\text{Me}(\text{OCH}_2\text{CH}_2)_{11}\text{N}(\text{CH}_2\text{PO}(\text{OH})_2)_2$ <sup>70</sup>

$\text{Me}(\text{OCH}_2\text{CH}_2)_{11}\text{NH}_2$  (3.93 g, 7.15 mmol), phosphorous acid (1.18 g, 14.40 mmol) and 6.5M HCl (2.20 mL) were heated to reflux. Afterwards, a 40% formaldehyde solution (2.50 g) was added to this reaction mixture over 0.5 h under stirring. The reaction mixture was refluxed overnight. The resulting product was dried by freeze-drying and recrystallized in acetone. The yield was 82.5%.

### **3.2.7 Ligand Exchange<sup>72</sup>**

A nanoparticle solution (1 mL), as described in Chapter 3.2.4, was added into a solution of PEO-mono-phosphonate/PEO-di-phosphonate ligands (1 g, Chapter 3.2.5.3/Chapter 3.2.6.2) in 5 mL ethanol. The reaction mixture was heated to 70°C and stirred overnight. The resulting reaction mixture was cooled down to room temperature. Hexane (3 mL) was added, the mixture was centrifugated at 1500 rpm for 30 min, and the organic phase with oleate was discarded. This step was repeated 3 times. The ethanol was removed mildly with help of a rotary evaporator and water was added to redisperse the nanoparticles. The excess amount of phosphonate ligands was removed by dialysis against water.

# Chapter 4

## Results and Discussions

Chapter 4 is divided into three parts, magnetic studies on  $\text{Gd}_2\text{O}_3$  nanoparticles (Chapter 4.1), magnetic studies on lanthanide-doped  $\text{NaGdF}_4$  nanoparticles (Chapter 4.2) and optical studies on Eu-, Er-, and Yb-doped  $\text{NaGdF}_4$  nanoparticles (Chapter 4.3).

### 4.1 Magnetic Studies on $\text{Gd}_2\text{O}_3$ Nanoparticles

Gadolinium oxide ( $\text{Gd}_2\text{O}_3$ ) nanoparticles have been considered as a possible contrast agent for magnetic resonance imaging (MRI) due to the 7 unpaired electrons in  $\text{Gd}^{3+}$ .<sup>73</sup> Doping  $\text{Gd}_2\text{O}_3$  nanoparticles with fluorescent lanthanides makes such nanoparticles multifunctional. A thermal annealing process on these nanoparticles is able to alter their magnetic properties.<sup>74</sup> Chapter 4.1 is focused on the influence of Eu dopants and thermal annealing processes on  $\text{Gd}_2\text{O}_3$  nanoparticles in terms of magnetic behavior.

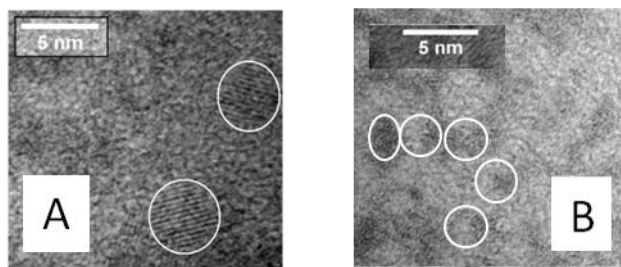


Figure 4.1.1: High resolution transmission electron microscopy images of the (A) Eu-doped  $\text{Gd}_2\text{O}_3$  and (B) undoped  $\text{Gd}_2\text{O}_3$  samples. The average sizes are (A)  $4.5 \pm 0.5$  nm and (B)  $2.5 \pm 0.5$  nm.

Three samples were prepared for the study, an undoped  $\text{Gd}_2\text{O}_3$  sample, an unannealed Eu-doped  $\text{Gd}_2\text{O}_3$  sample, and an annealed Eu-doped  $\text{Gd}_2\text{O}_3$  sample. The annealed Eu-doped  $\text{Gd}_2\text{O}_3$  sample was prepared by an additional annealing process on the unannealed Eu-doped  $\text{Gd}_2\text{O}_3$  sample in diethylene glycol at  $140^\circ\text{C}$  for 30 hours under

an inert atmosphere. Detailed synthetic methods are described in Chapter 3.2.3. High resolution electron microscopy images of these samples are shown in Figure 4.1.1.

The local magnetic properties of these samples are discussed in terms of X-ray absorption spectra (XAS) (Chapter 4.1.1) and X-ray magnetic circular dichroism spectra (XMCD) (Chapter 4.1.2). The bulk magnetic behavior of these samples are discussed in terms of the magnetization obtained from SQUID experiments (SQUID: superconducting quantum interference device) (Chapter 4.1.3). Finally, conclusions are drawn in Chapter 4.1.4.

### 4.1.1 X-ray Absorption Spectra Studies

X-ray absorption spectroscopy is an element and orbital specific technique to probe the local electronic structure of matter. An absorption edge occurs as a step-wise increase in an absorption cross section when a core electron absorbs energy which is equal to or larger than the binding energy of the core electron. In addition, resonant excitation into unoccupied orbitals provides discrete near-edge X-ray absorption fine structure (NEXAFS). The following absorption edges of Eu and Gd are used to be studied:  $L_{2,3}$  ( $2p \rightarrow 5d$ ) and  $M_{4,5}$  ( $3d \rightarrow 4f$ ). Due to the large absorption cross section of the  $M_{4,5}$  edges and the energy restriction (90-2000 eV) of the beamline at the Swiss Light Source X11MA, this study represents investigation of the local electronic properties at the  $M_{4,5}$  edges for both Eu and Gd. The  $M_4$  edges of both Eu and Gd occur because the core electron is excited from the  $3d_{3/2}$ -state mainly into the  $4f_{5/2}$ -state whereas the  $M_5$  edges is due to the excitation of a core electron from the  $3d_{5/2}$ -state mainly into the  $4f_{7/2}$ -state. According to the literature, the peak maxima of the  $M_4$  and  $M_5$  edges for Eu are located at 1161 eV and 1131 eV, respectively, whereas those for Gd occur at 1217 eV and 1185 eV, respectively.<sup>75</sup>

The XAS shown in Figure 4.1.2 are recorded in the range from 1120 eV to 1240 eV. These spectra are obtained from an average value of left- and right-handed circularly polarized synchrotron radiation. The absorption maxima at 1133, 1160, 1185 and 1215 confirm the presence of the elements Eu and Gd in the samples.

The areas under the corresponding elemental edges are integrated separately and the Gd-to-Eu XAS intensity ratios are calculated accordingly. The Gd-to-Eu XAS intensity ratio is  $2.65 \pm 0.01$  for the unannealed sample and  $2.66 \pm 0.01$  for the annealed one. To confirm the X-ray absorption results, additional atomic absorption spectra (AAS) were recorded. These show somewhat higher Gd-to-Eu ratios between these samples, which are  $4.3 \pm 0.1$  for the unannealed sample and  $4.0 \pm 0.1$  for the annealed sample. The different Gd-to-Eu ratios between the XAS results and AAS results are likely due to the different mass attenuation coefficients<sup>76</sup> and noise levels between Eu and Gd in XAS measurements, so that the AAS results appear to be correct. The mass attenuation coefficient is a measure of how strongly a chemical species absorbs or scatters light with given energy per unit mass. These results clearly indicate a similar elemental composition for the unannealed and annealed samples.

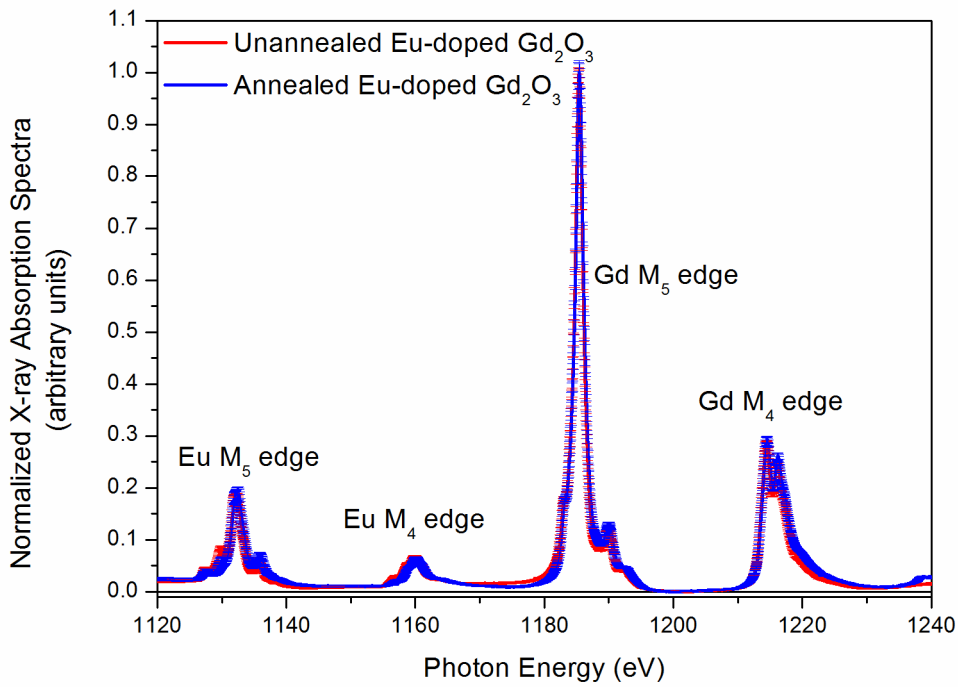


Figure 4.1.2: A comparison of XAS between the unannealed and annealed Eu-doped  $\text{Gd}_2\text{O}_3$  samples at the Eu  $M_{4,5}$  and Gd  $M_{4,5}$  absorption edges. The measurements were performed at  $T = 5$  K and  $B = 6$  T. The spectra are normalized to the corresponding absorption intensities at 1185 eV.

Figure 4.1.2 is divided into two parts, the Gd edges (Figure 4.1.3) and the Eu edges (Figure 4.1.4), for further discussions.

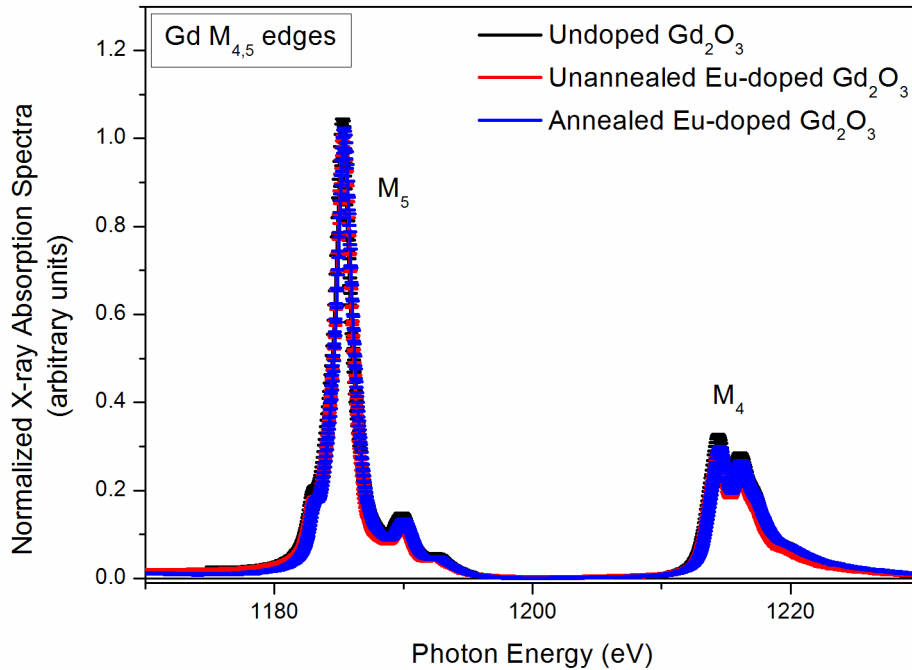


Figure 4.1.3: A comparison of XAS between the undoped Gd<sub>2</sub>O<sub>3</sub>, unannealed Eu-doped Gd<sub>2</sub>O<sub>3</sub>, and annealed Eu-doped Gd<sub>2</sub>O<sub>3</sub> samples at the Gd M<sub>4,5</sub> absorption edges. The measurements were taken at T = 5 K and B = 6 T. The spectra are normalized to the corresponding absorption intensities at 1185 eV.

In Figure 4.1.3 XAS of all samples under study, the unannealed and annealed Eu-doped Gd<sub>2</sub>O<sub>3</sub> samples as well as the undoped Gd<sub>2</sub>O<sub>3</sub> sample, are presented. All three spectra are shown with their standard deviation calculated from at least eight different scans. No specific difference is observed between these three samples.

The electronic configuration of Gd is [Xe]4f<sup>7</sup>5d<sup>1</sup>6s<sup>2</sup>. Therefore, Gd<sup>3+</sup>, [Xe]4f<sup>7</sup>, is the most stable oxidation state which can be found in most of the gadolinium compounds. Consistently, the only XAS signal that is found comes from Gd<sup>3+</sup>.<sup>77,78</sup> In comparison with the literature reported Gd<sup>3+</sup> XAS,<sup>77,78</sup> it is confirmed that both the band shapes and

the energy positions of the spectral features shown in Figure 4.1.3 are identical to previous work. Therefore, it is confirmed that the oxidation state of Gd that is present in these samples is +3.

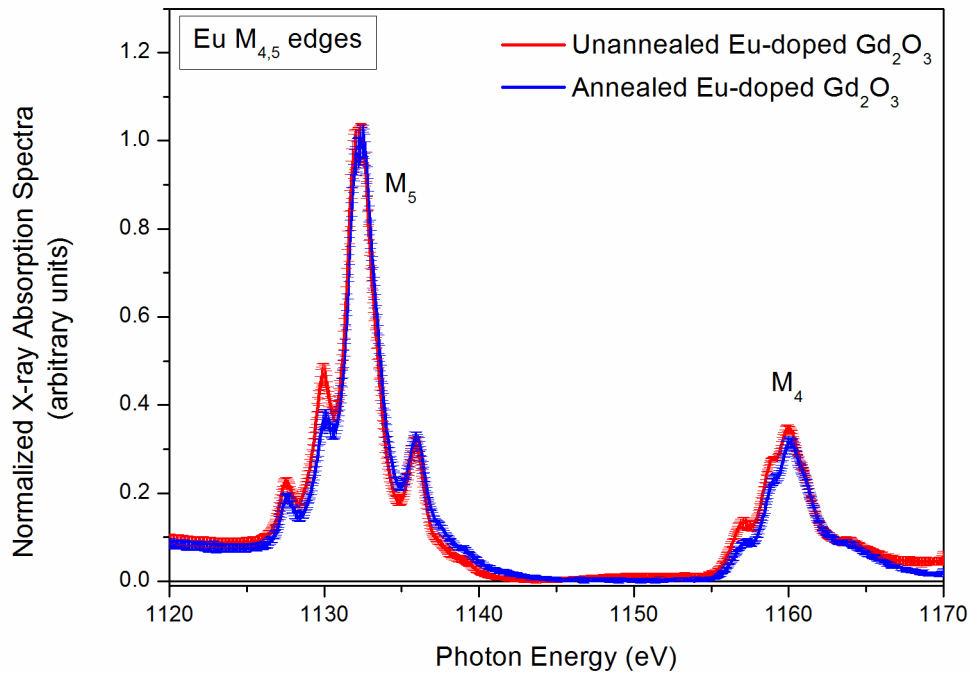


Figure 4.1.4: A comparison of XAS between the unannealed and annealed Eu-doped  $\text{Gd}_2\text{O}_3$  samples at the Eu  $M_{4,5}$  absorption edges. The measurements were taken at  $T = 5$  K and  $B = 6$  T. The spectra are normalized to the corresponding absorption intensities at 1132 eV.

In Figure 4.1.4, both the unannealed and annealed Eu-doped  $\text{Gd}_2\text{O}_3$  nanoparticles samples are present. The electronic configuration of Eu is  $[\text{Xe}]4f^76s^2$ , and there are two oxidation states of Eu which are often found in the europium compounds,  $\text{Eu}^{2+}$  which has the electronic configuration  $[\text{Xe}]4f^7$  and  $\text{Eu}^{3+}$  which corresponds to  $[\text{Xe}]4f^6$ . It is known from earlier work that  $\text{Eu}^{2+}$  and  $\text{Eu}^{3+}$  can be distinguished by XAS.<sup>78</sup> In comparison with the reported data, it is known that both samples contain not only  $\text{Eu}^{3+}$  but also  $\text{Eu}^{2+}$ . The obvious feature of  $\text{Eu}^{2+}$  at  $M_5$  edge is the peak which is located at 1130 eV, whereas the other features occurring in this spectral regime are mainly due to

Eu<sup>3+</sup>. According to Figure 4.1.4, the Eu<sup>2+</sup>-to-Eu<sup>3+</sup> ratio is larger in the unannealed sample than in the annealed one, since the Eu<sup>3+</sup> intensity is in both samples comparable and the unannealed sample has an absorption intensity that is  $1.5 \pm 0.1$  times larger than the annealed one at 1130 eV.

As a result, XAS clearly indicate the existence of Gd and Eu in both Eu-doped Gd<sub>2</sub>O<sub>3</sub> samples. The oxidation state of Gd is in both samples +3, whereas for Eu, +2 and +3 are found for both samples.

### **4.1.2 X-ray Magnetic Circular Dichroism Spectra Studies**

The local magnetic properties of the three samples under study are investigated by X-ray magnetic circular dichroism (XMCD). An XMCD spectrum is obtained from the difference between XAS that are taken using left- and right-handed circularly polarized synchrotron radiation. The obtained XMCD spectrum is able to give both the local orbital magnetic moment and the local spin magnetic moment of a given element by using sum rules.<sup>79</sup> The local orbital and spin magnetic moments obtained from sum rules give information of the magnetic contribution of a specific element in a multi-component or heterogeneous system.<sup>80</sup>

Figure 4.1.5 shows XMCD spectra of the unannealed and annealed samples which are normalized to the corresponding absorption intensity at 1186 eV. It is clearly seen that the signal is significantly larger at the Gd edges than at the Eu edges. This does not necessarily mean that the Gd atoms have larger XMCD signals than the Eu atoms because these XMCD spectra are not normalized to the corresponding X-ray absorption spectra which produce the XMCD signal for a given atom. The larger XMCD signal at the Gd edges is also possible to indicate that the Eu and Gd concentrations are different. The spectra show that, as the Gd XMCD signals are same, the XMCD signals of the unannealed sample at Eu edges are larger than those of the annealed sample.

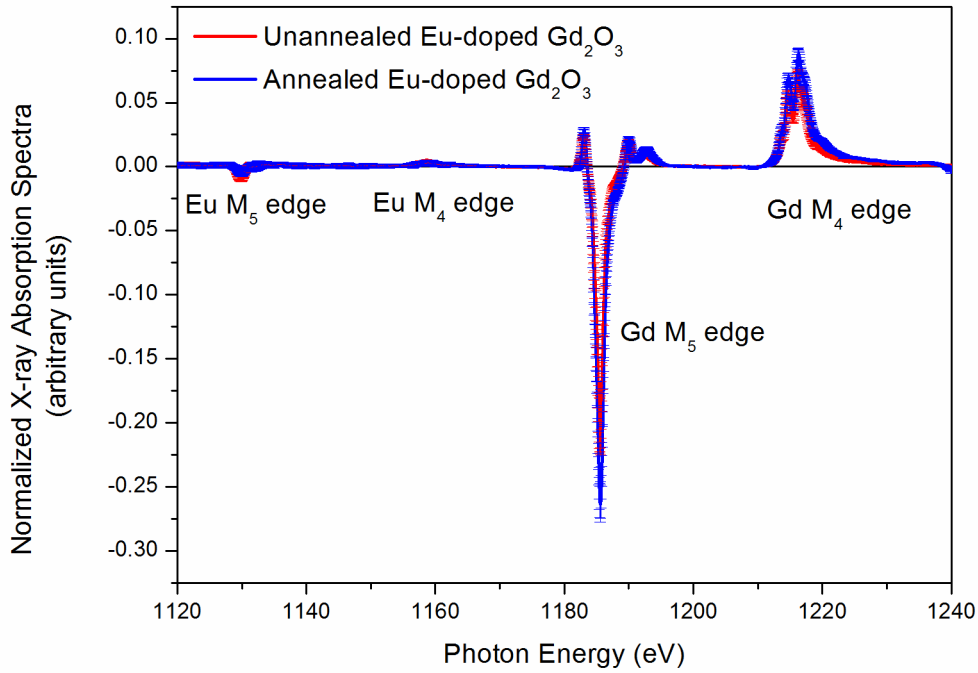


Figure 4.1.5: A comparison of XMCD spectra between the unannealed and annealed Eu-doped  $\text{Gd}_2\text{O}_3$  samples at the Gd  $M_{4,5}$  and Eu  $M_{4,5}$  absorption edges. The measurements were taken at  $T = 5$  K and  $B = 6$  T. The spectra are normalized to the corresponding absorption intensity at 1186 eV.

Figure 4.1.5 is divided into two parts, the Gd  $M_{4,5}$  edges shown in Figure 4.1.6 and the Eu  $M_{4,5}$  edges shown in Figure 4.1.7. All of the XMCD spectra are normalized to areas of the corresponding XAS absorption edges. Therefore, the XMCD behavior in both Figures 4.1.6 and 4.1.7 can be regarded as the average magnetic behavior for a single atom, which is either Gd or Eu, in the corresponding samples.

Figure 4.1.6 shows that the Eu-doped  $\text{Gd}_2\text{O}_3$  samples show stronger XMCD signals at the  $M_5$  edge than the undoped  $\text{Gd}_2\text{O}_3$  sample. Furthermore, the annealed sample has a stronger XMCD signal at the  $M_5$  edge than the unannealed one, but the difference between these samples is small. XMCD signal intensities of all three samples at the  $M_4$  edge are almost the same.

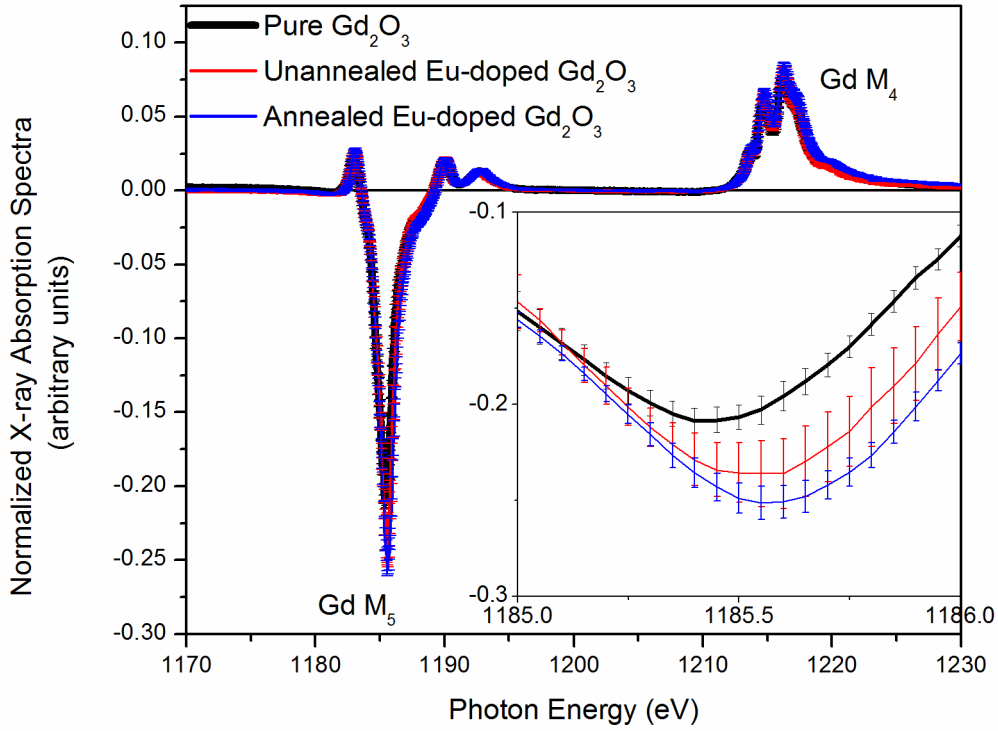


Figure: 4.1.6: A comparison of XMCD spectra between the undoped  $Gd_2O_3$ , unannealed Eu-doped  $Gd_2O_3$ , and annealed Eu-doped  $Gd_2O_3$  samples at the Gd  $M_{4,5}$  absorption edges. The spectra are normalized to the area of corresponding XAS. The enlarged peak at 1185 eV is shown in the inset.

The orbital magnetic moment ( $m_{Lz}$ ) and the spin magnetic moment ( $m_{Sz}$ ) of these samples are calculated using the following sum rules (Equation 4.1.1 and Equation 4.1.2) where the results are summarized in Table 4.1.1.<sup>79,81,82</sup>

(Equation 4.1.1):

$$m_{Lz} = -\langle L_z \rangle \mu_B = 2n_h \frac{\int_{M_5+M_4} (\mu^+ - \mu^-)}{\int_{M_5+M_4} (\mu^+ + \mu^-)} \mu_B$$

(Equation 4.1.2):

$$m_{S_z} = -2 \langle S_z \rangle = \left( 2n_h \frac{\int_{M_5} (\mu^+ - \mu^-) - \frac{3}{2} \int_{M_4} (\mu^+ - \mu^-)}{\int_{M_5+M_4} (\mu^+ + \mu^-)} + 6 \langle T_z \rangle \right) \mu_B$$

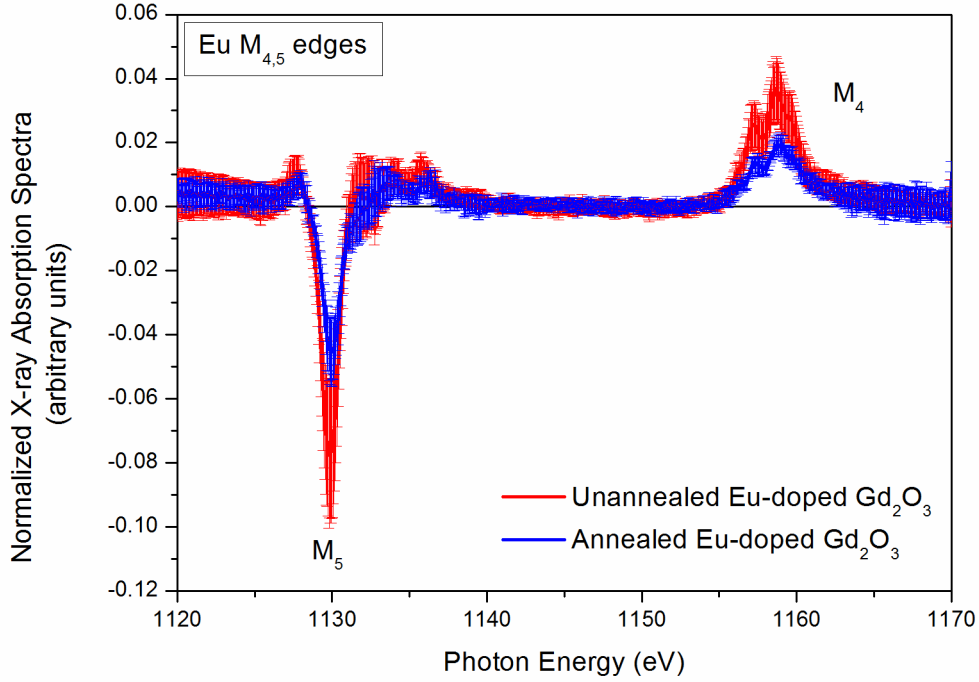


Figure 4.1.7: A comparison of XMCD spectra between the unannealed and annealed Eu-doped  $Gd_2O_3$  samples at the Eu  $M_{4,5}$  absorption edges. The spectra are normalized to the area of the corresponding XAS.

$\langle L_z \rangle$ ,  $\langle S_z \rangle$  and  $\langle T_z \rangle$  are orbital angular momentum, spin angular momentum, and magnetic dipole term, respectively;  $n_h$  is the number of electron holes in the  $4f$  shell; the  $\mu^+$  and  $\mu^-$  are the X-ray absorption coefficients with the helicity of the circular polarization parallel and anti-parallel to the direction of the fixed magnetization orientation.

The term  $\langle T_z \rangle$  provides a measure of the anisotropy of the spin magnetic moment. It can be altered by anisotropic charge distribution (quadrupole moment, crystal-field

effects) around the atom or spin-orbit interactions.<sup>83,84</sup> The quadrupole moment is zero in bulk systems with cubic symmetry, but it can be increased when the symmetry is broken. For  $3d$  electrons,  $\langle T_z \rangle$  is usually neglected.<sup>82,84,85</sup> However, for  $4f$  electrons, the spin-orbital interaction is usually not negligible.<sup>79</sup> Fortunately, spin-orbit interactions are the dominant contribution to  $\langle T_z \rangle$  in rare earths compared to crystal-field effects and  $\langle T_z \rangle$  is almost independent on the crystal field. Therefore,  $\langle T_z \rangle$  for  $4f$  electrons can be calculated for the free ions.<sup>82</sup> The rare earths system at  $M_{4,5}$  edges can be described by an almost pure LSJ coupling at Hund's rule ground state.<sup>86</sup>  $\langle T_z \rangle$  of such systems can be evaluated by Equation 4.1.3.<sup>84</sup>

(Equation 4.1.3):

$$\langle T_z \rangle = \langle M \rangle \left( l - n_h + \frac{1}{2} \right) \frac{3(S-J)^2(S+J+1)^2 - L(L+1)[L(L+1)+2S(S+1)+2J(J+1)]}{2(2l+3)(2l-1)(2L-1)SJ(J+1)}$$

where  $l$  and  $n_h$  are the azimuthal quantum number and the number of electron holes in the valence shell;  $S$  is the total spin momentum operator (Equation 4.1.4),  $L$  is the total orbital momentum operator (Equation 4.1.5), and  $J$  is total angular momentum operator (Equation 4.1.6).<sup>86</sup>

$$S = \sum_{i=1}^N s_i \quad (\text{Equation 4.1.4})$$

$$L = \sum_{i=1}^N l_i \quad (\text{Equation 4.1.5})$$

$$J = L + S \quad (\text{Equation 4.1.6})$$

The open shell of  $Gd^{3+}$  ions is the  $4f$  shell, so that  $l$  and  $n_h$  reaches values 3 and 7, respectively. There are 7 unpaired electrons in the  $4f$  shell implying that  $S$  is for  $Gd^{3+}$   $7/2$  ( $7 \times 1/2$ ),  $L$  is for  $Gd^{3+}$  0 ( $(-3) + (-2) + (-1) + 0 + 1 + 2 + 3$ ), and  $J$  is  $7/2$  ( $7/2 + 0$ ). When the above mentioned numbers are put into Equation 4.1.3, it is found that  $\langle T_z \rangle$  is zero for  $Gd^{3+}$ . This is reasonable to assume, which is due to the zero value of the total orbital angular momentum. Thus, there is no spin-orbit coupling in  $Gd^{3+}$ . Therefore, the magnetic dipole term in Equation 4.1.2 is eliminated. The calculated values of  $m_{Lz}$  and

$m_{S_z}$  are shown in Table 4.1.1. The results are based on XAS spectra shown in Figure 4.1.3 and XMCD spectra shown in Figure 4.1.6.

Table 4.1.1: The  $m_{L_z}$  and  $m_{S_z}$  values of  $Gd^{3+}$  in the undoped  $Gd_2O_3$ , Eu-doped  $Gd_2O_3$ , and annealed Eu-doped  $Gd_2O_3$  samples calculating according to sum rules.

	$m_{L_z} (\mu_B/Gd^{3+})$	$m_{S_z} (\mu_B/Gd^{3+})$	$m_{total} (\mu_B/Gd^{3+})$
Theoretical value	0	-7	-7
Undoped $Gd_2O_3$	$0.19 \pm 0.02$	$-4.59 \pm 0.03$	$-4.32 \pm 0.04$
Unannealed Eu-doped $Gd_2O_3$	$0.04 \pm 0.02$	$-4.59 \pm 0.02$	$-4.55 \pm 0.03$
Annealed Eu-doped $Gd_2O_3$	$0.19 \pm 0.01$	$-5.06 \pm 0.01$	$-4.87 \pm 0.01$

The XMCD results shown in this Chapter were taken at the magic angle, which means that the angle between the incident X-rays (the magnetization direction) and the sample surface normal is  $54.7^\circ$ . The reason to measure at the magic angle is to force the samples having rotational symmetry parallel to the surface normal.<sup>87</sup> In this way, the magnetic dipole term  $\langle T_z \rangle$  in Equation 4.1.2 can also be regarded as zero. All measurements have the same angle between the magnetization direction and the sample surface normal during measurements, so that a comparison between all three samples under study is possible. Due to the not observable  $Gd^{2+}$  absorption in the XAS spectra shown in Figure 4.1.3, the  $m_{L_z}$  and  $m_{S_z}$  values of the samples are calculated under the assumption that all XMCD-signals are due to  $Gd^{3+}$ . To calculate the theoretical values in Table 4.1.1, the orbital and spin angular moments of a free atom are used as the expected orbital- and spin-magnetic moments for the samples under study. The expected  $m_{S_z}$  value is equal to -2 times the theoretical spin momentum of a free  $Gd^{3+}$  (cf. Equation 4.1.2), which is  $-2 \times 7/2$ . The expected  $m_{L_z}$  value is equal to -1 times the theoretical orbital momentum of a free  $Gd^{3+}$  (cf. Equation 4.1.1), which is  $-1 \times 0$ , i.e. zero. Note that the reported magnetic moment of  $Gd^{3+}$  is larger than 7; usually it is found between 7-8  $\mu_B$ . This is because the  $4f$  electrons lead to an induced polarization of the  $6s$  and  $5d$  valence electrons, which introduce extra magnetic moments.<sup>88</sup>

It can be seen from Table 4.1.1 that the unannealed Eu-doped  $Gd_2O_3$  sample has  $m_{L_z}$  values close to zero. This means that the orbital magnetic moments of the  $4f$  orbital, which arise from the 7 unpaired electrons in the  $4f$  orbital, have cancelled in this sample. Such electronic configuration is expected due to the lowest energy which is possessed

by the Gd ions. However, in the other two samples, the undoped Gd<sub>2</sub>O<sub>3</sub> and the annealed Eu-doped Gd<sub>2</sub>O<sub>3</sub>, show  $m_{Lz}$  values that are slightly larger than zero, which is beyond the expectation. These  $m_{Lz}$  values are less than an integral and are still close to zero so that it is regarded as a statistic behavior, which means that most of the Gd atoms have a zero  $m_{Lz}$  value, and only part of the Gd atoms have a larger orbital moment. In comparison with the literature, it is found that all the Gd, Gd<sub>2</sub>, GdO and Gd<sub>2</sub>O clusters have Gd  $m_{Lz}$  values  $0.7 \pm 0.3 \mu_B$  whereas the Gd  $m_{Lz}$  value of Gd<sub>40</sub>Fe<sub>60</sub> is about zero.<sup>81,85</sup> Therefore, it is supposed that higher Gd orbital moments than zero in both of the undoped Gd<sub>2</sub>O<sub>3</sub> and the annealed Eu-doped Gd<sub>2</sub>O<sub>3</sub> samples may be related to Gd-Gd interactions in the samples. On the other hand, in the presence of other metals, such as Eu and Fe, such Gd-Gd interactions may become negligible. The Gd-Gd interaction is likely caused by high Gd concentrations and the presence of O. These conditions lead to antiferromagnetic Gd<sup>3+</sup>-O-Gd<sup>3+</sup> clusters.<sup>89</sup> Unfortunately, this result remains speculative and the clear mechanism leading to these results cannot be determined with the available experimental material so that it remains unknown. The reason for the non-zero orbital moment in the annealed Eu-doped Gd<sub>2</sub>O<sub>3</sub> sample implies that the Eu ions in the sample are clustered during the annealing process, which means that the Eu ions disperse in the Gd<sub>2</sub>O<sub>3</sub> host heterogeneously. Such behavior was also observed in Mn-doped CdSe quantum dots, in which the Mn ions are clustered in the CdSe host after the annealing process.<sup>90</sup>

When comparing the  $m_{Sz}$  values of the three samples under study, it can be seen that the spin magnetic moment of the undoped sample is close to that of the Eu-doped samples. In other words, the doping of Eu ions does not alter the spin magnetic moment of Gd<sup>3+</sup>. In addition, the local magnetic properties of Gd<sup>3+</sup> in Gd<sub>2</sub>O<sub>3</sub> nanoparticles should not be influenced by the crystal fields and the organic ligands on the particle surface. However, the annealing process increases the spin magnetic moment by about 10%.

The XMCD spectra of the unannealed and annealed Eu-doped Gd<sub>2</sub>O<sub>3</sub> samples at the M<sub>4,5</sub> edges of Eu are shown in Figure 4.1.7. The XAS spectra of the unannealed and annealed Eu-doped Gd<sub>2</sub>O<sub>3</sub> samples shown in Figure 4.1.4 indicate that Eu<sup>2+</sup> as well as Eu<sup>3+</sup> are present in the samples. However, Eu<sup>3+</sup> is assigned to be a non-magnetic element

because its total angular momentum ( $J$ ) which is related to magnetic moment of an atom is zero.<sup>91</sup> Magnetic moment of an atom is calculated by Equation 4.1.7.

$$m_{\text{atom}} = g_J \mu_B \sqrt{J(J+1)} \quad \text{Equation 4.1.7}$$

where  $g_J$  is Landé  $g$ -factor and  $\mu_B$  is Bohr magneton. Therefore, the XMCD signal in Figure 4.1.7 should be mainly contributed by  $\text{Eu}^{2+}$  ions.

At first glance in Figure 4.1.7, it is found that the unannealed sample, which has larger  $\text{Eu}^{2+}$ -to- $\text{Eu}^{3+}$  ratio, shows a stronger XMCD signal than the annealed sample. However, the XAS signals shown in Figure 4.1.4 are mainly due to  $\text{Eu}^{3+}$ . In addition to the fact that  $\text{Eu}^{3+}$  is non-magnetic oxidation state, when comparing with the reported experimental data of  $\text{Eu}^{2+}$  XMCD and  $\text{Eu}^{3+}$  XMCD,<sup>92-94</sup> it is found that the XMCD signals in Figure 4.1.7 are mainly due to  $\text{Eu}^{2+}$  because the peak at the  $M_5$  edge is located at 1130 eV, instead of 1132 eV, which would indicate the presence of  $\text{Eu}^{3+}$ .<sup>95</sup> The stronger magnetization in  $\text{Eu}^{2+}$  than in  $\text{Eu}^{3+}$  is due to the fact that the spin magnetic moment and orbital magnetic moment of  $\text{Eu}^{3+}$  have been cancelled by each other. Because of the different Eu compositions, when the XMCD spectra are normalized to the area of corresponding XAS, the difference between the unannealed sample and the annealed one may be caused by the annealing process or by a different  $\text{Eu}^{2+}$ -to- $\text{Eu}^{3+}$  ratio. Therefore, there is no sufficient evidence to prove the annealing effects on the Eu absorption edges.

Table 4.1.2:  $m_{Lz}$  and  $m_{Sz}$  values of Eu in undoped  $\text{Gd}_2\text{O}_3$ , unannealed Eu-doped  $\text{Gd}_2\text{O}_3$ , and annealed Eu-doped  $\text{Gd}_2\text{O}_3$  samples calculated according to sum rules, Equation 4.1.1 and Equation 4.1.2, based on the XAS spectra shown in Figure 4.1.4 and XMCD spectra shown in Figure: 4.1.7.

	$m_{Lz} (\mu_B/\text{Eu})$	$m_{Sz} (\mu_B/\text{Eu})$	$m_{\text{total}} (\mu_B/\text{Eu})$
Theoretical value	0	-7	-7
Unannealed Eu-doped $\text{Gd}_2\text{O}_3$	$0.40 \pm 0.03$	$-0.97 \pm 0.04$	$-0.57 \pm 0.05$
Annealed Eu-doped $\text{Gd}_2\text{O}_3$	$0.32 \pm 0.02$	$-0.79 \pm 0.03$	$-0.47 \pm 0.04$

The results shown in Table 4.1.2 are calculated by Equations 4.1.1 and 4.1.2 and are based on the parameter of  $\text{Eu}^{2+}$ . Unlike the magnetic moments shown in Table 4.1.1

which give the magnetic moments of a single  $Gd^{3+}$ , the magnetic moments shown in Table 4.1.2 gives the average magnet moments of  $Eu^{2+}$  and  $Eu^{3+}$ . All we can mention about Table 4.1.2 is that the  $m_{Lz}$  value can be either due to  $Eu^{3+}$  or clustered  $Eu^{2+}$ . The  $m_{Sz}$  and  $m_{total}$  values are quite small compared to the expected values. The reason for this finding should be attributed to the fact that the majority Eu ions,  $Eu^{3+}$ , are non-magnetic and only the minority Eu ions,  $Eu^{2+}$ , have contribution to the XMCD signal. Also, the strong influence of the Gd ions may be one of the reasons as well. Ott et al. have proved that the high proportion of Gd ions doped in EuO films reduced the XMCD signal of Eu.<sup>96</sup> Furthermore, the Eu magnetization is small compared to the Gd magnetization in these two samples.

In summary, XMCD studies reveal that the doping agent Eu has no influence on the Gd spin magnetic moment but the orbital magnetic moment is decreased after the addition of Eu, which is possibly due to the elimination of Gd-Gd interactions. Because of the anti-parallel relation between the orbital magnetic moment and the spin magnetic moment of Gd calculated by sum rules, the total magnetic moment of Gd is increased after the addition of Eu as a dopant. An annealing is able to increase both of the spin and orbital magnetic moments. However, due to the minor influence of the increased orbital magnet moment compared to the increased spin magnetic moment, the total magnetic moment is still increased after the annealing process. The orbital magnetic moment of Gd should be influenced by the location of Eu ions in  $Gd_2O_3$ . Due to the different  $Eu^{2+}$ -to- $Eu^{3+}$  ratios in unannealed and annealed  $Gd_2O_3$  nanoparticles samples, the annealing effect on the Eu magnetization is not fully clear. However, it is clear that the influence of Eu magnetization is minute compared to the Gd magnetization.

### 4.1.3 Superconducting Quantum Interference Device Studies

In contrast to XAS and XMCD studies which give local magnetic information of a single element, superconducting quantum interference device studies (SQUID) give complementary information on magnetic properties in multi-elemental samples. The aim for SQUID studies of the three samples under study is to compare the total magnetic moments either per sample weight unit or per magnetic ion with the total magnetic moments per  $\text{Gd}^{3+}$  or  $\text{Eu}^{3+}$  ion obtained from XMCD studies making use of sum rules. The detailed sample preparation procedures are shown in Chapter 3.1.4.

The field-dependent magnetization curves of dried nanoparticles coated with diethylene glycol shown in Figure 4.1.8 are normalized to the sample mass. These curves describe the magnetic behavior of the entire sample. They indicate a change of the magnetization as a function of the external magnetic field strength.

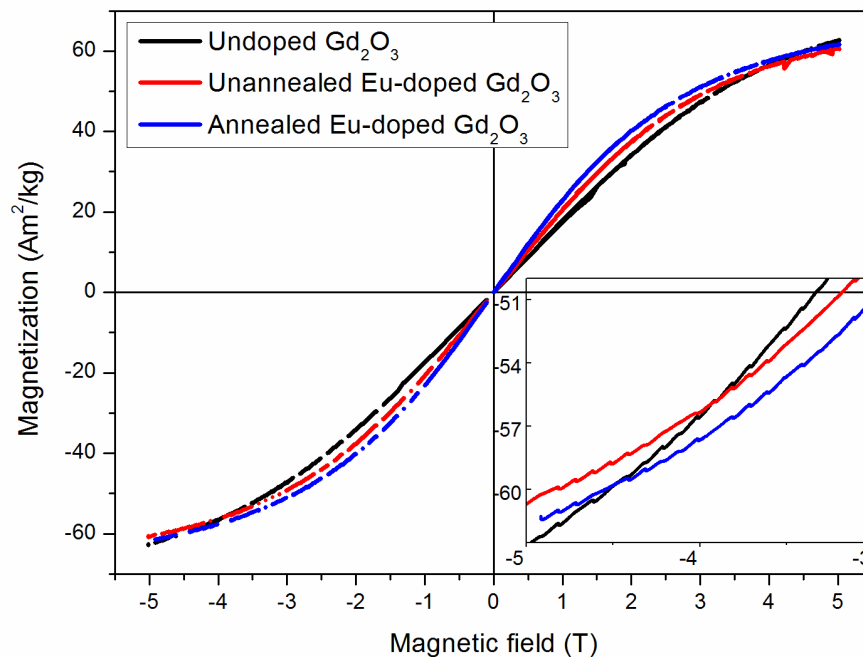


Figure 4.1.8: Magnetization curves as a function of external magnetic field measured at  $T = 5$  K. All of the curves are normalized to the corresponding sample mass. The inset shows the enlarged magnetization behavior of the three samples under study from  $-5$  T to  $-3$  T.

Huang et al. used gelatin cores as templates to produce hollow  $\text{Gd}_2\text{O}_3$  particles and porous  $\text{Gd}_2\text{O}_3$  particles. These authors proved that hollow  $\text{Gd}_2\text{O}_3$  particles are superparamagnetic at room temperature, whereas porous  $\text{Gd}_2\text{O}_3$  particles are paramagnetic.<sup>97</sup> They concluded that the superparamagnetism of the hollow  $\text{Gd}_2\text{O}_3$  particles is due to an extra calcination step during particles preparation. The calcination step caused a carbon layer on these particles because of the incomplete conversion of organic reactants, and this carbon layer leads to superparamagnetism of the hollow  $\text{Gd}_2\text{O}_3$  particles. Although the mechanism is not explained, they have proved that a removal of carbon layer switched the magnetic properties of the hollow  $\text{Gd}_2\text{O}_3$  particles. Those hollow  $\text{Gd}_2\text{O}_3$  particles became paramagnetic after the removal of the carbon layer. This conclusion shows that the magnetic properties are affected not only by the magnetic ions themselves but also the environment of the nanoparticles. As for the samples under study, Figure 4.1.8 points out that all three  $\text{Gd}_2\text{O}_3$  nanoparticles samples are not paramagnetic at 5 K because the magnetization curve is nonlinear. Furthermore, this data show that they are also not ferromagnetic since there is no remanence left after the magnetic field is removed (Measurement cycles from 0 T to 5 T, then back to 0 T and -5 T and again back to 0 T are carried out). The observed s-shaped magnetization curve is typical for superparamagnetic particles.<sup>98,99</sup> Such behavior is expected for particles size smaller than 5 nm. Figure 4.1.1 shows that samples under study are smaller than 5 nm. Petoral et al. also found magnetization curves with a similar shape for Tb-doped  $\text{Gd}_2\text{O}_3$  particles with 4.3 nm in diameter measured at 5 K. In addition, they have also shown that these curves become linear which means paramagnetic when the temperature is increased to above 50 K.<sup>66</sup>

The undoped  $\text{Gd}_2\text{O}_3$  samples are the least magnetized at magnetic field ranging between 0 T to 4 T. Afterwards, the magnetization of undoped  $\text{Gd}_2\text{O}_3$  increases rapidly and finally it has at 5 T a higher magnetization than the other two Eu-doped samples, (Figure 4.1.8 inset). This means that above 4 T, the magnetic susceptibility of the undoped  $\text{Gd}_2\text{O}_3$  particles is larger than that of the other two samples. Huang et al. show for heavy rare-earth metallofullerenes (heavy rare-earth on  $\text{C}_{82}$ ) that magnetic anisotropy is induced by the non-zero orbital angular momentum of heavy rare-earth ions, and the anisotropy causing a negative effect on the magnetization.<sup>100</sup> The zero

orbital angular momentum  $Gd^{3+}$  ions have an isotropic electron distribution owing to their spherical electron distribution, so that they are not influenced by the anisotropy effect. The anisotropy in the Eu-doped samples causes larger negative deviations from the linear field-dependent magnetization curves under a stronger external field. Therefore, the Eu-doped samples have higher susceptibilities at low external field than the undoped sample, but as the external field is increased, the susceptibilities become weaker compared to those of the undoped samples. This is due to the anisotropy effect.<sup>100</sup>

According to the XMCD studies in combination with AAS results, the Eu-doped samples have a lower total magnetization at 6 T than the undoped  $Gd_2O_3$  sample.  $Gd^{3+}$  ions have an average magnetization of 4.32-4.87  $\mu_B/Gd$  (see Table 4.1.1), Eu ions have an average magnetization of 0.47-0.57  $\mu_B/Eu$  (see Table 4.1.2) and the ratio of Eu/Gd in the Eu-doped samples is around 1:4, as follows from AAS results. In the most extreme case, the undoped  $Gd_2O_3$  sample has  $4.32 \times 100\% = 4.32 \mu_B/\text{lanthanide ion}$ , and the Eu-doped samples have  $4.87 \times 80\% + 0.57 \times 20\% = 3.94 \mu_B/\text{lanthanide ion}$ . As a result, the findings from SQUID fully confirm the XMCD results at an external field of 6 T. Although the difference in the magnetization between the undoped sample and the Eu-doped one at above 5 T is not significant, it is evident that the Eu-doped sample does not necessarily have weaker total magnetization than the undoped sample. According to the samples under study and the investigations in SQUID and XMCD studies, it is concluded that the total magnetization of the Eu-doped samples can be enhanced by lowering the Eu-content when it is exposed to a higher external field, or by lowering the external field while keeping the Eu/Gd ratio constant.

As for the annealing effect, it is clear from both XMCD and SQUID studies that an annealing process can improve the total magnetization of the sample. It is possible that longer annealing times or higher annealing temperatures may enhance the magnetization of the sample further.

To obtain the effective magnetic moment of the sample, the reciprocal susceptibility curves of the three samples are shown as a function of temperature at 100 mT in Figure

4.1.9. Initially magnetization curves as a function of temperature are measured at 100 mT and the temperature is varied from 5 K to 315 K. The magnetization curves are divided by the external magnetic field 100 mT to give susceptibility curves as a function of temperature. The susceptibility is defined in Equation 2.2.1 which is the ratio between the obtained magnetization and the external magnetic field. Finally, the reciprocal susceptibility curves are used in Figure 4.1.9 for the purpose to calculate the effective magnetic moments.

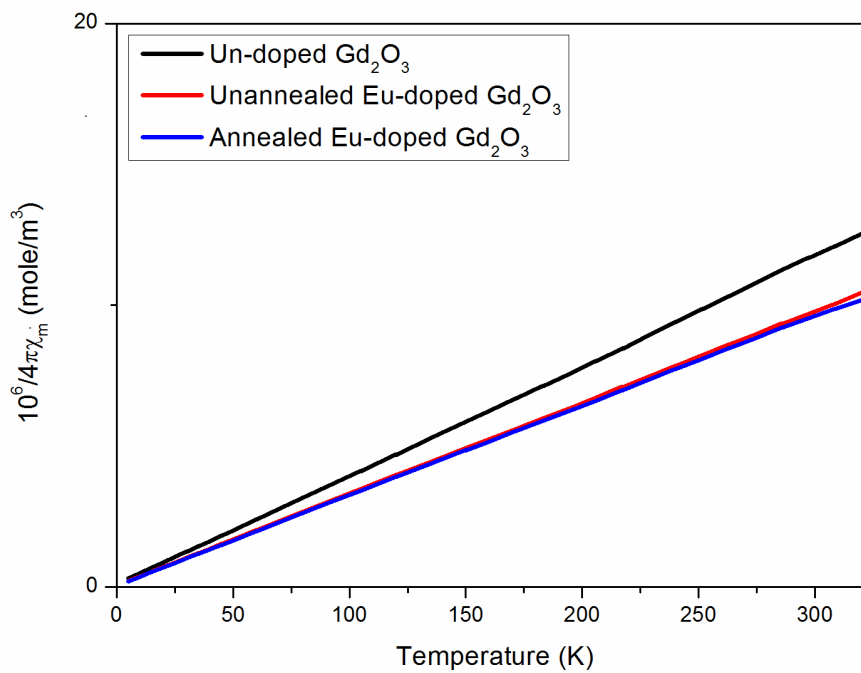


Figure 4.1.9: Reciprocal susceptibility curves as a function of temperature for the undoped  $Gd_2O_3$  sample, the unannealed Eu-doped  $Gd_2O_3$  sample, and the annealed Eu-doped  $Gd_2O_3$  sample. All measurements were taken at an external magnetic field of 100 mT.

The molar susceptibility can be further related as shown in Equation 4.1.7, where  $C_m$  is the molar Curie constant and T is temperature (K).

$$\chi_m(T) = C_m/T \quad (\text{Equation 4.1.7})$$

Figure 4.1.9 is derived by assuming that the net magnetization is dominated by  $Gd^{3+}$  ions, because there is only a limited contribution to the magnetization from Eu in the sample (see Table 4.1.2). The magnetization contributions of Eu ions are neglected in these SQUID measurements not only because the total magnetic moment obtained from XMCD is only about 10% in magnitude compared to  $Gd^{3+}$  ion, but also because of the much less magnetic  $Eu^{2+}$  content compared to the Gd content. Note that  $Eu^{3+}$  is non-magnetic. In addition, the composition between different magnetized  $Eu^{2+}$  and  $Eu^{3+}$  is unknown. Therefore, it is difficult to take magnetization contributions from Eu ions into account. The Curie constant is obtained by calculating the reciprocal slopes of the corresponding linear dependencies shown in Figure 4.1.9.

Furthermore, the effective magnetic moment is determined according to Equation 4.1.8, where  $N$  is Avogadro's number  $6.02 \times 10^{23} \text{ mol}^{-1}$ ,  $k$  is Boltzmann's constant  $1.38 \times 10^{-23} \text{ J/K}$ ,  $\mu_B$  is Bohr's magneton  $9.27 \times 10^{-24} \text{ J/T}$ , and  $\rho_{\text{eff}}$  is effective magnetic moment.

$$\rho_{\text{eff}} = \left( \frac{3kC_m}{N\mu_B^2} \right)^{1/2} \quad (\text{Equation 4.1.8})$$

The calculated effective magnetic moments per  $Gd^{3+}$  ion of the three samples under study are presented in Table 4.1.3. Here, the same trend as found as for the corresponding data obtained from XMCD measurements (see Table 4.1.1.) Both measurements show that  $Gd^{3+}$  ions in the Eu-doped samples possess a higher magnetic moment than in the undoped sample. The difference between these results is that XMCD studies measure directly the magnetic moment of the  $Gd^{3+}$  ions, whereas the data obtained from SQUID are based on the assumption that the magnetization contributed by other elements is negligible, and the measured magnetization is hence only averaged over the number of  $Gd^{3+}$  ions. Therefore, SQUID data might tend to overestimate the Gd magnetic moment, if other elements in the sample are also magnetic. A possible explanation has been given by Simon et al..<sup>89</sup> They stated that high  $Gd_2O_3$  concentrations in the matrix leads to antiferromagnetically coupled  $Gd^{3+}$ -O- $Gd^{3+}$  pairs, whereas most  $Gd^{3+}$  behaves as free  $Gd^{3+}$  ions. Therefore, the dopant Eu decreases the  $Gd_2O_3$  concentration and eliminates the antiferromagnetically coupled pairs.

Table 4.1.3: Magnetic moments per  $\text{Gd}^{3+}$  ion which are calculated according to Equation 4.1.7 and Equation 4.1.8, and Figure 4.1.9. The values Eu-doped samples may be less reliable due to the ignorance of the  $\text{Eu}^{2+}$  contribution.

	Undoped $\text{Gd}_2\text{O}_3$	Unannealed Eu-doped $\text{Gd}_2\text{O}_3$	Annealed Eu-doped $\text{Gd}_2\text{O}_3$
Magnetic moment/ $\text{Gd}^{3+}$ ( $\mu_B$ )	$4.52 \pm 0.01$	( $4.95 \pm 0.01$ )	( $4.99 \pm 0.01$ )

#### 4.1.4 Conclusions

Magnetic studies on undoped  $\text{Gd}_2\text{O}_3$  nanoparticles, unannealed Eu-doped  $\text{Gd}_2\text{O}_3$ , and annealed Eu-doped  $\text{Gd}_2\text{O}_3$  by XMCD measurements and SQUID measurements are shown to yield comparable results. The addition of Eu as a doping agent increases the magnetic moment per Gd ion (Table 4.1.1 and Table 4.1.3). However, the undoped sample which has larger Gd ratio compared to the other Eu-doped samples still has stronger magnetization per sample mass at the magnetic field larger than 5 T. An annealing process at  $140^\circ\text{C}$  for 30 h is able to enhance the net magnetic moment of the sample (Figure 4.1.8), but the difference is limited perhaps due to the insufficient annealing temperature or insufficient annealing period. Decreasing either the Eu/Gd ratio or the external field leads to a larger net magnetic moment in Eu-doped  $\text{Gd}_2\text{O}_3$  samples as compared to the undoped  $\text{Gd}_2\text{O}_3$  sample.

## **4.2 Magnetic Studies on Lanthanide-Doped NaGdF<sub>4</sub> Nanoparticles**

In order to eliminate the uncertainty of annealing effects between Eu-doped Gd<sub>2</sub>O<sub>3</sub> samples caused by the Eu in Chapter 4.1, a brief magnetic study on both unannealed and annealed Er (0.002%)-, Eu (5%)-, and Yb (18%)-doped NaGd(77%)F<sub>4</sub> nanoparticles in terms of SQUID measurements is discussed in this Chapter. The annealed sample was prepared by heating an unannealed one to 200°C for 70 h. This is accompanied with changes in sample size: the unannealed sample size was 12±2 nm, whereas the annealed one was slightly larger in size reaching 16±4 nm. Detailed sample information will be shown in Chapter 4.3.5. In addition, relaxometry measurements have been performed in order to understand if the gadolinium-contained nanoparticles are suitable magnetic resonance image contrast agents.

### **4.2.1 Superconducting Quantum Interference Device Studies**

The magnetization curves shown in Figure 4.2.1 have been normalized to the overall sample mass including the mass of ligands of the unannealed and annealed Er (0.002%)-, Eu (5%)-, and Yb (18%)-doped NaGd(77%)F<sub>4</sub> nanoparticles. The ligand mass is not eliminated from the overall sample mass because there is not only ligands but also other metals which may be either diamagnetic or magnetic existing in the sample and it is difficult to specify the mass and the magnetic contribution of each element. The surface ligand coverage is assumed to be similar because the ligand exchange processes were done under the same condition. Also, it is the whole sample that will be used in the applications, so it is useful to know the magnetic behavior of the whole sample. The effective magnetic moment will be calculated later through the results obtained from Figure 4.2.2.

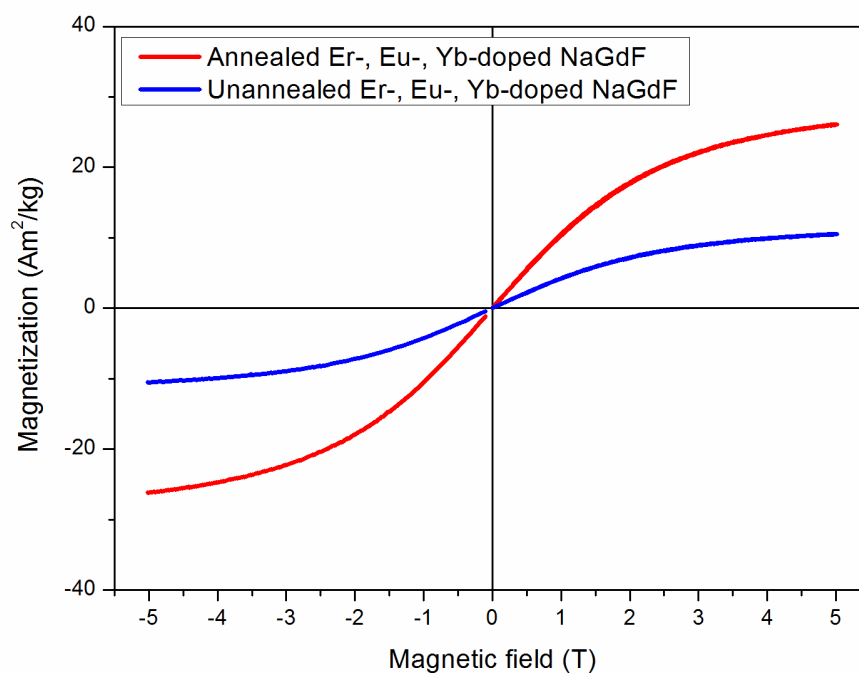


Figure 4.2.1: Magnetization curves of the unannealed and annealed Er (0.002%)-, Eu (5%)-, and Yb (18%)-doped NaGd(77%)F<sub>4</sub> nanoparticles as a function of applied magnetic field ranging from 0 T to 5 T measurement at 5 K. All of the curves are normalized to the corresponding sample mass.

When comparing unannealed and annealed Eu-doped Gd<sub>2</sub>O<sub>3</sub> samples with unannealed and annealed Er (0.002%)-, Eu (5%)-, and Yb (18%)-doped NaGd(77%)F<sub>4</sub> samples, it is found that the mass magnetic moments of the Er (0.002%)-, Eu (5%)-, and Yb (18%)-doped NaGd(77%)F<sub>4</sub> samples are much smaller than the Eu-doped Gd<sub>2</sub>O<sub>3</sub> nanoparticles. Both of the unannealed and annealed Eu-doped Gd<sub>2</sub>O<sub>3</sub> samples have magnetization which are approximately 60 Am<sup>2</sup>/kg under external field 5 T whereas the samples under study show only a magnetization of 10 Am<sup>2</sup>/kg for the unannealed sample and 26 Am<sup>2</sup>/kg for the annealed sample at 5 T. The reason to this is due to the fact that there are different ligands on the particles under study compared to the Eu-doped Gd<sub>2</sub>O<sub>3</sub> samples. The Eu-doped Gd<sub>2</sub>O<sub>3</sub> nanoparticles are coated by diethylene glycol in which the molecular weight is 106.12 g/mol, whereas the present samples are coated with PEO-

phosphate ligands and the average molecular weight is at least 7 times higher than that of diethylene glycol.

However, the annealed sample under study shows a large difference in the magnetization compared to the unannealed sample under study and has proved that an annealing process is able to enhance the magnetization of such samples. Likely, it is due to the higher annealing temperature and longer annealing times compared to the annealed Eu-doped  $Gd_2O_3$  sample which was annealed at  $140^\circ C$  for 30 hours. The stronger annealing condition enhanced the possibilities to eliminate the disorder in the crystal lattice, and hence the magnetic wall should be eliminated to improve the magnetization.

There are five metallic elements involved in the samples under study: Er, Eu, Yb, Na, and Gd. It has been shown in Chapter 4.1.1-4.1.2 that Gd ions usually exist as  $Gd^{3+}$  and Eu ions exist as  $Eu^{2+}$  and  $Eu^{3+}$ . The molar magnetic susceptibilities of  $Na^+$  and  $Yb^{3+}$  are significantly smaller ( $<10^{-4} \text{ cm}^3/\text{mol}$ ) than those of europium ( $Eu^{2+}$ :  $0.03 \text{ cm}^3/\text{mol}$ , and  $Eu^{3+}$ :  $0.01 \text{ cm}^3/\text{mol}$ ),  $Er^{3+}$  ( $0.07 \text{ cm}^3/\text{mol}$ ), and  $Gd^{3+}$  ( $0.05 \text{ cm}^3/\text{mol}$ ).<sup>101</sup> Therefore, their magnetic contribution can be neglected. In addition, the portions of erbium and europium ions are small (Er: 0.002%, and Eu: 5%) compared to that of gadolinium (77%) so that their magnetic contributions can also be neglected. Based on the assumption made above, reciprocal susceptibility curves as a function of temperature for the unannealed and annealed Er (0.002%)-, Eu (5%)-, and Yb (18%)-doped  $NaGd(77\%)F_4$  samples are presented in Figure 4.2.2. The procedures to obtain reciprocal susceptibility curves are shown in Chapter 4.1.3.

The effective magnetic moments per  $Gd^{3+}$  of both unannealed and annealed Er (0.002%)-, Eu (5%)-, and Yb (18%)-doped  $NaGd(77\%)F_4$  nanoparticles are calculated as described in Chapter 4.1.3. These are shown in Table 4.2.1. The effective magnetic moment of  $Gd^{3+}$  in the annealed sample is significantly enhanced compared to the unannealed sample. This result confirms the conclusion obtained from XMCD and SQUID measurements on  $Gd_2O_3$  nanoparticles indicating that the annealing process is able to improve magnetic moments of  $Gd^{3+}$  in nanoparticles.

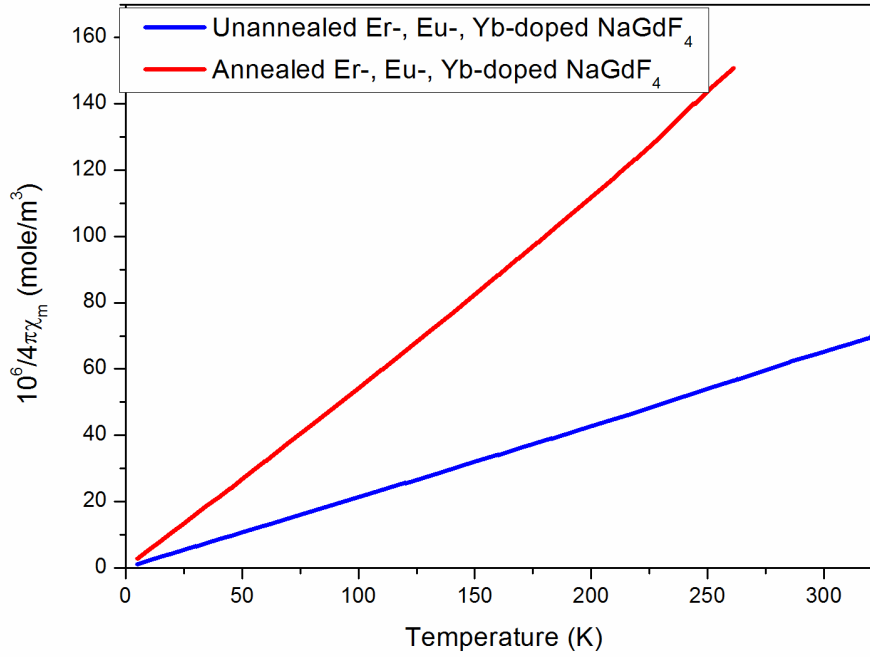


Figure 4.2.2: Reciprocal susceptibility curves as function of temperature for the unannealed and annealed Er (0.002%)-, Eu (5%)-, and Yb (18%)-doped NaGd(77%)F<sub>4</sub>. All measurements are carried out at an external magnetic field of 100 mT.

Table 4.2.1: Magnetic moment per Gd ion calculated in the application of Figure 4.2.2, Equation 4.1.7, and Equation 4.1.8.

	Unannealed Er-, Eu-, Yb-doped NaGdF <sub>4</sub>	Annealed Er-, Eu-, Yb-doped NaGdF <sub>4</sub>
Magnetic moment/ Gd <sup>3+</sup> (μ <sub>B</sub> )	3.7±0.3	6.1±0.5

## 4.2.2 Relaxometry Measurements

Due to the presence of Gd in the sample, Gd-based nanoparticles are expected to be a potential candidate for being used as a  $T_1$ -weighted MRI contrast agent. Therefore, comparisons were made between the currently applied MRI contrast agent Magnevist<sup>®</sup> and lanthanide-doped NaGdF<sub>4</sub> nanoparticles. Magnevist<sup>®</sup> is a trade mark produced by Bayer Schering Pharma, and it contains gadopentetic acid which is a salt of a complex of gadolinium with diethylenetriaminepentacetate (DTPA). The particles used here for relaxometry measurement are Er (0.002%)-, Eu (2%)-, and Yb (18%)-doped NaGd(80%)F<sub>4</sub> particles. Their TEM image is shown in Figure 4.2.3. The average size of the particles is  $16 \pm 3$  nm.

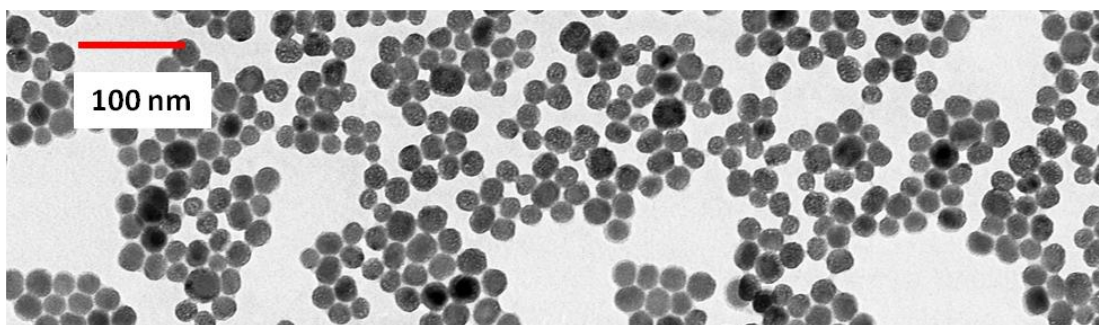


Figure 4.2.3: TEM image of Er (0.002%)-, Eu (2%)-, and Yb (18%)-doped NaGd(80%)F<sub>4</sub> nanoparticles.

MRI relaxation images of the reference material Magnevist<sup>®</sup> and Er (0.002%)-, Eu (2%)-, and Yb (18%)-doped NaGd(80%)F<sub>4</sub> nanoparticles are shown in Figure 4.2.4 and Figure 4.2.5, respectively. Five samples of both Magnevist<sup>®</sup> and Er (0.002%)-, Eu (2%)-, and Yb (18%)-doped NaGd(80%)F<sub>4</sub> in different concentrations plus two blank samples (distilled water) are measured at the same time so that the experimental condition, the echo time, and repetition time, are identical for these studies. The MRI relaxation images help us to quantify the contrast properties of the contrast agents. It is the same as what can be seen in the magnetic resonance images. One can directly see how the blank solution does look like and how the interactions between water and contrast agents change the images when additives to the contrast agents are applied. When a  $T_1$ -weighted contrast agent interaction with water, it can accelerate the radio

frequency-excited proton spins to release their excess energies and give white-contrasted magnetic resonance images. The detailed processes to describe how the magnetic resonance images are produced are discussed in Chapter 4.1.2.

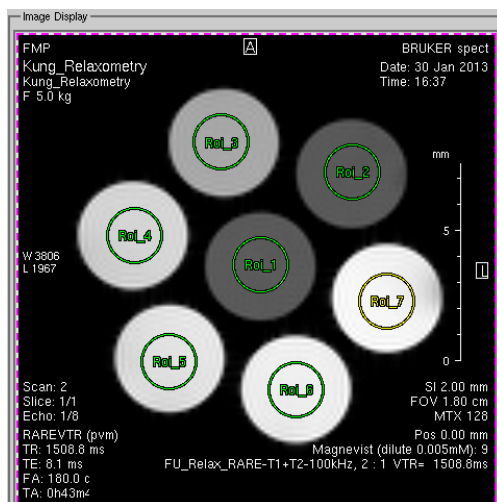


Figure 4.2.4: Magnetic resonance images for the reference material Magnevist<sup>®</sup>. The darkest two circles are blank reference samples without addition of a contrast agent, Magnevist<sup>®</sup>, and the concentration of Magnevist<sup>®</sup> is increasing counter-clockwisely.

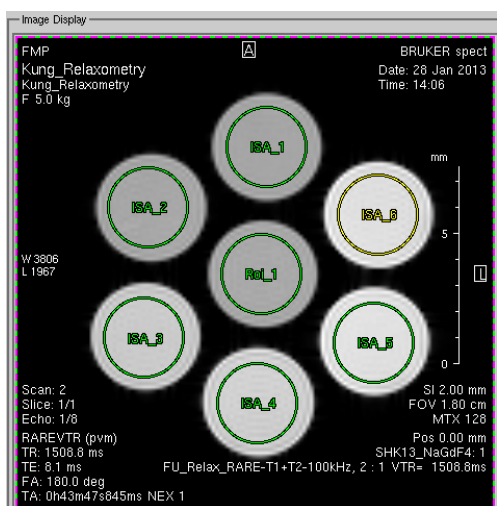


Figure 4.2.5: Magnetic resonance images for Er (0.002%)-, Eu (2%)-, and Yb (18%)-doped NaGd(80%)F<sub>4</sub> nanoparticles. The darkest two circles in the middle vertical line are blank references samples without addition of a contrast agent. The concentration of the contrast agent is increased counter-clockwisely.

It can be seen that the difference between the blank solution (the darkest two circles, Roi\_1 and Roi\_2 in Figure 4.2.4, Roi\_1 and ISA\_1 in Figure 4.2.5) and the solution with the highest concentration (the brightest circle, Roi\_7 in Figure 4.2.4, ISA\_6 in Figure 4.2.5) are much stronger in the Magnevist<sup>®</sup> contrasted images than those of the lanthanide-doped NaGdF<sub>4</sub>. As proved by atomic absorption spectra, it is known that the Gd concentrations are more than 100 times higher in the sample under study compared to the reference Magnevist<sup>®</sup> samples. This means that the contrast ability of the Magnevist<sup>®</sup> is much stronger compared to that of the lanthanide-doped NaGdF<sub>4</sub> nanoparticles. However, images in Figure 4.2.5 prove that these particles have potential to be a T<sub>1</sub>-weighted contrast agent. As the concentrations are taken into account, the relaxation rate r<sub>1</sub> and r<sub>2</sub> values are calculated and the results are presented in Table 4.2.2.

Table 4.2.2: Relaxation rates, r<sub>1</sub> and r<sub>2</sub>, of Magnevist<sup>®</sup> and Er (0.002%)-, Eu (2%)-, and Yb (18%)-doped NaGd(80%)F<sub>4</sub> nanoparticles. The measurements are achieved at 7 T and 310 K.

	Magnevist <sup>®</sup>	Lanthanide-doped NaGdF <sub>4</sub>
r <sub>1</sub> /Gd (mM <sup>-1</sup> s <sup>-1</sup> )	4.5±0.2	0.33±0.1
r <sub>2</sub> /Gd (mM <sup>-1</sup> s <sup>-1</sup> )	5.9±0.2	32±3

Table 4.2.2 shows that Magnevist<sup>®</sup> has a higher r<sub>2</sub> value than r<sub>1</sub> value as a T<sub>1</sub>-weighted MRI contrast agent, and that the r<sub>1</sub>-to-r<sub>2</sub> ratio of it is 73 times larger than that of the lanthanide-doped NaGdF<sub>4</sub> nanoparticles. For T<sub>1</sub>-weighted contrast agents, the r<sub>1</sub>-to-r<sub>2</sub> ratio should be large. However, r<sub>1</sub> is always smaller than r<sub>2</sub> according to the reported data in the literature.<sup>2</sup> This is possible because the T<sub>2</sub> relaxation processes are much faster than the T<sub>1</sub> relaxation process, so that their contrast abilities occur on different time scales. Also, when one adds a contrast agent into a sample, both T<sub>1</sub> and T<sub>2</sub> relaxation will be altered. Therefore, a high T<sub>1</sub>-weighted contrast agent should show a high r<sub>1</sub>-to-r<sub>2</sub> ratio. Due to the small r<sub>1</sub>-to-r<sub>2</sub> ratio of Er (0.002%)-, Eu (2%)-, and Yb (18%)-doped NaGd(80%)F<sub>4</sub> nanoparticles, it is concluded that these particles are a better T<sub>2</sub>-weighted contrast agent than a T<sub>1</sub>-weighted contrast agent.

The best condition for Gd<sup>3+</sup> to shorten the T<sub>1</sub> relaxation time of a water molecule is that Gd<sup>3+</sup> is in direct contact.<sup>102</sup> The commercially available Magnevist<sup>®</sup> is the complex of Gd<sup>3+</sup> and DTPA<sup>5-</sup>, and the gadolinium ion is nine fold coordinated, it is surrounded by 3

nitrogen atoms and 5 oxygen atoms from the carboxylate groups. The ninth coordination site is occupied by a water molecule where this water molecule can be replaced rapidly by other water molecules that are located near the complex. As a result, one Magnevist<sup>®</sup> complex can relax several proton spins by direct contacting the neighboring water molecules. In Gd-based nanoparticles only Gd<sup>3+</sup> on the surface can efficiently fulfill this function. However, all Gd<sup>3+</sup> ions are taken into account when the relaxation rates are calculated. The  $r_1$  and  $r_2$  values are normalized to the total Gd concentration in the particles. Therefore, the relaxation rate of the lanthanide-doped NaGdF<sub>4</sub> is averaged and it is therefore much smaller. The advantage of Magnevist<sup>®</sup>, which is consisting of gadopentetic acid molecules, is that all Gd<sup>3+</sup> can directly interact with water. Johnson et al. have shown for pure NaGdF<sub>4</sub> particles that as the particles size is decreased, the MR relaxivity is enhanced.<sup>7</sup> Their 2.5 nm NaGdF<sub>4</sub> particles have  $r_1$  value of  $7.2 \pm 0.2 \text{ mM}^{-1} \text{ s}^{-1}$ . Dong et al. presented their work on Tm-, Yb-doped NaYF<sub>4</sub> core with a 0.6 nm NaGdF<sub>4</sub> shell which contains 29.7% Gd in the particles, and the  $r_1$ ,  $r_2$  values they derived are  $1.36 \pm 0.01 \text{ mM}^{-1} \text{ s}^{-1}$   $106 \pm 5 \text{ mM}^{-1} \text{ s}^{-1}$ , respectively.<sup>103</sup>

According to the reported data, it is known that the results we obtained from the present studies are reasonable. In order to improve the  $r_1$  relaxivity, the particles size needs to be reduced to 2.5 nm. A core shell structure is not quite efficient compared to small size particles. In addition, the ligand density of the particles also needs to be considered since particles with high surface ligand density also reduce the performance of the surface-bound Gd.

### 4.2.3 Conclusions

The SQUID data shown in Chapter 4.2.1 show clear magnetization enhancement after an annealing process at 200 °C for 70 h which is corresponding to the conclusion obtained from Chapter 4.1.1 to Chapter 4.1.2. Both, the unannealed and annealed Er (0.002%)-, Eu (5%)-, and Yb (18%)-doped NaGd(77%)F<sub>4</sub> nanoparticles are superparamagnetic at 5 K.

Relaxometry measurements show that the Er (0.002%)-, Eu (2%)-, and Yb (18%)-doped NaGd(80%)F<sub>4</sub> nanoparticles can be T<sub>1</sub>-weighted contrast agents, as shown in Figure 4.2.5. However, the contrast ability of commercially available Magnevist<sup>®</sup> is much higher than the samples under study. To enhance the contrast ability of the nanoparticles prepared in this work, the particles size needs to be reduced. In addition, the ligand concentration bound to the particle surface needs to be decreased, which is due to the interaction of water with Gd ions.

## 4.3 Optical Studies on Eu-, Er-, and Yb-Doped NaGdF<sub>4</sub> Nanoparticles

Many upconversion studies on rare earths have been performed since the 1960s.<sup>41,68,104-106</sup> Investigations focus recently especially on Er- and Yb-doped NaYF<sub>4</sub> nanoparticles which are due to the high upconversion efficiency in Er transitions. Many of the Er transition energies are nearly equal or proportional to the transition energy of ionic ytterbium (Figure 4.3.25). In addition, Eu ions are frequently chosen among all lanthanide ions as one of the most efficient fluorescent elements for fluorophores. Based on these two facts, this Chapter is focused on the fluorescent and upconversion behavior of Eu-, Er-, and Yb-doped NaGdF<sub>4</sub> nanoparticles.

Primary research on Eu ions in NaGdF<sub>4</sub> particles and the distinct optical properties of Eu-, and Er-contained Yb-doped NaGdF<sub>4</sub> particles is discussed in the beginning (Chapter 4.3.1-4.3.2), followed by investigations on variation of dopants (Chapter 4.3.3), size effects (Chapter 4.3.4), and annealing effects (Chapter 4.3.5) on Eu-, and Er-contained, Yb-doped NaGdF<sub>4</sub> nanoparticles. Mainly, the optical efficiencies and lifetimes aspects are discussed. In the end, an energy transfer route will be proposed that is based on all information obtained from Chapter 4.3.1 to Chapter 4.3.5. This is shown in Chapter 4.3.6.

### 4.3.1 Eu Ions in NaGdF<sub>4</sub> Nanoparticles

Three samples were prepared to study the optical behavior of europium: an undoped NaEuF<sub>4</sub> sample, a 10% Eu-doped NaGdF<sub>4</sub> sample, and an undoped NaGdF<sub>4</sub> sample. TEM images of these samples are shown in Figure 4.3.1; particles in the same size range can be seen in all three Figures without particle aggregation. The average particle sizes are 9±2 nm for both of the undoped NaGdF<sub>4</sub> and 10% Eu-doped NaGdF<sub>4</sub> samples, and we also assume that the undoped NaEuF<sub>4</sub> sample with an average size of 11±2 nm is in the same size range as the other samples mentioned above due to the overlap size distribution.

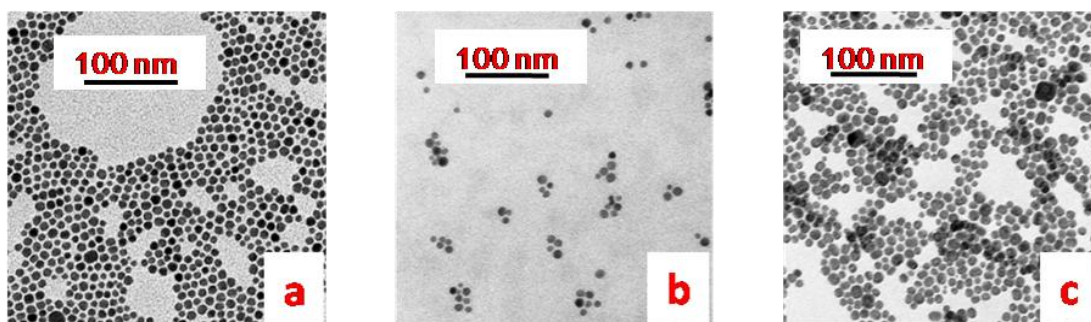


Figure 4.3.1: TEM images of (a) NaGdF<sub>4</sub> (9±2 nm), (b) 10% Eu-doped NaGdF<sub>4</sub> (9±2 nm) and (c) NaEuF<sub>4</sub> (11±2 nm) samples.

The particle surfaces of these three samples were originally coated with oleic acid and are modified by PEO-diphosphonate ligands with ligand exchange processes (Chapter 3.2.7) before the samples are suspended in ultrapure water. Emission spectra of these samples are recorded by the same spectrometer using same experimental conditions (Figure 4.3.2). The precise positions of emission peaks are summarized in Table 4.3.1. Since the emission peaks of Gd ions are in the UV regime,<sup>107</sup> we recorded spectra (Figure 4.3.2) in the range between 500 nm and 750 nm which includes all typical emission peaks of Eu in the visible regime.<sup>108</sup>

The undoped NaGdF<sub>4</sub> spectrum is noisy due to the fact that no Gd emissions occur in the visible regime; when the spectrum is normalized to its intensity maximum, only the noise level is amplified, as is supported by the original data (Figure 4.3.2, inset) which shows essentially a flat line when compared to the other spectra. Both, undoped NaEuF<sub>4</sub> and 10% Eu-doped NaGdF<sub>4</sub> samples show typical Eu transitions in the spectra;<sup>109</sup> especially <sup>5</sup>D<sub>0</sub>→<sup>7</sup>F<sub>J</sub> transitions, where J is 1-4, and <sup>5</sup>D<sub>1</sub>→<sup>7</sup>F<sub>J</sub> transitions, where J is 3-5, can be assigned in both spectra. This is unlike the 10% Eu-doped NaGdF<sub>4</sub> sample, <sup>5</sup>D<sub>1</sub>→<sup>7</sup>F<sub>J</sub> transitions, where J is 0-2, and the <sup>5</sup>D<sub>2</sub>→<sup>7</sup>F<sub>3</sub> transition are missing in the undoped NaEuF<sub>4</sub> sample. The difference between these two spectra is due to cross relaxations between Eu ions. A cross relaxation process happens between the same types of ions which is also called self-quenching.<sup>110</sup> In the case of the undoped NaEuF<sub>4</sub> sample, in which the concentration of Eu is high, therefore the distance between two neighboring Eu ions is small enough for efficient energy transfer.<sup>111,112</sup> Then, excited Eu ions in the <sup>5</sup>D<sub>1</sub> and <sup>5</sup>D<sub>2</sub> levels transfer their energies to another neighboring Eu in a non-radiative

process which decreases the probability of  ${}^5D_{1-2} \rightarrow {}^7F_J$  emissions. When the overall fluorescence intensities in the original spectra (Figure 4.3.2, inset) are integrated separately, as the Eu content is decreased to 10%,  $43 \pm 1.4\%$  of the Eu fluorescence yield remains. Note that the error limit was obtained from repeated experiments, in which 20 spectra in the first 100  $\mu\text{s}$  after the excitation pulse were recorded. In other words, Eu ions perform, as a doping agent, efficient fluorescence in  $\text{NaGdF}_4$  hosts. This enables the potential of a multifunctional material.

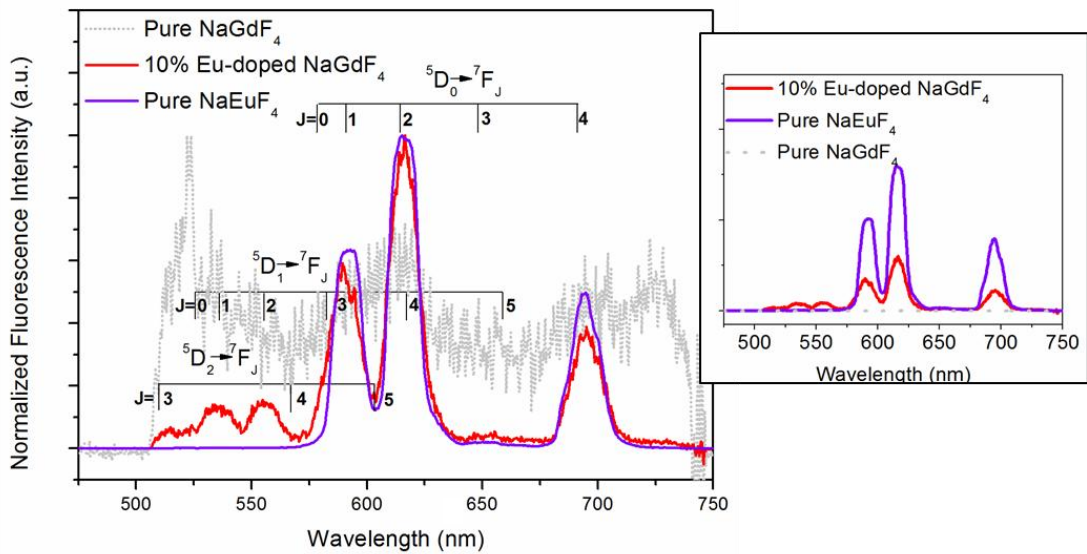


Figure 4.3.2: Eu transitions and fluorescence spectra of the undoped  $\text{NaGdF}_4$  (light gray dots), 10% Eu-doped  $\text{NaGdF}_4$  (red solid line), and undoped  $\text{NaEuF}_4$  (violet solid line) samples. The samples were excited at 464 nm and all obtained spectra are normalized with respect to their intensity maxima. The inset corresponds to emission spectra which were directly obtained from the spectrometer without further normalization, and the vertical axis represents the relative fluorescence intensity in arbitrary units.

The time-dependent optical properties of the two samples containing Eu were derived from lifetime measurements. Decay curves (Figure 4.3.3) with respects to different emission transitions are summarized in Table 4.3.1. The lifetimes shown in Table 4.3.1 were extracted from a series of the box-car fluorescence measurements; fluorescence counts of each spectrum collected at different time after a pulsed excitation were

integrated over the corresponding transition range; the integration values ( $y$ ) were plotted as a function of time ( $t$ ) after pulsed excitations and the obtained decay curves were fitted by a mono-exponential decay function (Equation 4.3.1) in order to derive the lifetimes ( $\tau$ ) of Eu transitions. Note that all decay curves were taken from the highest intensity point, i.e. they do not contain the rise in signals after excitations.

$$y(x) = A \times e^{-\frac{t}{\tau}} \quad \text{Equation 4.3.1}$$

$A$  describes the amplitude of the component right after the pulsed excitation ( $t=0$ ) and  $\tau$  is the lifetime.

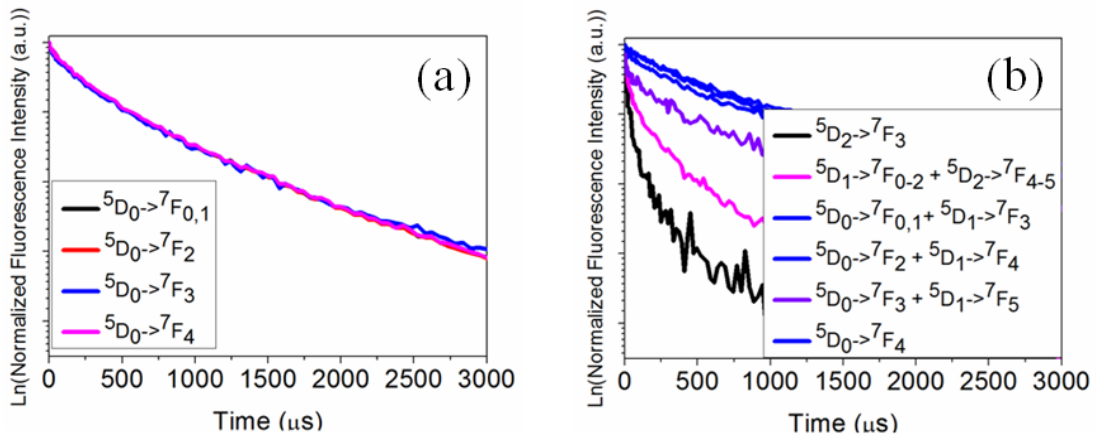


Figure 4.3.3: Fluorescence decay curves on a natural logarithmic scale of the (a) undoped NaEuF<sub>4</sub>, and (b) 10% Eu-doped NaGdF<sub>4</sub> samples at different Eu transitions.

From the undoped NaEuF<sub>4</sub> sample (see Figure 4.3.3 (a)) it is clear that all decay times are due to the same emitting level (<sup>5</sup>D<sub>0</sub>), since cross relaxations inhibit transitions of the <sup>5</sup>D<sub>1</sub> and <sup>5</sup>D<sub>2</sub> levels and the lifetimes are always in the same range (665-675 μs, see Table 4.3.1). When Eu serves as a doping agent in the NaGdF<sub>4</sub> dominated nanocrystals, the lifetime of almost every transition is changed and the most populated transition in Figure 4.3.2 has a longer lifetime (820 μs) than is observed for the undoped NaEuF<sub>4</sub> sample (675 μs). This is due to the fact that even the smallest energy gap between the Gd emitting state and the ground state is too large to absorb the excitation light (Figure 4.3.25) so that Gd ions do not cause extra energy transfer.

Table 4.3.1: The fluorescence lifetimes of the 10% Eu-doped NaGdF<sub>4</sub> and the undoped NaEuF<sub>4</sub> samples at different Eu transitions. The unit of lifetimes shown in the Table is microseconds ( $\mu$ s).  $R^2$  is obtained from the fitting procedure.

Transitions	${}^5D_2 \rightarrow {}^7F_3$	${}^5D_1 \rightarrow {}^7F_{0-2}$ +	${}^5D_0 \rightarrow {}^7F_{0-1}$ +	${}^5D_0 \rightarrow {}^7F_2$ +	${}^5D_0 \rightarrow {}^7F_3$ +	${}^5D_0 \rightarrow {}^7F_4$
		${}^5D_2 \rightarrow {}^7F_{4-5}$	${}^5D_1 \rightarrow {}^7F_3$	${}^5D_1 \rightarrow {}^7F_4$	${}^5D_1 \rightarrow {}^7F_5$	
Peak positions (nm)	515	525-570	590	615	650	695
10% Eu-doped NaGdF <sub>4</sub>	43 $\pm$ 2 ( $R^2 \geq 0.96$ )	130 $\pm$ 9 ( $R^2 \geq 0.94$ )	670 $\pm$ 20 ( $R^2 \geq 0.99$ )	760 $\pm$ 10 ( $R^2 \geq 0.996$ )	460 $\pm$ 30 ( $R^2 \geq 0.95$ )	820 $\pm$ 20 ( $R^2 \geq 0.996$ )
Undoped NaEuF <sub>4</sub>	-	-	672 $\pm$ 9	668 $\pm$ 9	665 $\pm$ 10	675 $\pm$ 9

Therefore, it is rather assumed that there is an energy transfer between the Eu ions, and the small Eu concentration reduces non-radiative cross-relaxations and hence increases the observed lifetimes. The decay of the  ${}^5D_0 \rightarrow {}^7F_4$  transition gives a non-interfering decay time for  ${}^5D_0 \rightarrow {}^7F_{0-4}$  transitions of Eu in this sample since no other transitions are taking place in the range between 675 nm and 725 nm (see Figure 4.3.2). The relaxation time of  ${}^5D_0 \rightarrow {}^7F_2$  is also similar to that of  ${}^5D_0 \rightarrow {}^7F_4$  since its transition population is sufficiently strong to neglect the blending which is caused by the  ${}^5D_1 \rightarrow {}^7F_4$  transition. Relaxation times of the  ${}^5D_0 \rightarrow {}^7F_1$  and  ${}^5D_0 \rightarrow {}^7F_3$  transitions have stronger deviations because of their insufficient fluorescence intensities, and the interference is driven by both  ${}^5D_1 \rightarrow {}^7F_3$  and  ${}^5D_1 \rightarrow {}^7F_5$  transitions. Therefore, these values are not reliable which is also confirmed by the small value of  $R^2$  shown in Table 4.3.1. Note that  $R^2$  in the table stands for adjust  $R^2$  values which are obtained from the fitting procedure and describe the reliabilities of the calculated lifetimes.

It is reasonable to point out that when describing fluorescence relaxations of the NaEuF<sub>4</sub> and Eu-doped NaGdF<sub>4</sub> samples, the decay time of the  ${}^5D_0 \rightarrow {}^7F_4$  transition represent the "real" fluorescence behavior of the  ${}^5D_0$  energy level, as is explained above. The  ${}^5D_{1,2} \rightarrow {}^7F_{0-2}$  transitions have much shorter relaxation times compared to  ${}^5D_0 \rightarrow {}^7F_{1-4}$  transitions. This is due to the fact that more ions in  ${}^5D_1$  and  ${}^5D_2$  energy levels undergo non-radiative

relaxations because of the small energy gap between the  $^5D_0$ ,  $^5D_1$ , and  $^5D_2$  states (Figure 4.3.25).

Chen et al.<sup>113</sup> described the fluorescence decay behavior of 7 nm Tm-doped NaYbF<sub>4</sub> nanocrystals by a bi-exponential function. Their explanation accounts for two relaxation times which were attributed to the location of Tm ions in different environments, i.e. The Eu ions close to the particle surface lead to a shorter decay time, because surface imperfections shorten the relaxation time, whereas the bulk Eu ions lead to a longer relaxation time. The latter also indicates a more stable environment for fluorescence processes. This explanation is also proved by their work where they coated a surface layer of the nanocrystals. Then, surface imperfections are suppressed by the additional NaGdF<sub>4</sub> shell and the decay processes can be described by a mono-exponential function without surface imperfection-induced relaxations. In comparison to the work of Chen et al., it can be stated that both of the present samples have a homogenous environment and evidently surface imperfections do not play a major role.

In conclusion, when we compare samples of the undoped NaGdF<sub>4</sub>, 10% Eu-doped NaGdF<sub>4</sub>, and undoped NaEuF<sub>4</sub>, we can prove that there are no Gd emissions observed and only 10% of Eu ions yield 44% of the NaEuF<sub>4</sub> fluorescence intensity. This is due to the fact that a higher Eu content may lead to self-quenching and hence this may also decrease the fluorescence efficiency. In addition, when Eu ions are put into NaGdF<sub>4</sub> nanoparticles, the characteristic lifetimes of Eu can be enhanced by a factor of 1.2. In other words, we can dope Eu ions onto NaGdF<sub>4</sub> hosts without a loss in fluorescence efficiency. It is also worthwhile to note that relaxations from the same emitting energy level yield similar decay times.

### 4.3.2 Eu and Er Ions in NaGdF<sub>4</sub> Nanoparticles

In this Chapter, differences between Eu and Er ions in the same sample are discussed regarding their fluorescence and upconversion properties. The sample under study is Er-, Eu-, and Yb-doped, NaGdF<sub>4</sub> nanoparticles where the relative molar ratio of Gd:Yb:Eu:Er in the overall rare earth content is 80:18:2:0.002. A TEM image of this sample is shown in Figure 4.3.4, in which the average particles size is 17±4 nm.

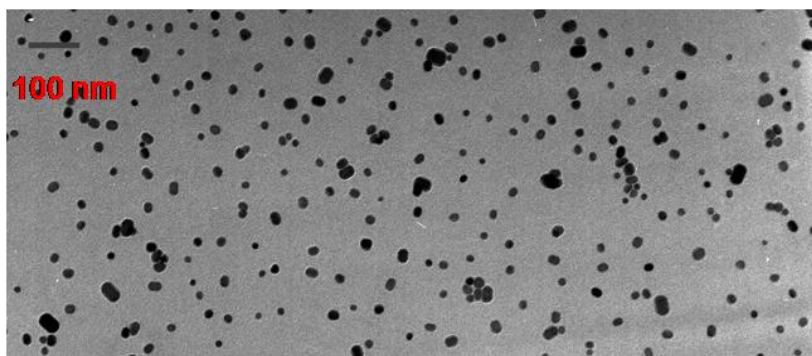


Figure 4.3.4: The TEM image of Er (0.002%)-, Eu (2%)-, and Yb (18%)-doped NaGd(80%)F<sub>4</sub> nanoparticles.

The particle surface of this sample is modified by PEO-diphosphonate ligands (cf. Chapter 3.2.6). This sample was measured as solid powder by both fluorescence and upconversion measurements. The fluorescence spectrum shown in Figure 4.3.5 was excited at 394 nm and recorded from 475-750 nm. Using these excitation conditions, a series of time-resolved fluorescence spectra was recorded using box car method. Time-dependent information is also extracted providing fluorescence decay curves (Figure 4.3.6) and fluorescence relaxation times (Table 4.3.3).

Only Er and Eu are possible to be fluorescent in this spectral range, because Yb emits light in the IR regime and Gd in the UV regime. However, there are differences between the Eu fluorescence spectrum of 10% Eu-doped NaGdF<sub>4</sub> nanoparticles (see Figure 4.3.2) and the Eu fluorescence spectrum of Er (0.002%)-, Eu (2%)-, and Yb (18%)-doped NaGd(80%)F<sub>4</sub> nanoparticles (see Figure 4.3.5). The most obvious difference is that

more transitions appear in Er-, Eu-, and Yb-doped NaGdF<sub>4</sub> nanoparticles and there are two possible reasons for this result.

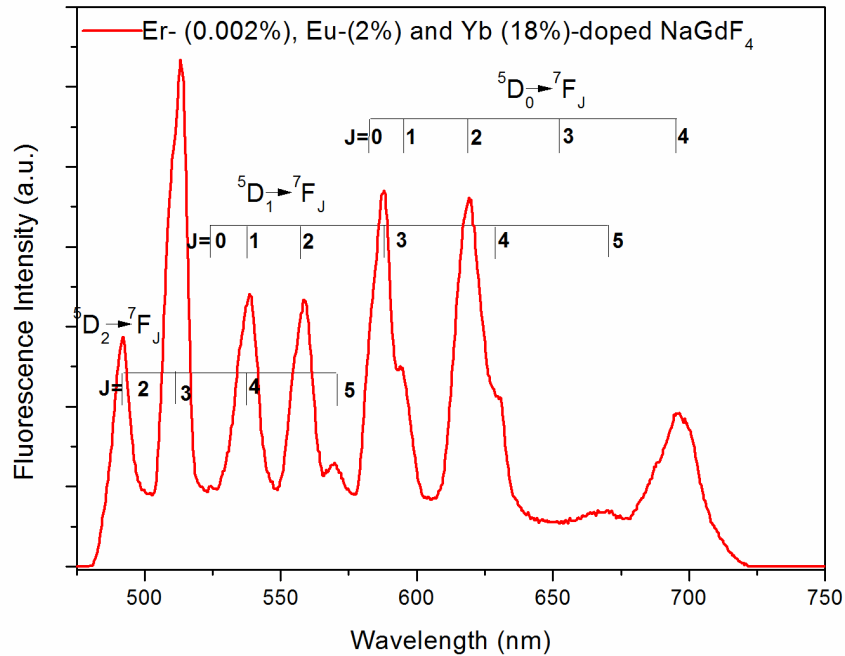


Figure 4.3.5: Eu transitions and fluorescence spectrum of Er-, Eu-, and Yb-doped NaGdF<sub>4</sub> nanoparticles. The sample was excited at 394 nm.

- Different excitation wavelengths and different host matrices: although  $4f$ -electrons in Eu ions are shielded by the outer  $5s$ - and  $5p$ -electrons, there is still a slight (smaller than 5 nm) shift of the transitions between different matrix hosts, which is due to the crystal field produced by the electric field of the surroundings of the excited site.<sup>41</sup> It is found that excitation wavelengths near 396 nm instead of 464 nm yielding fluorescence spectra like in Figure 4.3.2 can be absorbed more efficiently by Er-, Eu-, and Yb-doped NaGdF<sub>4</sub> nanoparticles. The energy level diagram clearly indicates (see Figure 4.3.25), that the excitation wavelength of 396 nm gives more energy than is required for an electronic excitation from the electronic ground state to the  $^5D_2$  level. This increases the probability of Eu relaxations from the  $^5D_2$  and  $^5D_1$  levels compared to spectra excited at 464 nm.
- Different Eu concentration: as already mentioned in Chapter 4.3.1, a higher concentration of Eu ions will lead to self-quenching of the fluorescence. The low

Eu concentration (2%) in the sample under study compared to 10% Eu-doped NaGdF<sub>4</sub> nanoparticles is therefore another plausible reason for the observed results.

According to Song et al., the fluorescence transitions of Er are caused by both nonradiative decay from <sup>2</sup>H<sub>11/2</sub> and cross relaxations from <sup>4</sup>G<sub>11/2</sub> to <sup>2</sup>H<sub>11/2</sub> or <sup>4</sup>S<sub>3/2</sub>, so that it is found that an excitation wavelength of 377 nm increases the Er fluorescence efficiently compared to other excitation conditions.<sup>114</sup> Therefore, it has also been tried to take the fluorescence spectrum of Er at 377 nm using the present sample. However, no transition peaks of Er, at 525 nm, 543 nm, and 650 nm can be observed above the background level. Evidently, Er ions absorb radiation of 377 nm poorly. There are two possible reasons for this result: (i) firstly this might be due to the fact that the Er content is too low in the sample compared to the Eu content (see Table 4.3.2, the elemental concentration measured by neutron activation analysis), (ii) Er ions absorb the exciting radiation in the UV regime less efficiently than Eu ions. As a result, it is sure that Eu ions give more intense fluorescence signals than Er ions in Er (0.002%)-, Eu (2%)-, and Yb (18%)-doped NaGd(80%)F<sub>4</sub> nanoparticles. Therefore, only Eu shows observable fluorescence emissions as the sample is excited by light in the UV-/near UV-regime.

Table 4.3.2: Neutron activation analysis results of the sample Er (0.002%)-, Eu (2%)-, and Yb (18%)-doped NaGd(80%)F<sub>4</sub> nanoparticles. The rare earth content mentioned in the above text corresponds to the stoichiometry given by the ratio of the starting materials which were added during the particle preparation. The results from neutron activation analysis describe the rare earths content ratio in the final particles sample.

Element	(mg Eu/ Gd/ Yb)/(kg sample)	Standard deviation	mole%
Eu	1.895	0.008	2.2
Gd	68.3	1.8	76.7
Yb	20.72	0.26	21.1
Er	undetectable	-	-

Briefly, one can see that Eu emissions dominate the fluorescence spectrum recorded at 394 nm (cf. Figure 4.3.5). No Er emissions above the noise level can be observed at

excitation wavelengths of both 394 nm and 377 nm. The reason for the absence of Er emissions is due to the low Er content and the inefficient fluorescence of Er.

To continue time-dependent fluorescence studies of the sample containing Er (0.002%)-, Eu (2%)-, and Yb (18%)-doped NaGd(80%)F<sub>4</sub> nanoparticles, Figure 4.3.6 is obtained from a series of time-resolved spectra by the following procedure:

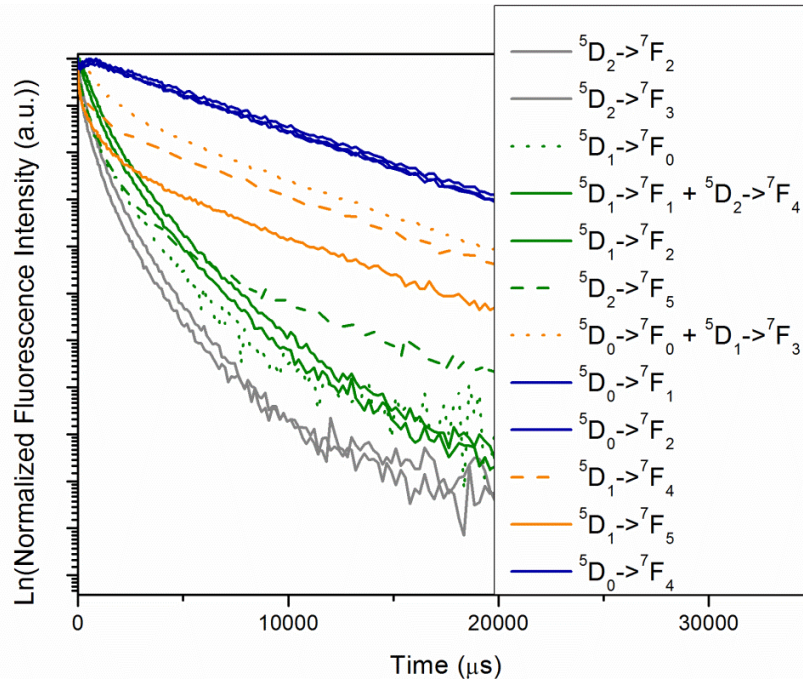


Figure 4.3.6: Normalized fluorescence decay curves in a natural logarithmic scale of Er (0.002%)-, Eu (2%)-, and Yb (18%)-doped NaGd(80%)F<sub>4</sub> nanoparticles at different Eu transitions.

- Firstly, 250 fluorescence spectra were recorded at different delay times after the pulsed excitations at 976 nm.
- Secondly, the fluorescence intensities of each peak are integrated separately in each spectrum. This requires 12 (peaks) × 250 (spectra) = 3000 integrations.
- Finally, the obtained integration values are plotted in a natural logarithmic scale against time for each transition.

- Due to blended transitions from different emitting states shown in Figure 4.3.6, the analysis is restricted to decay curves of “pure” transitions, so that complications of the analysis are avoided. As concluded in Chapter 4.3.1, transitions from the same emitting energy level should show a similar relaxation behavior. We use two colors of the “pure transitions” as shown in Figure 4.3.6, which are labeled according to the corresponding emitting levels. Blue and gray colors describe the real relaxation behavior because of their single transition positions, as shown in Figure 4.3.5. More specifically, blue colored curves describe the relaxation behavior of excited electrons in the  $^5D_0$  emitting level, and gray ones in the  $^5D_2$  emitting level. The other colors used in Figure 4.3.6 describe mixtures of different transitions, which explain bi-exponential curves. Decay curves and calculated lifetimes are shown in Table 4.3.3. Clearly, transitions starting from the  $^5D_0$  emitting level (blue curves) show the longest lifetimes compared to the other two emitting levels. Usually, emissions of Eu from the  $^5D_0$  emitting level are applied as fluorescence labels in time-resolved immunofluorometric assays, which is due to their large Stokes shift and extremely long fluorescence lifetimes ( $\mu\text{s}$  to  $\text{ms}$  range).<sup>115,116</sup>

Table 4.3.3: Fluorescence lifetimes of Er (0.002%)-, Eu (2%)-, and Yb (18%)-doped NaGd(80%)F<sub>4</sub> nanoparticles at different Eu transitions. The adjusted R<sup>2</sup> values of all mono-exponential fits are larger than 0.98. Even larger values (R<sup>2</sup> > 0.997) are obtained from bi-exponential fits. Numbers in parentheses in the last column describe the amplitudes of the component occurring right after the pulsed excitation (t=0).

Transition	Peak <sub> maximum</sub> (nm)	Lifetimes fit by an exponential function ( $\mu\text{s}$ )	Lifetimes fit by a bi-exponential function ( $\mu\text{s}$ )
$^5D_2 \rightarrow ^7F_2$	492	370±9	75±2 (0.43); 685±10 (0.52)
$^5D_2 \rightarrow ^7F_3$	513	429±7	146±5 (0.40); 790±10 (0.59)
$^5D_0 \rightarrow ^7F_{0,1}$ + $^5D_1 \rightarrow ^7F_3$	587	1850±40	990±20 (0.76); 6200±200 (0.32)
$^5D_0 \rightarrow ^7F_4$	696	6780±50	-

Features of the blue curves are different from those occurring in other curves. In the blue transitions, all three blue time-dependencies are linear if plotted on a natural logarithmic scale. This means that the blue transitions are fully described by a mono-exponential decay. In addition, they have an around half millisecond delay to reach their intensity maxima after electronic excitations. Meanwhile, all other transitions reach their intensity maxima right after the excitation pulse and their decays are well-fitted by a bi-exponential function because of the non-linear time-dependencies on a natural logarithmic scale. There are two possibilities to explain the maximal intensity delay of the group of blue curves. One is that the excitation energy is higher than all of the  $^5D_2$ ,  $^5D_1$ , and  $^5D_0$  emitting levels, so that at most of the excitation energies promote electrons from the ground state to the  $^5D_2$  emitting state. The emitting state requires that the closest amount of energy provided by the excitation light is present. There may be non-radiative vibrational relaxations and relaxations to the  $^5D_1$  or  $^5D_0$  emitting levels. However, half a millisecond ( $0.5 \times 10^{-3}$  s) is much longer than the time that is needed for a non-radiative process ( $10^{-12}$ - $10^{-10}$  s),<sup>31</sup> so that a more plausible explanation should exist. The typical transition times for absorptions is only about  $10^{-15}$  s, so that it is reasonable to assume that most of the delay time is consumed by other processes following the photon absorption. This means that either energy conversion or photon emission consumes most of the time due to excited state lifetimes. However, even energy transfer among different ions needs only about  $10^{-6}$  seconds, so that it is straightforward to believe that the delay time of the occurrence of fluorescence is consumed by the emission step. A phosphorescence emission usually takes  $10^{-2}$  to  $10^2$  seconds which is beyond the 0.5 milliseconds delay. Therefore, it is supposed that the delay of the intensity maxima is caused by a different emission process which is called delayed fluorescence (see Chapter 2.2.2). It has a characteristic fluorescence emission spectrum and its lifetime is only a bit shorter than that of phosphorescence emissions.<sup>117</sup>

In addition, according to Chen et al.,<sup>113</sup> decay curves that are described by bi-exponential functions are due to inhomogeneous environments caused by surface imperfections, as discussed above. Evidently, it can be stated that relaxations from the  $^5D_2$  level are influenced by surface imperfections similar to the work of Chen et al.. The short relaxation times in the  $^5D_2$  transitions represent surface imperfection-influenced

Eu fluorescence emissions. Transitions from the other emitting levels seem to be less affected by the surface imperfections because the short relaxation times are not able to be extracted by fitting these decay curves with a tri-exponential function.

When the same sample is excited by light in the IR regime, i.e. at 976 nm, the luminescence behavior is different from the above findings. A series of luminescence spectra in different time intervals after pulsed excitations at 976 nm are recorded in the visible regime. It is no longer that Eu plays a major role in the emission spectra; instead, emissions of Er dominate the emission spectra. Figure 4.3.7 shows the upconversion behavior of Er (0.002%)-, Eu (2%)-, and Yb (18%)-doped NaGd(80%)F<sub>4</sub> nanoparticles.

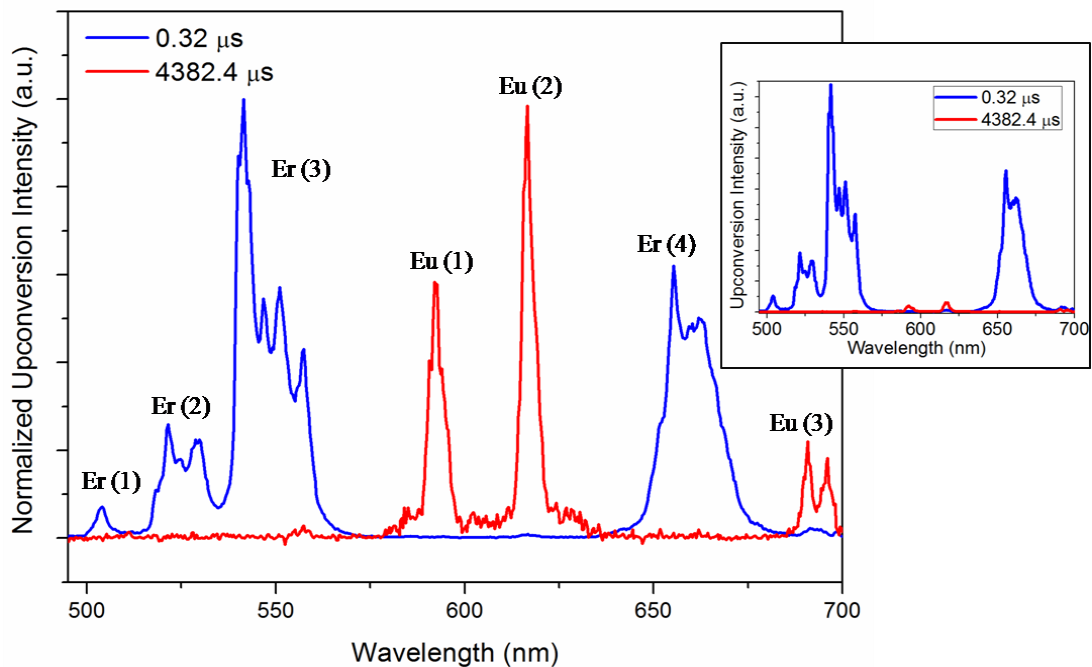


Figure 4.3.7: Normalized upconversion spectra of Er-, Eu-, and Yb-doped NaGdF<sub>4</sub> nanoparticles. The sample was excited at 976 nm and the spectra were recorded at 0.32  $\mu$ s (red) and 4382.4  $\mu$ s (blue) after the excitation pulse. The inset shows relative intensities of spectra recorded at different time points as indicated.

The short explanation of upconversion is that an atom absorbs more than one photon with lower energy; the electrons of the atom are able to be excited from their excited state when the atom absorbs another photon; the atom emits one photon with higher

energy when the double excited electron relax to the ground state. The detailed explanation of the upconversion process is given in Chapter 2.2.2. According to the energy diagram shown in Figure 4.3.25, Er and Yb ions have the potential to absorb the excitation light, and Yb ions can be excited to its  $^2F_{5/2}$  level, whereas Er can only be excited to its  $^4I_{11/2}$  level. However, it is found that only Eu and Er ions have emissions in the visible regime after several energy transfer steps, since the Yb emission occur in the IR regime and Gd in the UV regime. It can be seen in Figure 4.3.7 that only Er transitions exist when the emission spectrum was recorded at 0.32  $\mu\text{s}$  after the excitation pulse, whereas only Eu transitions are observed when the spectrum was recorded at 4382.4  $\mu\text{s}$  after the excitation pulse. In addition, Eu emissions account only for  $1.95 \pm 0.00\%$  of the total intensity when the integration of Er emissions is assumed to be 100% intensity (Figure 4.3.7 inset). This confirms that Er emissions play the major role in the emission spectra when the excitation light is in the IR regime. Note the following notation in Figure 4.3.7: Er (1):  $^2G_{11/2} \rightarrow ^4I_{11/2}$ , Er (2):  $^2H_{11/2} \rightarrow ^4I_{15/2}$ , Er (3):  $^2S_{3/2} \rightarrow ^4I_{15/2}$ , and Er (4):  $^4F_{9/2} \rightarrow ^4I_{15/2}$  transitions; Eu (1):  $^5D_0 \rightarrow ^7F_1$ , Eu (2):  $^5D_0 \rightarrow ^7F_2$ , and Eu (3):  $^5D_0 \rightarrow ^7F_4$  transitions.<sup>118,119</sup>

Upconversion decay curves shown in Figure 4.3.8 indicate that Er transitions reach their intensity maxima within 20  $\mu\text{s}$  after the excitation pulse, whereas Eu reach their intensity maxima in 0.5 milliseconds after the pulsed excitation. The temporal shifts in intensity maxima of Eu are of the same order of magnitude as it has been found in the fluorescence spectrum shown in Figure 4.3.6. It is also evident that Eu transitions have a significantly longer lifetime than Er emissions. The accurate lifetimes of Er are shown in Table 4.3.4. It is possible to assume that the excitation light is firstly absorbed by Yb ions, secondly the energy is transferred to Er ions, and finally, some of the energy is transferred from the Er ions to the Eu ions. A similar discussion was given before on Er-, Eu-, and Yb-doped NaYF<sub>4</sub> nanoparticles.<sup>118</sup>

In conclusion, fluorescence spectra of Er (0.002%)-, Eu (2%)-, and Yb (18%)-doped NaGd(80%)F<sub>4</sub> nanoparticles shows only Eu emissions by using excitation pulses at 393 nm, whereas no Er emissions occur, even at favorable excitation conditions for exciting Er ions at 377 nm. This implies that only Eu plays a role in the fluorescence spectra

when the sample is excited in the UV regime. In addition, frequently applied Eu emissions of  $^5D_0$  have extremely long lifetimes reaching up to 6.5 ms, which is due to delayed fluorescence. When the same sample is excited in the IR regime at 976 nm, Er emissions dominate the emission spectrum at first, whereas Eu emissions dominate the emission spectra after Er ions were fully deactivated. The emissions of two ions can be fully separated by time. However, although Eu ions have much longer lifetimes, intensities of their transitions are too weak to be comparable with Er emissions, which also have lifetimes around 0.1 ms (Table 4.3.4). Furthermore, when excitation pulses of different wavelength are applied, pure emissions from different ions can be observed, and their lifetimes are much longer than is observed for conventional fluorescence probes which are always in the range of nanoseconds.<sup>120</sup>

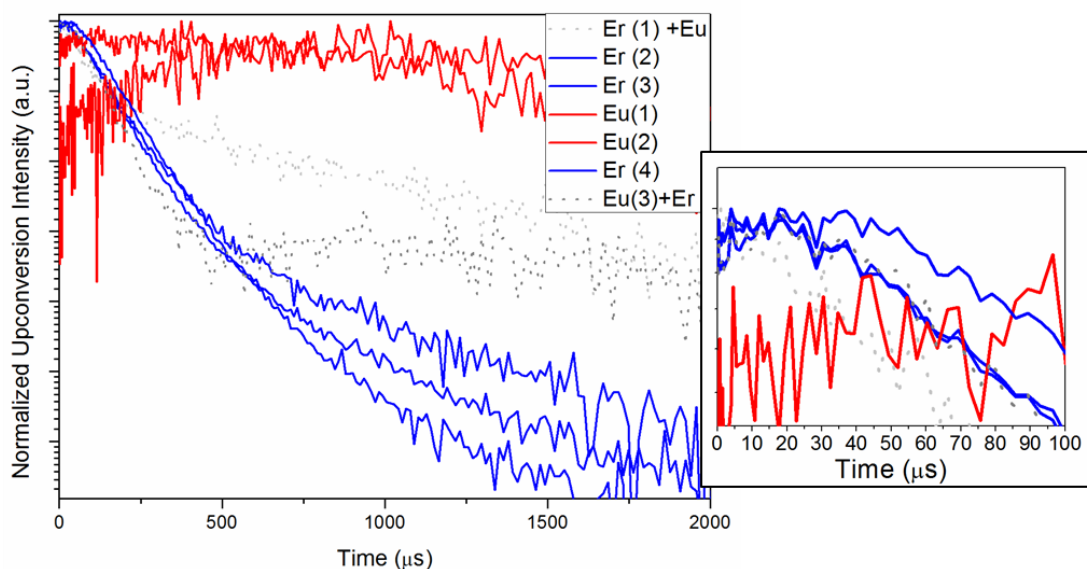


Figure 4.3.8: Normalized upconversion decay curves in a natural logarithmic scale of Er (0.002%)-, Eu (2%)-, and Yb (18%)-doped NaGd(80%)F<sub>4</sub> nanoparticles at different Eu and Er transitions. The blue curves represent relaxation behavior of pure Er transitions, red ones represent Eu transitions, and gray dots are transition mixtures with weak upconversion. The inset shows the enlarged initial spectra of Er transitions.

Table 4.3.4: Upconversion lifetimes of Er (0.002%)-, Eu (2%)-, and Yb (18%)-doped NaGd(80%)F<sub>4</sub> nanoparticles at different Er and Eu transitions. The adjusted R<sup>2</sup> values in all fits are larger than 0.98. The full decay curves of Eu emissions are beyond the experimental range. Therefore, the Eu lifetimes are estimated using the assumption that there is no upconversion signal after 8000 μs.

Transition	Peak range (nm)	Lifetime (μs)
<sup>4</sup> G <sub>11/2</sub> → <sup>4</sup> I <sub>11/2</sub>	495-509	152±4
<sup>2</sup> H <sub>11/2</sub> → <sup>4</sup> I <sub>15/2</sub>	509-534	156±2
<sup>2</sup> S <sub>3/2</sub> → <sup>4</sup> I <sub>15/2</sub>	534-576	149±2
<sup>4</sup> F <sub>9/2</sub> → <sup>4</sup> I <sub>15/2</sub>	632-685	113±2
<sup>5</sup> D <sub>0</sub> → <sup>7</sup> F <sub>1</sub>	576-602	1100±200
<sup>5</sup> D <sub>0</sub> → <sup>7</sup> F <sub>2</sub>	602-632	1100±200

### 4.3.3 Variation of Dopants

Four different samples have been prepared in order to rationalize the effect of the dopants Eu and Er on the properties of Er-, Eu-, and Yb-doped NaGdF<sub>4</sub> nanoparticles. The following Er/Eu ratios have been prepared: **Er/Eu**  $\approx$  **0** (Er (0.002%)-, Eu (5%)-, and Yb (18%)-doped NaGd(77%)F<sub>4</sub>), **Er/Eu** = **1/8** (Er (1%)-, Eu (8%)-, and Yb (11%)-doped NaGd(80%)F<sub>4</sub>), **Er/Eu** = **1/4** (Er (2%)-, Eu (8%)-, and Yb (10%)-doped NaGd(80%)F<sub>4</sub>), and **Er/Eu** =  $\infty$  (Er (5%)-, and Yb (15%)-doped NaGd(80%)F<sub>4</sub>) nanoparticles. The TEM images of all four samples with similar particle size ranging between 12-17 nm are shown in Figure 4.3.9.

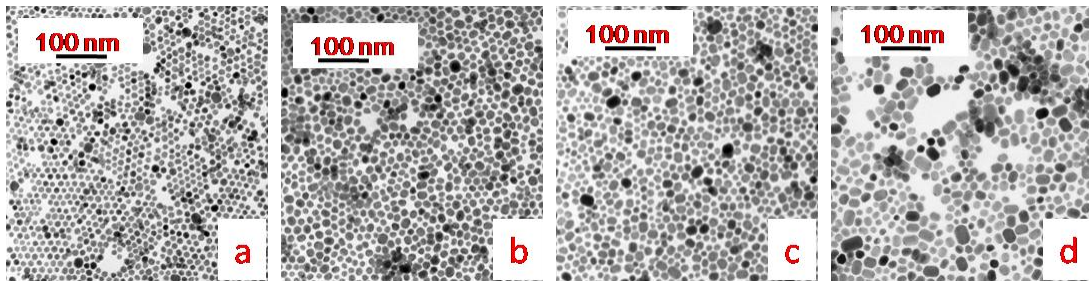


Figure 4.3.9: NaGdF<sub>4</sub>: Yb, Er, and Eu nanoparticles. TEM images of (a) Er/Eu  $\approx$  0 (12 $\pm$ 2 nm) (Er (0.002%)-, Eu (5%)-, and Yb (18%)-doped NaGd(77%)F<sub>4</sub>), (b) Er/Eu = 1/8 (15 $\pm$ 3 nm) (Er (1%)-, Eu (8%)-, and Yb (11%)-doped NaGd(80%)F<sub>4</sub>), (c) Er/Eu = 1/4 (15 $\pm$ 4 nm) (Er (2%)-, Eu (8%)-, and Yb (10%)-doped NaGd(80%)F<sub>4</sub>), and (d) Er/Eu =  $\infty$  (17 $\pm$ 5 nm) (Er (5%)-, and Yb (15%)-doped NaGd(80%)F<sub>4</sub>) nanoparticles.

All particles were prepared by exactly the same procedures, same temperature, and same heating time. Only the ratios of the lanthanide starting materials were varied (Chapter 3.2.1). All samples were prepared and characterized by the approach that was described in Chapter 4.3.2. Therefore, they can be compared with the Er (0.002%)-, Eu (2%)-, and Yb (18%)-doped NaGd(80%)F<sub>4</sub> nanoparticles discussed in Chapter 4.3.2.

As proved in Chapter 4.3.2, it is also found in Figure 4.3.10 that Er emissions dominate the upconversion spectra. Although the Eu content is in these samples higher than the Er

contents, only Er emissions can be observed, especially within short time periods after the excitation pulse (100  $\mu$ s).

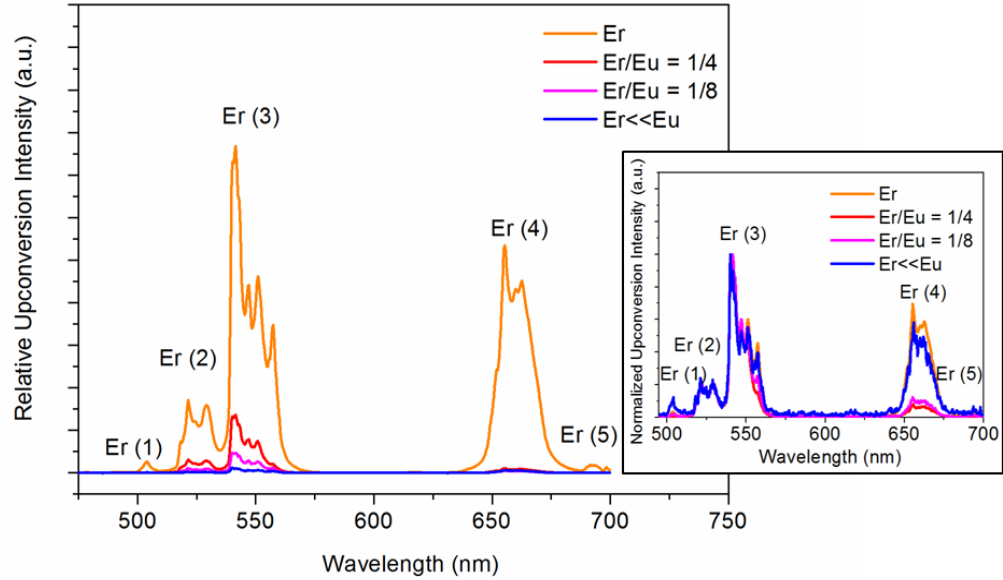


Figure 4.3.10: Relative upconversion spectra of  $Er/Eu = \infty$  (orange line, pure Er),  $Er/Eu = 1/4$  (red line),  $Er/Eu = 1/8$  (pink line), and  $Er/Eu \approx 0$  (blue line). The samples were excited at 976 nm. The inset shows upconversion spectra normalized to their intensity maxima. The labels correspond to transitions of Er. Er (1):  ${}^2G_{11/2} \rightarrow {}^4I_{11/2}$ , Er (2):  ${}^2H_{11/2} \rightarrow {}^4I_{15/2}$ , Er (3):  ${}^2S_{3/2} \rightarrow {}^4I_{15/2}$ , Er (4):  ${}^4F_{9/2} \rightarrow {}^4I_{15/2}$ , and Er (5):  ${}^2G_{9/2} \rightarrow {}^4I_{11/2}$ .

According to Figure 4.3.10 and Table 4.3.5, there are two explanations for these results. Firstly, upconversion signals increase as the Er content is increased. This is intuitive and was experimentally proved by Wang et al.,<sup>121</sup> showing that upconversion signals of Er emissions were enhanced as the Er content in  $NaY(18\%)F_4:Yb(2\%)$  particles was increased from 0.2% to 1.5%. The spectra also show that the addition of Eu does not influence the behavior of Er emission intensities as the Er content is varied. Secondly, values in the last column of Table 4.3.5 are associated with the ratios of  $(Yb + Eu)$  and  $(Er + Eu)$ . Bai et al.<sup>122,123</sup> have proved that the red-to-green ratio was increased when the Yb-to-Er ratio was increased. The explanation is that the increasing Yb concentration reduces the distance between Er and Yb ions and this enhances the energy back transfer process (EBT) which suppresses the emissions from the green band and promotes red

band emissions. Therefore, this explanation is applied for the present samples. Dwivedi et al.,<sup>124</sup> and Sheng et al.,<sup>125</sup> have demonstrated that the addition of Eu in Er- and Yb-contained substances have a higher red-to-green ratio as the Eu concentration was increased. In addition, the similar energy levels between Eu <sup>5</sup>D<sub>1-2</sub> and Er <sup>2</sup>H<sub>11/2</sub> as well as <sup>4</sup>S<sub>3/2</sub> might decrease the probability of Er green emissions. Therefore, it is supposed that the (Yb + Eu)-to-(Er + Eu) ratio also related to the red-to-green ratio. This is confirmed by the present results: the higher the (Yb + Eu)-to-(Er + Eu) ratio, the higher is the red-to-green ratio.

Table 4.3.5: Peak intensities of the spectra shown in Figure 4.3.10. Note that the green band is in the range of 500-590 nm and it includes Er (1), Er (2), and Er (3), whereas the red band is in the range of 630-700 nm and it includes Er (4) and Er (5). All intensities shown in the columns green band, red band, and green + red bands are normalized to the corresponding intensity of the sample Er/Eu = ∞. The (Yb + Eu)-to-(Er + Eu) ratio corresponds to the elemental molar ratio and the red-to-green ratios are intensity ratios calculated based on the integrations over corresponding transition peaks in the upconversion spectra.

	Green Band	Red Band	(Green + Red) Bands	(Yb + Eu)/(Er + Eu) molar ratio	Red /Green ratio
Er/Eu = ∞	100%	100%	100%	4.6	0.7
Er/Eu = 1/4	16%	2%	10%	2.1	0.1
Er/Eu = 1/8	6%	1%	4%	1.0	0.1
Er/Eu ≈ 0	2%	1%	1%	3.0	0.6

Upconversion decay curves and extracted lifetimes are shown in Figure 4.3.11 and Table 4.3.6 for each transition and all four differently doped samples. Er (2) and Er (3) transitions, in the green band, show the same temporal evolution and the same relaxation times in all four samples. Er (5) transitions are also similar as the Er (2) and Er (3) transitions. Er (1) transitions have the shortest decay times in all samples. Er (4) transitions, in the red band, have the longest relaxation time when the Er-to-Eu ratios exceeds 1/4, and have slightly shorter decay times than Er (2), Er (3), and Er (5) transitions when the Er/Eu ratio is reduced to ≤1/8. Furthermore, it is found that both the Er (1) and the Er (5) transitions shown in Figure 4.3.10 are absent in the most

commonly applied upconversion materials containing Er- and Yb-doped NaYF<sub>4</sub> nanoparticles.<sup>121</sup> It is believed that these two transitions are caused by Eu and Er interactions, since they were also found in Eu-contained Er- and Yb-doped NaYF<sub>4</sub> nanoparticles.<sup>118</sup> Suyver et al.<sup>126</sup> have reported that Er (2%)- and Yb (18%)-doped NaYF<sub>4</sub> show at 300 K at the Er (3) transitions with a lifetime of 140  $\mu$ s and the Er (4) transition shows a lifetime of 470  $\mu$ s. According to data published by Suyver et al., the upconversion material under study, Er-, Eu-, and Yb doped NaGdF<sub>4</sub>, have similar Er lifetimes, i.e. hundreds microseconds, as the well investigated material Er- and Yb-doped NaYF<sub>4</sub>. In addition, it is concluded from Table 4.3.6 that the lifetime of the red band can be elongated by increasing the Er-to-Eu ratio in the presence of Eu, which is possibly due to the elimination of non-radiative process and the enhanced energy back transfer.

In conclusion, when changing the Er-to-Eu ratio in Er-, Eu-, and Yb-doped NaGdF<sub>4</sub> particles, it is found that upconversion emission intensities increase when the Er content is increased and the Er-to-Eu ratio does not influence this property. In comparison to well-studied upconversion Er (2%)- and Yb (18%)-doped NaYF<sub>4</sub> nanoparticles, the red-to-green ratio of Er- and Yb-doped NaYF<sub>4</sub> nanoparticles increases as the Yb-to-Er ratio is increased,<sup>122</sup> whereas the red-to-green ratio of the present sample Er-, Eu-, and Yb-doped NaGdF<sub>4</sub> particles is related to the (Yb + Eu)-to-(Er + Eu) ratio. In addition, the material under study shows more Er transitions than the frequently studied Er (2%)- and Yb (18%)-doped NaYF<sub>4</sub> nanoparticles because of the existence of Eu ions. Lifetimes of this material can be altered by different Er-to-Eu ratios. It is found that the lifetime of the red band can be prolonged by increasing Er-to-Eu ratio. To separate the Er from Eu emissions thoroughly, a sample with Er/Eu  $\approx$  0 is chosen as a material for further investigations on size and annealing effects. In addition, it should also be emphasized that less than 0.1% of Er can produce clear upconversion. This is because most excitation energies absorbed by Yb ions are efficiently transferred to Er ions due to its energy level is closer to the doubled energy of the Yb transition than that of Eu ions. (Figure 4.3.25, Figure 4.3.7, inset and Figure 4.3.10).

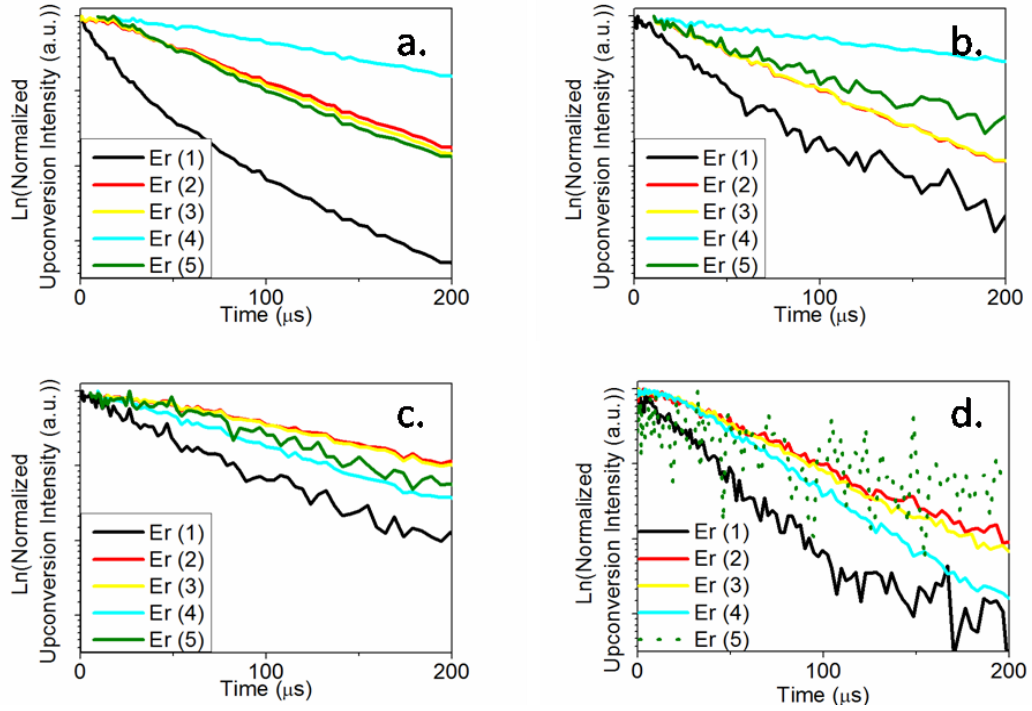


Figure 4.3.11: Normalized upconversion decay curves in natural logarithmic scale of (a)  $Er/Eu = \infty$ , (b)  $Er/Eu = 1/4$ , (c)  $Er/Eu = 1/8$ , and (d)  $Er/Eu \approx 0$ . Note that the scales are in all four Figures identical.

Table 4.3.6: Upconversion lifetimes of  $Er/Eu = \infty$ ,  $Er/Eu = 1/4$ ,  $Er/Eu = 1/8$ , and  $Er/Eu \approx 0$ . Note:  ${}^2G_{11/2} \rightarrow {}^4I_{11/2} = Er (1)$ ,  ${}^2H_{11/2} \rightarrow {}^4I_{15/2} = Er (2)$ ,  ${}^2S_{3/2} \rightarrow {}^4I_{15/2} = Er (3)$ ,  ${}^4F_{9/2} \rightarrow {}^4I_{15/2} = Er (4)$ , and  ${}^2G_{9/2} \rightarrow {}^4I_{11/2} = Er (5)$ .

Transition	Peak range (nm)	$Er/Eu = \infty$ Lifetime ( $\mu s$ )	$Er/Eu = 1/4$ Lifetime ( $\mu s$ )	$Er/Eu = 1/8$ Lifetime ( $\mu s$ )	$Er/Eu \approx 0$ Lifetime ( $\mu s$ )
${}^4G_{11/2} \rightarrow {}^4I_{11/2}$	497-510	$37.4 \pm 5$	$57.2 \pm 0.7$	$91 \pm 1$	$44.5 \pm 0.7$
${}^2H_{11/2} \rightarrow {}^4I_{15/2}$	510-535	$116.7 \pm 0.7$	$97.2 \pm 0.7$	$200 \pm 1$	$97.1 \pm 0.9$
${}^2S_{3/2} \rightarrow {}^4I_{15/2}$	535-579	$111.1 \pm 0.8$	$97.8 \pm 0.6$	$194 \pm 1$	$92.0 \pm 0.9$
${}^4F_{9/2} \rightarrow {}^4I_{15/2}$	636-685	$239 \pm 1$	$403 \pm 4$	$134.2 \pm 0.8$	$71.0 \pm 0.6$
${}^2G_{9/2} \rightarrow {}^4I_{11/2}$	685-702	$93.9 \pm 0.7$	$124 \pm 4$	$137 \pm 3$	Not measurable

#### 4.3.4 Size Effects

The large surface-to-volume ratio make nanocrystals special compared to bulk materials. It is assumed that when the particles size becomes smaller, there are more surface defects relative to the bulk because of their large surface-to-volume ratios compared to large particles. It has been mentioned in Chapter 4.3.2 that surface imperfections have an influence on the energy transfer mechanism of fluorescence emission processes of Eu ions. Therefore, size effects on the fluorescence and upconversion behavior are studied in this Chapter. Unlike Lui et al.<sup>127</sup> who have varied the particle size by using different ratios of the rare earth components and bases during syntheses, two different samples have been prepared by the same conditions except for the duration of heating during the particle growth. The large particles sample ( $19\pm 4$  nm) was heated for 2 h, and the small particles sample ( $12\pm 2$  nm) was heated for 1.5 h. TEM images of these two samples are shown in Figure 4.3.12.

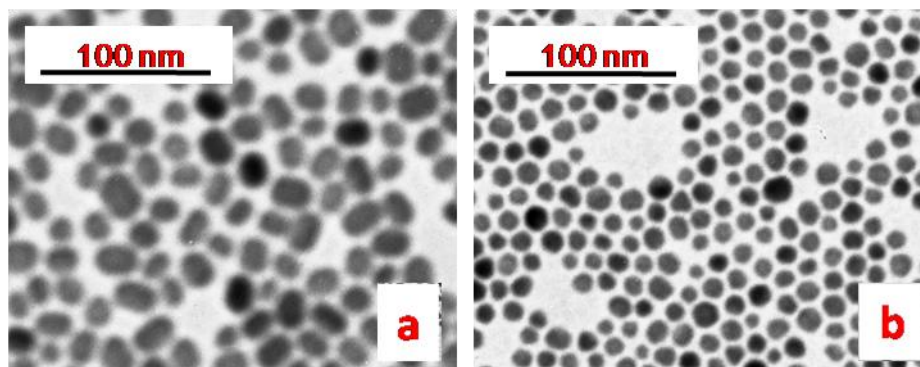


Figure 4.3.12: TEM images of (a) large, average size:  $19\pm 4$  nm, and (b) small, average size:  $12\pm 2$  nm, Er (0.002%)-, Eu (2%)-, and Yb (18%)-doped  $\text{NaGd}(80\%)\text{F}_4$  nanoparticles.

The relative fluorescence spectra of these two samples are shown in Figure 4.3.13. It can be seen in this Figure that both spectra show the same Eu emissions which are already assigned in Chapter 4.3.2. The most obvious difference between the large particles spectrum and the small particles spectrum is a change in the fluorescence intensity.

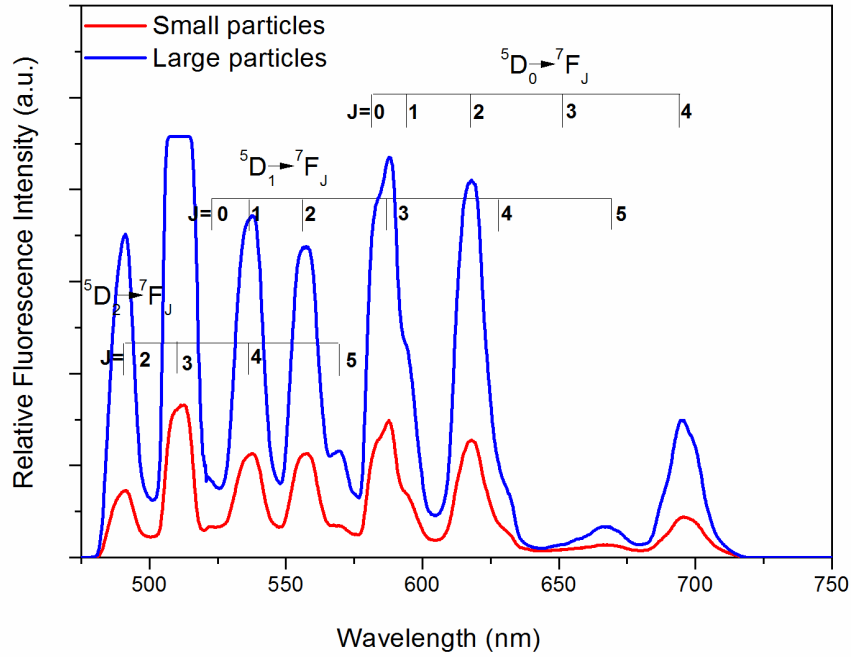


Figure 4.3.13: Eu transitions in the fluorescence spectra of small (red line) and large (blue line) Er (0.002%)-, Eu (2%)-, and Yb (18%)-doped NaGd(80%)F<sub>4</sub> nanoparticles. The samples were excited at 394 nm.

The original emission spectra obtained from the same experimental conditions were integrated separately. The small particles sample reached only 31.6% of the fluorescence intensity of the large particles sample. According to Lambert-Beer's law, the absorbance of the samples is proportional to the concentration of the fluorophores. In this case the Eu concentrations were identical. In addition, the luminescence intensity should be proportional to the fluorescence efficiency when the same number of photons is absorbed. According to the neutron activation analysis result, the small particles sample has an Eu concentration ((Eu/rare-earths)%) of  $2.07 \pm 0.07\%$ , whereas the large particles sample has an Eu concentration of  $2.20 \pm 0.05\%$ . Note that the error propagations are taken into account for determining the error limits. The Eu concentrations in these samples are in the same range, but the fluorescence intensity of the large particles is three times stronger than that of the small particles. It is supposed that this is related to the different surface-to-volume ratios of the samples under study. It is assumed that the surface defect density is the same for both of the small and large samples because of the same reaction conditions. Therefore, the larger surface-to-

volume ratio implies to more proportions of Eu ions are surface imperfection-influenced in the small particles sample compared to the sample containing large particles. More surface imperfection-induced non-radiative recombination occurs, and hence the fluorescence efficiency of the small particles sample is decreased.

The fluorescence decay curves of different transitions of both samples are shown in Figure 4.3.14 (the small particles sample) and Figure 4.3.15 (the large particles sample).

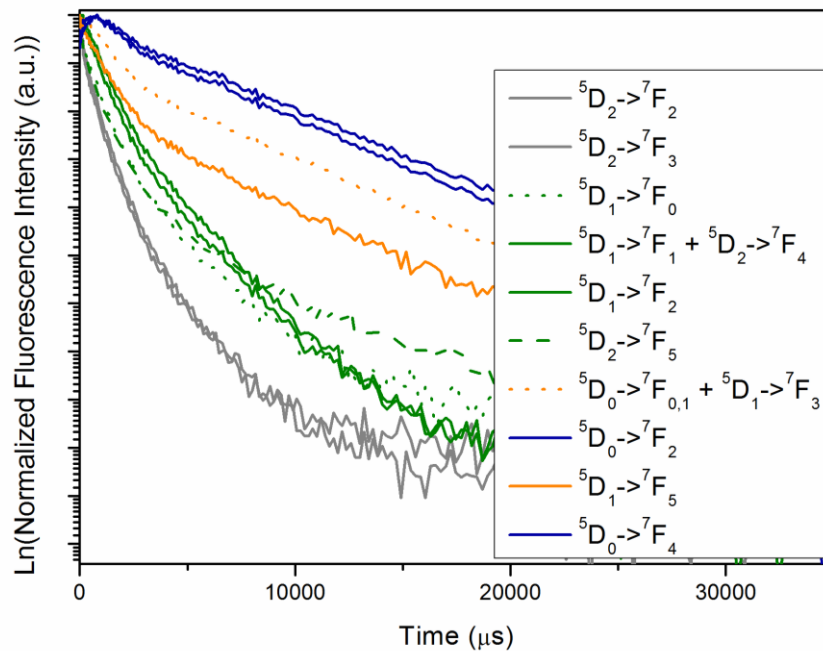


Figure 4.3.14: Normalized fluorescence decay curves in a natural logarithmic vertical scale of the small Er (0.002%)-, Eu (2%)-, and Yb (18%)-doped NaGd(80%)F<sub>4</sub> particles sample for different Eu transitions. All transitions shown in this Figure are found in the red fluorescence spectrum shown in Figure 4.3.13.

Decay curves of both samples can be explained in a similar way as discussed in Chapter 4.3.2. However, both of the samples have different time-dependencies for the curves plotted in blue color, compared to the results shown in Figure 4.3.6. In Figure 4.3.6, the blue curves drop linearly after the intensity maxima, whereas the blue curves in the samples discussed in this Chapter show clearly curvatures after the intensity maxima.

Note that, the scales of all three Figures are the same, so that the curvatures are not amplified in Figure 4.3.14 and Figure 4.3.15.

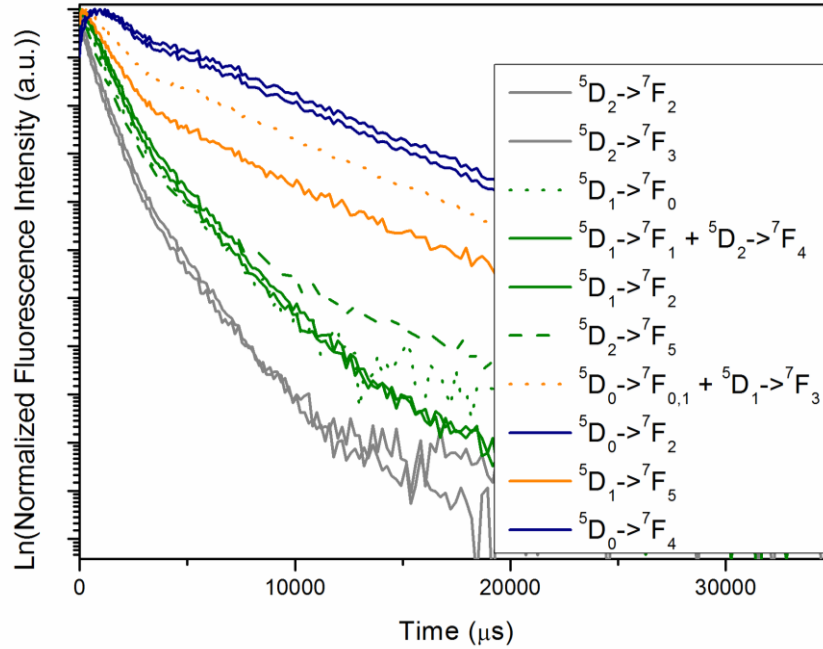


Figure 4.3.15: Normalized fluorescence decay curves in a natural logarithmic vertical scale of the large Er (0.002%)-, Eu (2%)-, and Yb (18%)-doped NaGd(80%)F<sub>4</sub> particles sample for different Eu transitions. All transitions shown in this Figure are found in the blue fluorescence spectrum shown in Figure 4.3.13.

There are three stages of these time-dependencies in both, the small and the large particles samples. An increasing stage and two distinguished decreasing stages. The two decreasing stages suggest that two different relaxation paths take place. Two different deactivation stages of the blue curves can be explained by the mixture of  $^5D_0$  and  $^5D_1$  transitions. In these samples, the energy levels of Eu have slightly changed compared to those in the sample discussed in Chapter 4.3.2. The  $^5D_1$  transition releases photons of similar energy as the  $^5D_0$  transitions in both, the small and the large particles samples. In other words, at the peak positions, both of the  $^5D_1$  and  $^5D_0$  transitions have a comparable influence on the time-dependencies. At these transitions, the standard deviations of decay times are large when they are fitted by a bi-exponential function.

Table 4.3.7: Fluorescence lifetimes of the small and large Er (0.002%)-, Eu (2%)-, and Yb (18%)-doped NaGd(80%)F<sub>4</sub> nanoparticles at different Eu transitions.

Transition	Peak <sub>maximum</sub>	Lifetime (μs) of Small Particles	Lifetime (μs) of Large Particles
<sup>5</sup> D <sub>2</sub> → <sup>7</sup> F <sub>2</sub>	491	63±3 (0.43); 580±10 (0.54)	98±3 (0.66); 764±8 (0.99)
<sup>5</sup> D <sub>2</sub> → <sup>7</sup> F <sub>3</sub>	513	96±5 (0.41); 640±10 (0.58)	133±6 (0.27); 790±10 (0.77)
<sup>5</sup> D <sub>1</sub> → <sup>7</sup> F <sub>0</sub>	522	29±2 (0.30); 780±10 (0.64)	955±6
<sup>5</sup> D <sub>1</sub> → <sup>7</sup> F <sub>1</sub> + <sup>5</sup> D <sub>2</sub> → <sup>7</sup> F <sub>4</sub>	538	885±7	1030±6
<sup>5</sup> D <sub>1</sub> → <sup>7</sup> F <sub>2</sub>	557	988±8	1108±8
<sup>5</sup> D <sub>2</sub> → <sup>7</sup> F <sub>5</sub>	569	50±3 (0.35); 760±10 (0.85)	380±40 (0.37); 1100±40 (0.66)
<sup>5</sup> D <sub>0</sub> → <sup>7</sup> F <sub>0,1</sub> + <sup>5</sup> D <sub>1</sub> → <sup>7</sup> F <sub>3</sub>	588	1350±40 (0.85); 7200±800 (0.22)	1300±40 (0.90); 6400±400 (0.34)
<sup>5</sup> D <sub>0</sub> → <sup>7</sup> F <sub>2</sub>	618	1220±90 (0.77); 5800±200 (0.67)	1600±200 (0.60); 6100±400 (0.72)
<sup>5</sup> D <sub>1</sub> → <sup>7</sup> F <sub>5</sub>	667	940±40 (0.73); 5000±800 (0.15)	1240±30 (1.00); 7000±1000 (0.11),
<sup>5</sup> D <sub>0</sub> → <sup>7</sup> F <sub>4</sub>	696	1400±200 (0.57); 6000±300 (0.77)	900±100 (0.81); 6000±20 (0.93)

Lifetimes for the excited <sup>5</sup>D<sub>0</sub>, <sup>5</sup>D<sub>1</sub>, and <sup>5</sup>D<sub>2</sub> states are assigned to be around 5000 - 7000 μs, 900 - 1200 μs, and 50 - 800 μs, respectively, as shown in Table 4.3.7. It shows that all transitions in the large particles sample show slightly longer relaxation times compared to those of small particles samples. It is known that both the fluorescence quantum yield and the relaxation times are inversely proportional to the summation of the radiative rate constant and the non-radiative rate constant,<sup>128</sup> so that the slightly longer relaxation times confirm that the large particles sample has a higher fluorescence efficiency than the small particles sample. It is assumed that less excitation energy is absorbed by Eu ions in the small particles sample and most of it is lost among defects. The longer relaxation lifetimes and the stronger fluorescence intensity indicate that the longer heating duration leads to a larger particles size and longer fluorescing Er-, Eu-,

and Yb-doped NaGd(80%)F<sub>4</sub> nanoparticles. Moreover, when taking a closer look at the maximum intensity delays of fluorescence delayed transitions, it can be found that the large particles sample takes on the average about 200 μs longer to reach its intensity maximum. This implies that it takes more time to transfer the excitation energy to fluorescence delayed transitions in large particles.

When these samples are excited by IR radiation at 976 nm, upconversion spectra occur for both of the small particles and the large particles sample, as shown in Figure 4.3.16. Both spectra show typical Er transitions as assigned in Chapter 4.3.2.

From Figure 4.3.16 it is evident that the upconversion intensities of both samples are the same and the ratio of the overall upconversion intensities between the small particles sample and the large particles sample is  $1.10 \pm 0.07$ . However, it is obvious that the green-to-red ratio is different for these two samples. The large particles sample has a stronger green band emission than the red band emission (green/red band ratio  $\sim 1.32 \pm 0.04$ ), whereas the small particles sample shows a weaker green band emission than the red band emission (green/red band ratio  $\sim 0.90 \pm 0.02$ ). According to Shan et al.,<sup>129</sup> the crystal structure of particles is able to change the ratio between the green band and red band emissions. The host crystal with a hexagonal structure increases the green-to-red band ratio, whereas the host crystal with a cubic structure shows only a small green-to-red ratio. Zhao et al.<sup>130</sup> also concluded that the green-to-red ratio depends on both, the particle size and the crystal structure in Er- and Yb-doped NaYF<sub>4</sub> nanoparticles. Particles that are smaller than 14 nm have a cubic structure and stronger red emission whereas particles in the size range between 20-45 nm show a hexagonal structure and stronger green emission. The ratio of lanthanide starting materials in both samples was fixed; only the duration of heating during the particle growth stage was varied in this study, so that the elemental composition is not an issue to vary the green-to-red ratio, as discussed in Chapter 4.3.3. Clearly it is shown that the heating duration varies the particle size. Therefore, the different green-to-red ratio shown in Figure 4.3.16 is evidently related to different particle sizes and different crystal structures.

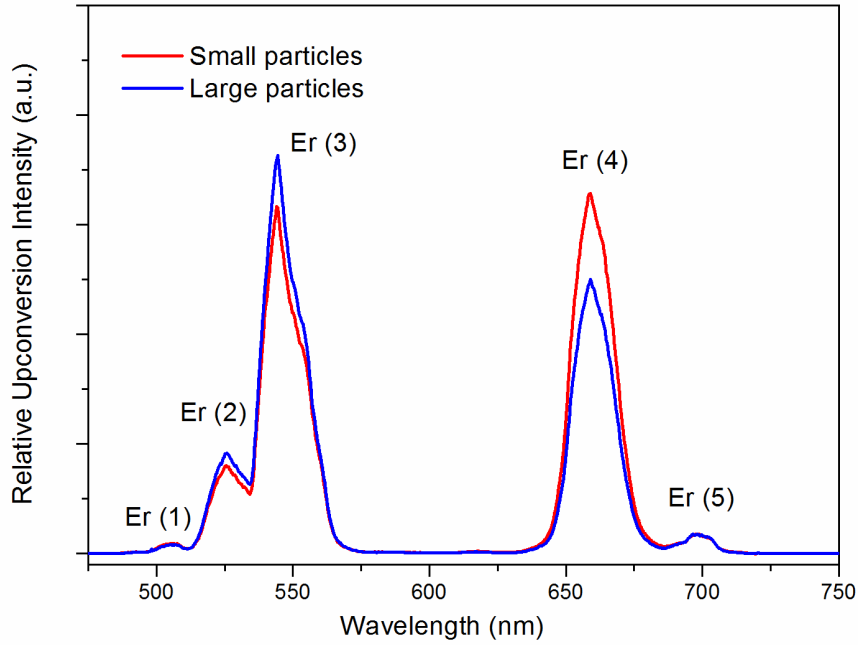


Figure 4.3.16: Relative upconversion spectra of the small (red line) and large (blue line) Er (0.002%)-, Eu (2%)-, and Yb (18%)-doped NaGd(80%)F<sub>4</sub> nanoparticles. The samples were excited at 976 nm. Note the following transitions: Er (1) =  ${}^2G_{11/2} \rightarrow {}^4I_{11/2}$ , Er (2) =  ${}^2H_{11/2} \rightarrow {}^4I_{15/2}$ , Er (3) =  ${}^2S_{3/2} \rightarrow {}^4I_{15/2}$ , Er (4) =  ${}^4F_{9/2} \rightarrow {}^4I_{15/2}$ , and Er (5) =  ${}^2G_{9/2} \rightarrow {}^4I_{11/2}$ .

Decay curves of both, the small particles sample (a) and the large particles samples (b) are presented in Figure 4.3.17. The most pronounced difference between both samples is that the small particles sample reaches its intensity maximum at 10  $\mu$ s, whereas the large particles sample reaches its intensity maximum at 30  $\mu$ s. It may be due to a larger amount of neighboring Yb ions within a large particle is able to transfer their energy to Er ions which leads to a slightly longer energy transfer time. The energy transfer mechanism for small structures in (b) between 100-200  $\mu$ s is still unknown; possibly it is due to the trace amount of the energy transferred from Eu.

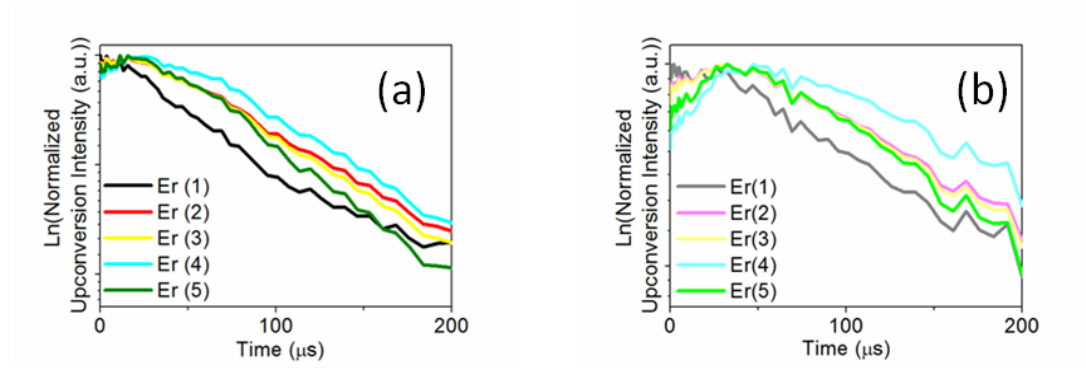


Figure 4.3.17: Normalized upconversion decay curves in a natural logarithmic vertical scale of (a) small, and (b) large Er (0.002%)-, Eu (2%)-, and Yb (18%)-doped NaGd(80%)F<sub>4</sub> nanoparticles. Note that the scales in both figures are the same.

Table 4.3.8 lists the lifetimes of both samples. It can be seen that the lifetimes of the large particles sample are always almost twice longer than the lifetimes of the small particles sample. It has been stated earlier that both luminescence intensity and lifetimes should be related to the summation of radiative and non-radiative rate constants, but in this case, the lifetimes have been extended by increasing the particle size, whereas upconversion intensities were found not be significantly changed (see Figure 4.3.16). This is because that these two spectra were recorded at a short time after the excitation pulse. At this time, the large particles sample has not reached its intensity maximum, instead it is still increasing. Therefore, no difference in upconversion intensity is observed for both samples under these measurement conditions.

Table 4.3.8 Upconversion lifetimes of the small and the large Er (0.002%)-, Eu (2%)-, and Yb (18%)-doped NaGd(80%)F<sub>4</sub> nanoparticles. All transitions in both samples are well fitted by mono-exponential functions ( $R^2 \geq 0.98$ ). The transitions are labeled as follows:  ${}^2G_{11/2} \rightarrow {}^4I_{11/2} = \text{Er (1)}$ ,  ${}^2H_{11/2} \rightarrow {}^4I_{15/2} = \text{Er (2)}$ ,  ${}^2S_{3/2} \rightarrow {}^4I_{15/2} = \text{Er (3)}$ ,  ${}^4F_{9/2} \rightarrow {}^4I_{15/2} = \text{Er (4)}$ , and  ${}^2G_{9/2} \rightarrow {}^4I_{11/2} = \text{Er (5)}$ .

Transition	Peak range (nm)	Small particles	Large particles
${}^4G_{11/2} \rightarrow {}^4I_{11/2}$	488-512	102±2	220±4
${}^2H_{11/2} \rightarrow {}^4I_{15/2}$	512-534	116±1	194±1
${}^2S_{3/2} \rightarrow {}^4I_{15/2}$	534-575	110±1	184±1
${}^4F_{9/2} \rightarrow {}^4I_{15/2}$	631-686	120±1	202±3
${}^2G_{9/2} \rightarrow {}^4I_{11/2}$	686-716	90±2	154±3

In summary, size effects of Eu emission spectra have been investigated. Size variations change the surface-to-volume ratio of the nanoparticles, which reduces the proportion of surface defect-influenced Eu ions in the large particles sample, and hence leads to enhanced fluorescence efficiency. Furthermore, longer lifetimes are obtained from increasing the particle size. In addition, the large particles consume a longer time to reach the intensity maximum of fluorescence. Regarding upconversion properties in the Er spectra, the intensities were not varied as much as observed in the Eu fluorescence spectra due to the measurement timing, but the lifetimes of the large particles sample are  $1.8 \pm 0.2$  times longer than that of the small particles sample. Due to the different green-to-red ratio in the Er upconversion spectra and the same elemental composition obtained from the neutron activation analysis, it is concluded that the different particle sizes leads to different crystal structures. The lifetimes in both the Eu fluorescence spectra and Er upconversion spectra can be prolonged by enlarging the particles size, which is essentially due to the reduced influence of surface defect-influenced ions.

### 4.3.5 Annealing Effects

Annealing is a heating treatment that is reached by raising the system temperature to a certain value for a given period of time. During this time, structural defects are able to be eliminated. Afterwards, a higher crystal order can be found. Annealing processes on nanoparticles are frequently used by using temperatures between hundreds or thousands of Kelvin.<sup>131</sup> The nanoparticles are often aggregated after the annealing process. In this Chapter, two samples were prepared to investigate annealing effects on fluorescence and upconversion properties. The annealed particles were obtained from heating the particles at 200 °C for 70 hours. 200 °C is below the particles formation temperature, i.e. this is a gentle heating treatment that avoids severe particle aggregation compared to annealing at more elevated temperatures. However, due to this long time period that is used for annealing, the particles size varied a bit because of coarsening effect which is also called Ostwald ripening effect.<sup>132</sup> Ostwald ripening effect grows larger particles at the expense of smaller ones and this is driven by the size-dependent solubility difference between small and large particles. TEM images of these two samples are shown in Figure 4.3.18. The unannealed sample has an average size of  $12\pm 2$  nm, whereas the annealed sample shows a broader size range of  $16\pm 4$  nm than the unannealed sample.

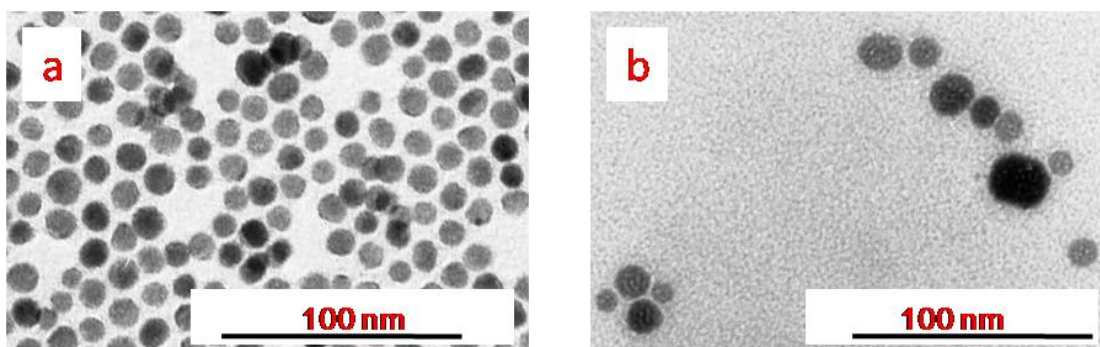


Figure 4.3.18: TEM images of (a) unannealed, average size:  $12\pm 2$  nm, and (b) annealed, average size:  $16\pm 4$  nm Er (0.002%)-, Eu (5%)-, and Yb (18%)-doped  $\text{NaGd}(77\%)\text{F}_4$  nanoparticles.

Figure 4.3.19 shows fluorescence spectra of the unannealed and the annealed samples, and both were excited by 394 nm radiation. Therefore, fluorescence efficiencies of these two spectra can be easily compared with each other. All peaks in the spectra are assigned and discussed in Chapter 4.3.2. There is almost no difference between the unannealed and annealed sample in the fluorescence spectra, including the similar emission intensities and the shape of the transitions. This implies that such an annealing process has limited influence on the Eu fluorescence efficiency of Er (0.002%)-, Eu (5%)-, and Yb (18%)-doped NaGd(77%)F<sub>4</sub> nanoparticles.

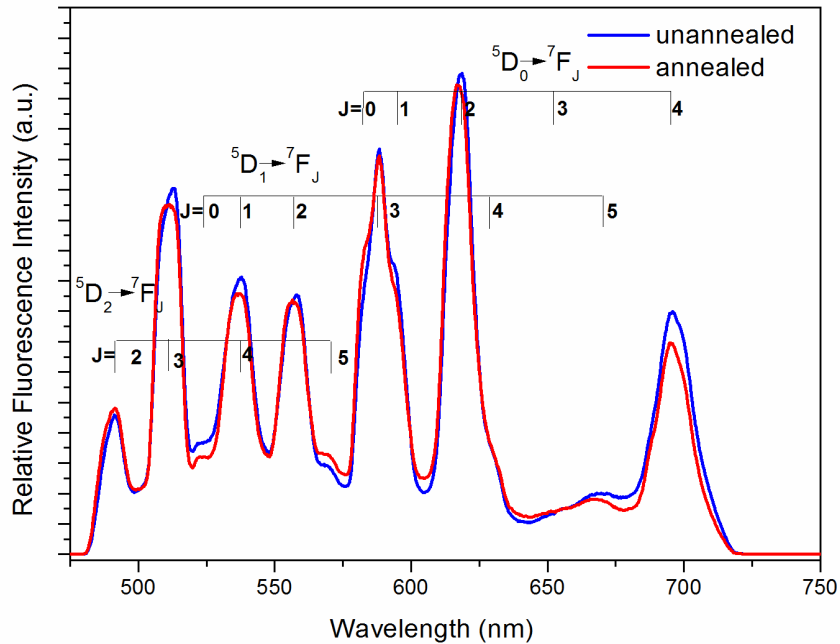


Figure 4.3.19: Eu transitions and relative fluorescence spectra of the unannealed (blue line) and annealed (red line) Er (0.002%)-, Eu (5%)-, and Yb (18%)-doped NaGd(77%)F<sub>4</sub> nanoparticles. The samples were excited at 394 nm.

Furthermore, time independent studies are shown in Figure 4.3.20 (unannealed sample) and Figure 4.3.21 (annealed sample). Relaxation times are determined from these results and are shown in Table 4.3.9. The explanations of the decay curves shown in Figures 4.3.20 and 4.3.21 are the same as discussed in Chapter 4.3.2. It is clear that no specific

difference exists, in other words, the decay curves of each transition are almost identical in both samples. The fluorescence intensity maximum starts at the same time, the decay times are the same, and ratio between short and long decay processes are the same, as well. This tells us that an annealing process at 200 °C for 70 h has no influence on the Eu fluorescence spectra. In comparison with size effects on Er-, Eu-, and Yb-doped NaGdF<sub>4</sub> nanoparticles, it can be stated that the Eu fluorescence can be enhanced more efficiently by changing the particles size rather than by an annealing process at 200 °C for 70 h.

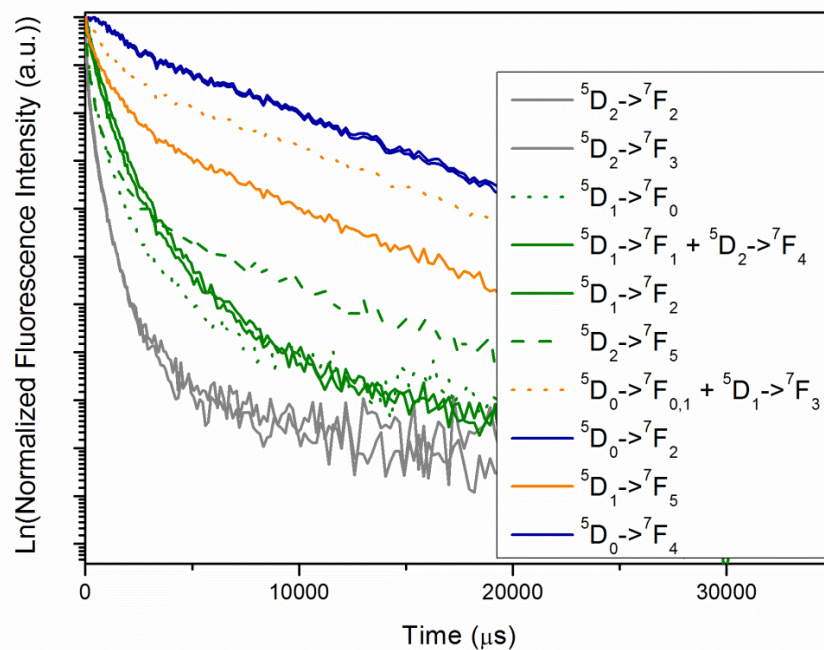


Figure 4.3.20: Normalized fluorescence decay curves in a natural logarithmic vertical scale of the unannealed Er (0.002%)-, Eu (5%)-, and Yb (18%)-doped NaGd(77%)F<sub>4</sub> nanoparticles.

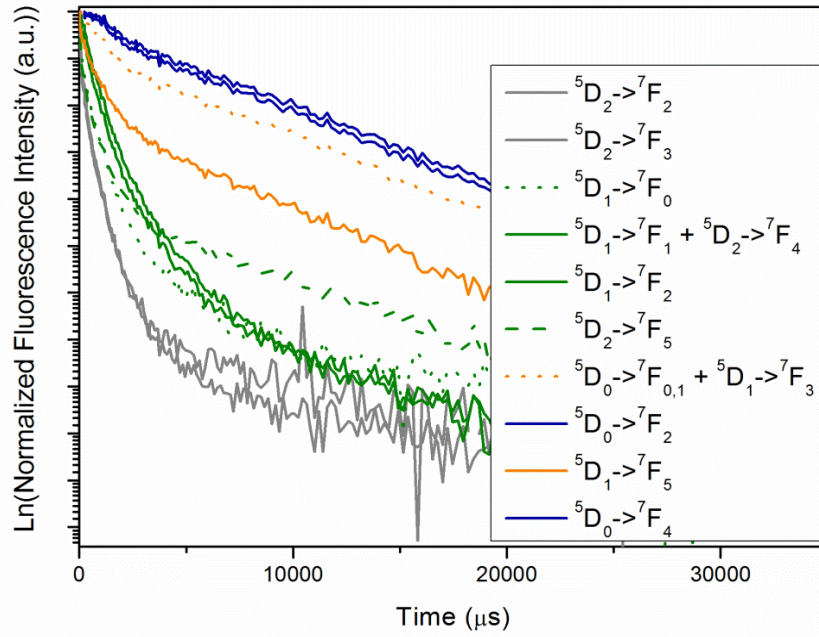


Figure 4.3.21: Normalized fluorescence decay curves in a natural logarithmic scale of the annealed Er (0.002%)-, Eu (5%)-, and Yb (18%)-doped NaGd(77%)F<sub>4</sub> nanoparticles.

Table 4.3.9: Fluorescence lifetimes of the unannealed and annealed Er (0.002%)-, Eu (5%)-, and Yb (18%)-doped NaGd(77%)F<sub>4</sub> nanoparticles at different Eu transitions. All transitions in both samples are well fitted by bi-exponential functions ( $R^2 \geq 0.99$ ).

Transition	Peak <sub>maximum</sub>	Lifetime (μs) of Unannealed Sample	Lifetime (μs) of Annealed Sample
${}^5D_2 \rightarrow {}^7F_2$	491	34.5±0.8 (0.65); 267±7 (0.35)	32±1 (0.57); 283±9 (0.38)
${}^5D_2 \rightarrow {}^7F_3$	513	40±1(0.64); 280±8 (0.38)	40±1(0.57); 310±9 (0.40)
${}^5D_1 \rightarrow {}^7F_0$	522	47±2 (0.43); 412±9 (0.54)	21±1 (0.43); 397±9 (0.51)
${}^5D_1 \rightarrow {}^7F_1 +$ ${}^5D_2 \rightarrow {}^7F_4$	538	220±20 (0.49); 790±40 (0.50)	200±20 (0.36); 670±40 (0.57)
${}^5D_1 \rightarrow {}^7F_2$	557	380±30 (0.71); 1100±100 (0.34)	410±30 (0.83); 1100±200 (0.25)
${}^5D_2 \rightarrow {}^7F_5$	569	39±1 (0.64);	29±1 (0.55);

		271±8(0.38)	450±10 (0.38)
$^5D_0 \rightarrow ^7F_{0,1}$ + $^5D_1 \rightarrow ^7F_3$	588	840±20 (0.67); 5700±100 (0.33)	920±30 (0.63); 5700±100 (0.38)
$^5D_0 \rightarrow ^7F_2$	618	1600±100 (0.50); 6000±100 (0.60)	1400±100 (0.51); 5900±100 (0.58)
$^5D_1 \rightarrow ^7F_5$	667	210±10 (0.44); 1570±60 (0.49)	47±4 (0.33); 980±30 (0.57)
$^5D_0 \rightarrow ^7F_4$	696	1200±80 (0.55); 6000±100 (0.67)	1800±200 (0.46); 6000±100 (0.63)

Annealing effects on upconversion spectra are more pronounced than fluorescence spectra. The unannealed and annealed upconversion spectra are shown in Figure 4.3.22. At first glance, there is a significant improvement of the upconversion intensity. The annealed sample shows  $63 \pm 2$  times stronger upconversion intensity than the unannealed sample. The explanation of this improvement can be confirmed by the inset of Figure 4.3.22. As already mentioned in Chapter 4.3.4, particles with cubic crystal structure show a small green-to-red ratio, whereas particles with a hexagonal crystal structure show an increased green-to-red ratio. The green-to-red ratio of the unannealed sample is  $1.57 \pm 0.04$  whereas the green-to-red ratio of the annealed sample is  $3.7 \pm 0.1$ . This implies that the annealed sample has a higher amount of hexagonal structure compared to the unannealed sample which is confirmed by XRD measurement shown in Figure 4.3.23 which shows large cubic peaks in the unannealed sample. In addition, it is known that Er ions can be upconverted in hexagonal structure more efficiently than in the cubic structure. Therefore, it is clear that, an annealing process at 200°C for 70 h on the studied material changes the crystal structure and enhances the upconversion efficiency.

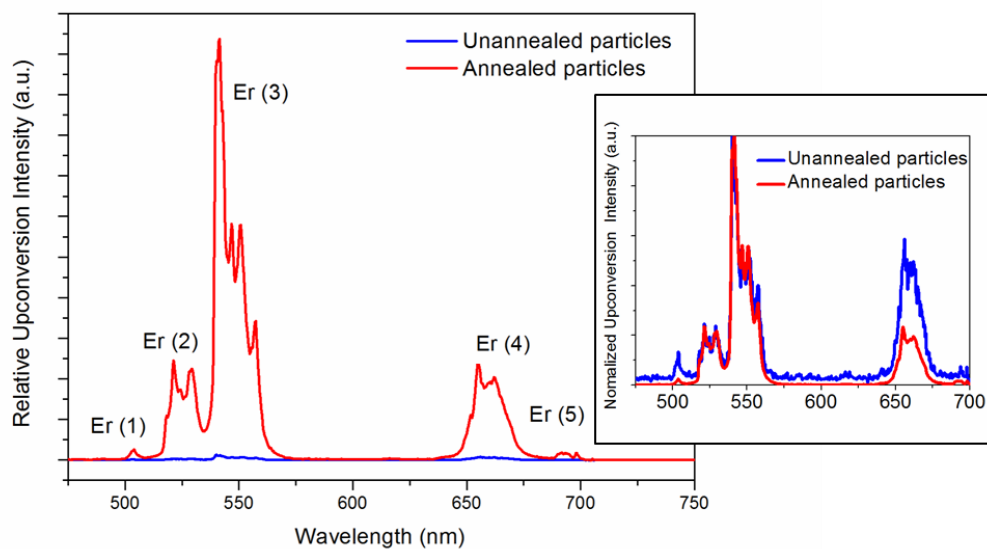


Figure 4.3.22: Relative upconversion spectra of the unannealed (blue line) and annealed (red line) Er (0.002%)-, Eu (5%)-, and Yb (18%)-doped NaGd(77%)F<sub>4</sub> nanoparticles.

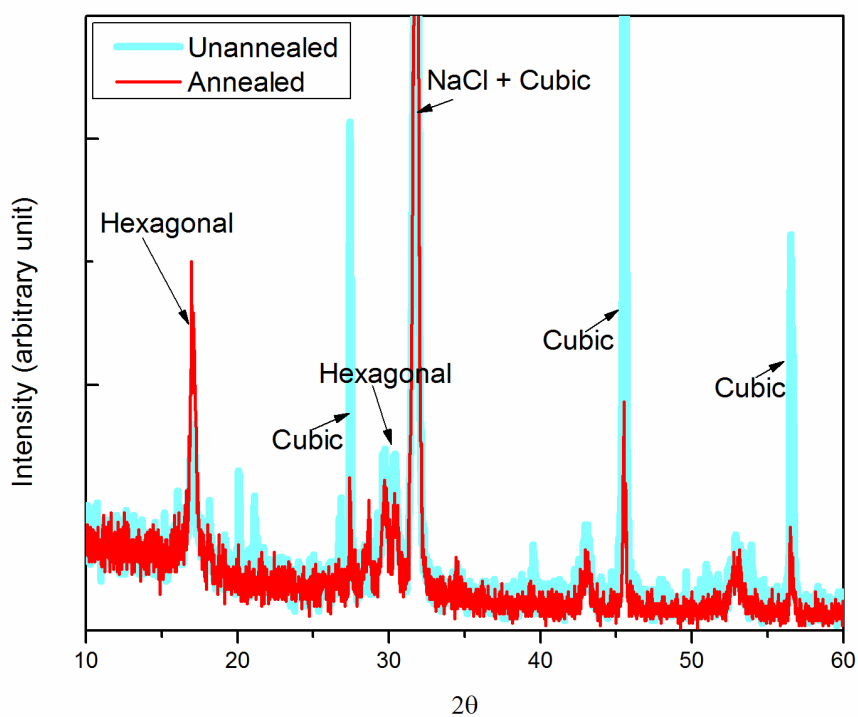


Figure 4.3.23: Powder diffraction data of the unannealed and annealed Er (0.002%)-, Eu (5%)-, and Yb (18%)-doped NaGd(77%)F<sub>4</sub> nanoparticles.

The corresponding time-dependencies of both the unannealed and annealed samples are presented in Figure 4.3.24. The lifetimes of the corresponding transitions shown in Figure 4.3.24 are summarized in Table 4.3.10. According to this, the lifetimes of the annealed sample are longer than those of the unannealed sample. Especially, the red band emission is more than 2.5 times longer than that of the unannealed sample. This implies a change in elemental composition. According to the results discussed in Chapter 4.3.3, the Er-to Eu ratio should be between 1/4 and 1/8. Unfortunately, the exact Er concentration could not be measured by NAA. However, the NAA result shows a decrease in Eu-to-Gd, Eu-to-Yb and Yb-to-Gd ratios in the annealed sample compared to the unannealed sample. The master thesis achieved in this group also showed that the dopant concentration is decreased after the annealing process.<sup>90</sup>

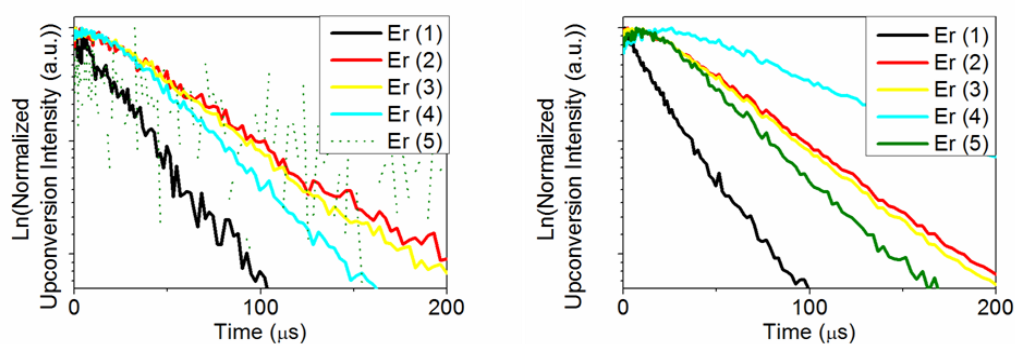


Figure 4.3.24: Normalized upconversion decay curves in a natural logarithmic scale of the unannealed (the left) and annealed (the right) Er (0.002%)-, Eu (5%)-, and Yb (18%)-doped  $\text{NaGd}(77\%)\text{F}_4$  nanoparticles. Note that vertical scales are the same in both figures.

Finally, the annealing process at 200°C for 70 h on Er (0.002%)-, Eu (5%)-, and Yb (18%)-doped  $\text{NaGd}(77\%)\text{F}_4$  nanoparticles does not change the fluorescence spectra that are Eu ion dominated when the excitation wavelength is set to 394 nm. There is no obvious change in Eu fluorescence intensity and lifetimes between the unannealed and annealed samples. However, this annealing process enhances the Er ions dominated upconversion efficiencies dramatically by a change in crystal structure.

Table 4.3.10: Upconversion lifetimes of the unannealed and annealed Er (0.002%)-, Eu (5%)-, and Yb (18%)-doped NaGd(77%)F<sub>4</sub> nanoparticles. All transitions in both samples are well fitted by mono-exponential functions ( $R^2 \geq 0.98$ ). The transitions are labeled as follows:  ${}^2G_{11/2} \rightarrow {}^4I_{11/2} = \text{Er (1)}$ ,  ${}^2H_{11/2} \rightarrow {}^4I_{15/2} = \text{Er (2)}$ ,  ${}^2S_{3/2} \rightarrow {}^4I_{15/2} = \text{Er (3)}$ ,  ${}^4F_{9/2} \rightarrow {}^4I_{15/2} = \text{Er (4)}$ , and  ${}^2G_{9/2} \rightarrow {}^4I_{11/2} = \text{Er (5)}$ .

Transition	Peak range (nm)	Unannealed Lifetime ( $\mu\text{s}$ )	Annealed Lifetime ( $\mu\text{s}$ )
${}^4G_{11/2} \rightarrow {}^4I_{11/2}$	488-512	44.5 $\pm$ 0.7	46.7 $\pm$ 0.3
${}^2H_{11/2} \rightarrow {}^4I_{15/2}$	512-534	97.1 $\pm$ 0.9	113.5 $\pm$ 0.8
${}^2S_{3/2} \rightarrow {}^4I_{15/2}$	534-575	92.0 $\pm$ 0.9	103.6 $\pm$ 0.5
${}^4F_{9/2} \rightarrow {}^4I_{15/2}$	631-686	71.0 $\pm$ 0.6	184.2 $\pm$ 0.8
${}^2G_{9/2} \rightarrow {}^4I_{11/2}$	686-716	Not measurable	81.1 $\pm$ 0.5

### 4.3.6 Conclusions

In the beginning of Chapter 4.3, it was shown that only 10% Eu-doped NaGdF<sub>4</sub> nanoparticles yield 44% of the NaEuF<sub>4</sub> nanoparticles fluorescence intensity. This is due to the fact that a higher Eu content may lead to self-quenching and hence this might also decrease the fluorescence efficiency. In addition, when Eu ions are put into NaGdF<sub>4</sub> nanoparticles, the characteristic lifetimes of Eu can be enhanced by a factor of 1.2. In other words, we can dope Eu ions onto NaGdF<sub>4</sub> hosts without a loss in fluorescence efficiency. Although the unexpected Eu emissions of the excited states <sup>5</sup>D<sub>1</sub> and <sup>5</sup>D<sub>0</sub> also appear in the emission spectra, these emissions can be filtered or entirely eliminated by optical filters or by gating the fluorescence lifetime.

Furthermore, upconversion which can absorb low-energy photons and emit high-energy photons is also introduced for the multifunction nanomaterials. Er ions and Yb ions are doped in Eu-contained NaGdF<sub>4</sub> nanoparticles. It is found that the probe has distinct luminescence properties in (0.002%)-, Eu (5%)-, and Yb (18%)-doped NaGd(77%)F<sub>4</sub> nanoparticles when different excitation wavelengths are applied. Excitation by 393 nm in the UV regime leads only to Eu emissions, where the lifetimes reaches up to 6.5 ms whereas excitation by 976 nm in the IR regime leads only to Er emissions, where the lifetimes reaches up to 0.1 ms. In addition, the Eu emission spectra show a delay of about 0.5 ms after primary electronic excitation before they reach their intensity maxima. In the case of Er emission spectra this time is shorter, so that less than 0.05 ms are required to reach the intensity maxima after excitation. The former is attributed to delayed fluorescence and the latter one is due to an energy transfer from Yb ions to Er ions.

To alter upconversion properties of the multifunction material prepared in this work, further investigations on variations of dopants, size effects, and annealing effects are studied. The dopant variation of Er/ Eu ratios shows that the red-to-green emission ratio is proportional to the (Yb + Eu)-to-(Er + Eu) ratio. This is because Eu ions are not only able to decrease the green emissions through non-radiative transitions from Er <sup>2</sup>H<sub>11/2</sub> and <sup>4</sup>S<sub>3/2</sub> to Eu <sup>5</sup>D<sub>0</sub>, but they also increase the green emissions by a non-radiative process from its <sup>5</sup>D<sub>1-2</sub> levels to the green band of Er. The increasing Er-to-Eu ratio in the

presence of Eu also increases significantly the lifetime of the dominant emission in the red band because of the enhanced energy back transfer.

For samples with the same elemental composition, a variation of particles size shows that the large particles sample with a smaller surface-to-volume ratio has enhanced fluorescence intensity compared to the small particles sample. This is attributed to the decreasing number of surface imperfections when assuming the densities of surface imperfections on both small and large particles surface are same due to the identical preparation conditions. Therefore, more excitation energy can be absorbed by Eu ions in the large particles sample. However, only slightly longer lifetimes of Eu transitions in the large particles sample implies that the surface imperfection-influenced Eu plays a minor role to alter the lifetimes of Eu transitions in the samples, perhaps due to the extremely long lifetimes of  $^5D_0$  energy state. Regarding upconversion properties in Er spectra, the intensities were not varied as much as observed in Eu fluorescence spectra, but the lifetimes of the large particles sample are  $1.8 \pm 0.2$  times longer than that of the small particles sample. In addition, the change in green-to-red ratio in upconversion spectra implies that the particles sizes have influenced on crystal structure. The lifetimes in both Eu fluorescence spectra and Er upconversion spectra can be prolonged by enlarging the particles size, which is essentially due to the reduced influence of surface defect-influenced ions.

After an annealing process, it is found that an annealing process has limited influence on the Eu emission. In other words, an annealing process at 200°C for 70 h is less efficient in the removal of surface defects than a variation of particle size. However, the upconversion efficiency is significantly enhanced due to a reduction in cubic crystal structure. Evidently, the upconversion efficiency is increased in the hexagonal phase. Furthermore, it is found that the annealing process also alters the elemental composition of the sample.

As a result, the fluorescence efficiency of Eu emissions can be enhanced by increasing the particles size, whereas it is difficult to vary the lifetimes. The upconversion efficiency can be increased by an increase in Er concentration and by thermal annealing, in which the crystal structure changes from cubic to hexagonal. The green-to-red ratio

of the multifunction material can be adjusted by changing crystal structure, varying the particle size and varying the elemental composition of the nanoparticles.

An upconversion energy transfer diagram of Er-, Eu-, and Yb-doped NaGdF<sub>4</sub> nanoparticles is proposed in Figure 4.3.25, which is based on the results obtained in Chapter 4.3.3 in combination with previous results from Wang.<sup>86,118,122</sup>

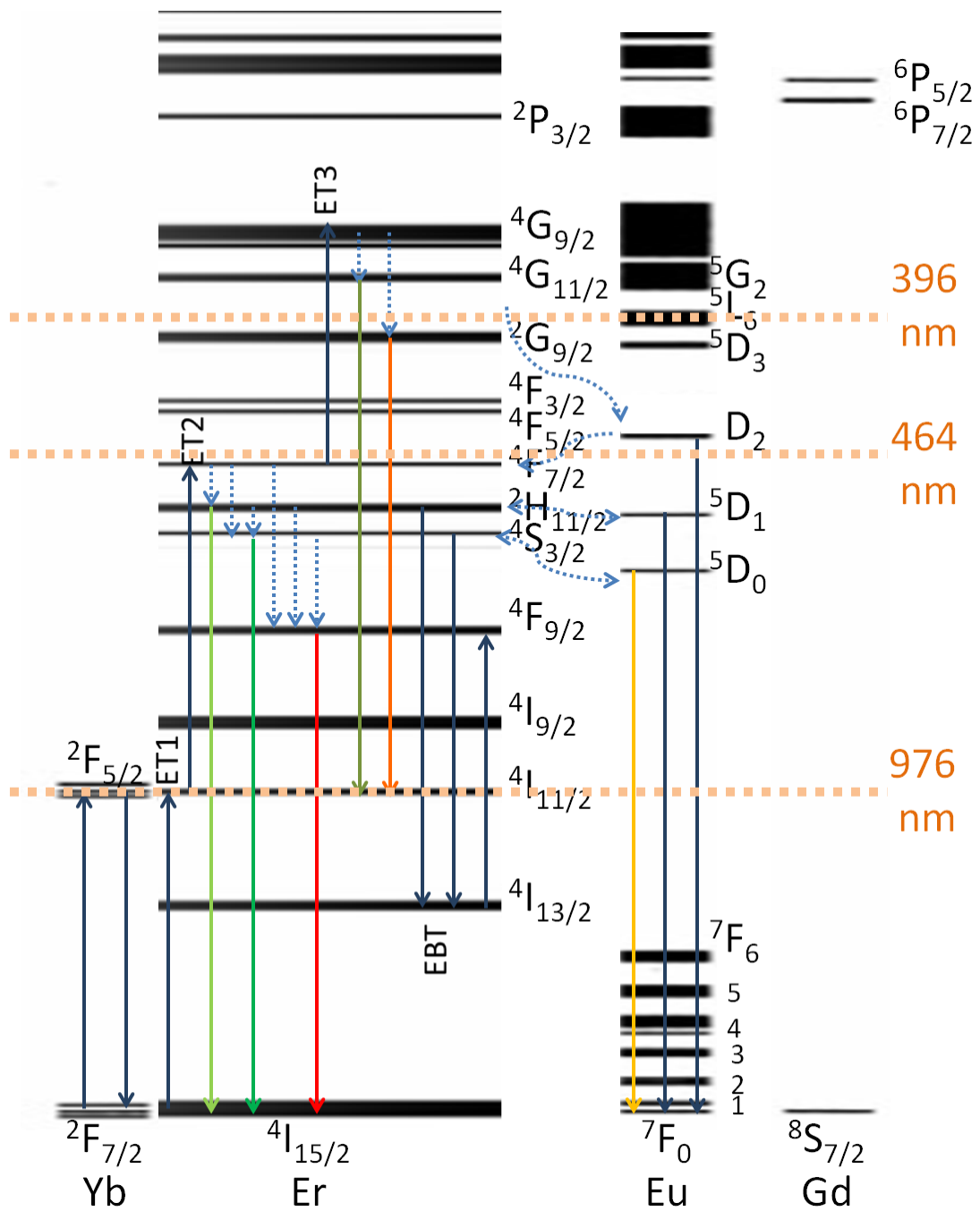


Figure 4.3.25: Simplified energy level diagrams of  $\text{Er}^{3+}$ ,  $\text{Eu}^{3+}$  and  $\text{Yb}^{3+}$  and possible energy transfer pathways in Er-, Eu-, and Yb-doped  $\text{NaGdF}_4$  nanoparticles. ET1, ET2 and ET3 are photons transferred from Yb to Er. EBT is energy back transfer which leads a decrease in green emission and enhances the red emission under the assistance of Yb ions. The dotted blue lines correspond to non-radiative energy transfer processes.

# Chapter 5

## Conclusions

This thesis focuses on the magnetic and optical properties of multifunctional lanthanide-based nanoparticles. Two different kinds of nanoparticle hosts are used. One is gadolinium oxide ( $\text{Gd}_2\text{O}_3$ ) and the other one is sodium gadolinium fluoride ( $\text{NaGdF}_4$ ). Both nanoparticle systems are doped with different lanthanide ions, such as Eu, Er, and Yb, for the purpose being multifunctional.

There are three main parts of the thesis: Chapter 4.1 is focused on the magnetic properties of  $\text{Gd}_2\text{O}_3$ -based nanoparticles, Chapter 4.2 is focused on the magnetic properties of  $\text{NaGdF}_4$ -based nanoparticles, and Chapter 4.3 is focused on the optical properties of  $\text{NaGdF}_4$ -based nanoparticles.

In Chapter 4.1, three different samples have been prepared for investigations on the magnetic properties of  $\text{Gd}_2\text{O}_3$ -based nanoparticles. These are undoped  $\text{Gd}_2\text{O}_3$  nanoparticles, unannealed 10% Eu-doped  $\text{Gd}_2\text{O}_3$  nanoparticles, and annealed 10% Eu-doped  $\text{Gd}_2\text{O}_3$  nanoparticles. All of these nanoparticles are in the size range smaller than 5 nm. These samples are characterized by the experimental methods of XAS, XMCD, and SQUID. The XAS results not only confirm the existence of Gd and Eu in the corresponding samples, but also show the oxidation states of these metals. The oxidation state of Gd is +3 whereas the oxidation states of Eu are both +2 and +3 in all samples. The XMCD spectra show a small XMCD effect at the Eu absorption edges for the Eu-doped  $\text{Gd}_2\text{O}_3$  samples. This is due to the non-magnetic character of  $\text{Eu}^{3+}$  which is the major oxidation state of Eu. The XMCD studies reveal that the doping agent Eu has no observable influence on the Gd spin magnetic moment but the orbital magnetic moment of Gd is decreased after the addition of Eu. This is possibly due to the elimination of Gd-Gd interactions. Because of the anti-parallel relation between the orbital magnetic moment and the spin magnetic moment of Gd, as calculated by sum rules, the total magnetic moment of Gd is increased after the addition of Eu as a dopant. An annealing process is able to increase both of the spin and orbital magnetic moments

of Gd. However, due to the less significant magnitude of the increased orbital magnetic moment compared to the increased spin magnetic moment, the total magnetic moment is increased after the annealing process. Unlike XAS and XMCD studies, which provide local and elemental-specific magnetic information of the samples, SQUID measures the magnetic properties of the whole samples. Based on the assumption that all elements except Gd ions have no magnetic contributions in SQUID measurements, effective magnetic moments obtained from SQUID confirm the total magnetic moments of Gd derived from XMCD sum rules.

In Chapter 4.2, two different samples have been prepared for investigations on the magnetic properties of NaGdF<sub>4</sub> nanoparticles. These are unannealed and annealed Er (0.002%)-, Eu (5%)-, and Yb (18%)-doped NaGd(77%)F<sub>4</sub> nanoparticles. They are in the size range of 15 nm. The SQUID results shows that an annealing process on these nanoparticles at 200 °C for 70 h is able to successfully enhance the magnitude of magnetization in the factor of 1.65. However, when such nanoparticles are applied as a MRI contrast agent, they show to have the potential to accelerate the T<sub>1</sub> relaxations, but they show even a larger potential to be used as a T<sub>2</sub>-weighted contrast agent. This is due to the large particles size and thus fewer Gd ions are located on the particle surface, which is required for being used as a suitable T<sub>1</sub>-weighted MRI contrast agent.

In Chapter 4.3, the optical studies of NaGdF<sub>4</sub>-based nanoparticles are discussed in three steps. Firstly, the influence of Eu as a dopant for enhancing the optical properties is discussed. Secondly, the different optical properties between Er and Eu on Er-, Eu-, and Yb-doped NaGdF<sub>4</sub> nanoparticles are distinguished. Thirdly, the possible route to alter the optical properties of these particles, such as by variations of different Er/Eu ratios, particles sizes, and annealing processes, are studied.

The studies of the dopant Eu effects on NaGdF<sub>4</sub> are investigated by comparisons between three samples: the undoped NaGdF<sub>4</sub>, 10% Eu-doped NaGdF<sub>4</sub>, and undoped NaEuF<sub>4</sub> samples. It is found that there is no fluorescence emission of undoped NaGdF<sub>4</sub> in the visible regime, and 10% of Eu ions yield 44% of the undoped NaEuF<sub>4</sub> fluorescence intensity. In addition, when Eu ions are contained in NaGdF<sub>4</sub> nanoparticles, the characteristic lifetime of Eu can be enhanced by a factor of 1.2. This study

demonstrates the strong fluorescence potential of Eu on Gd-containing multifunctional nanoparticles.

Furthermore, this work also shows that when the multifunctional nanomaterials containing Er (0.002%)-, Eu (2%)-, and Yb (18%)-doped NaGd(80%)F<sub>4</sub> nanoparticles are excited at UV regime, only Eu emissions are found and their lifetimes reach up to 6.5 ms, whereas when they are excited by IR light, only Er emissions are observable and their lifetimes reach only up to 0.1 ms. These results demonstrate that Er-, Eu-, and Yb-doped NaGdF<sub>4</sub> nanoparticles are multifunctional materials with both, downconversion and upconversion abilities. This material is not only ideal for being a fluorescent probe which has extremely long lifetimes for long-term tracking using different excitation wavelengths, but there is also the potential to be used as an energy sensor which shows different emissions when different photon energies are used. Furthermore, the optical properties of this multifunctional material that are influenced by the Er-to-Eu ratios, the particles size, and the annealing conditions, have been systematically investigated in this Chapter.

It is found that the upconversion emission intensities increase when the Er content is increased and the Er-to-Eu ratio has no influence on this property. The red-to-green ratio of emission bands of these particles is related to the (Yb + Eu)-to-(Er + Eu) ratio. Lifetimes of this material are altered by different Er-to-Eu ratios and it is found that the lifetimes of the red emission band are increased by increasing Er-to-Eu ratios because of the enhanced back transfer of energy.

For samples with the same elemental composition, variation of the particles size shows that large particles show stronger fluorescence intensity. Regarding upconversion properties in Er spectra, the intensities were not varied as much as observed for Eu fluorescence spectra, but the lifetimes of the large particles sample are  $1.8 \pm 0.2$  times longer than for the small particles. Also, the change in green-to-red ratio in upconversion spectra implies that the particles size has an influence on the crystal structure. The lifetimes in both Eu fluorescence spectra and Er upconversion spectra can be increased by enlarging the particles size, which is essentially due to the reduced influence of surface defect-sites.

The annealing process does not change the lifetimes and intensities in the fluorescence spectra. However, the upconversion and its lifetimes are significantly enhanced due to a reduction in cubic crystal structure.

Briefly, the fluorescence efficiency of Eu emissions can be enhanced by increasing particle sizes but the lifetimes are more difficult to change. However, the lifetimes of Eu emissions are sufficiently long, reaching up to 6.5 ms. The upconversion efficiency can be increased by an increase in Er concentration, by increasing the particles size, or by applying a thermal annealing on the particles, in which the crystal structure changes from a cubic to a hexagonal lattice. The lifetimes of upconversion emissions can be increased by both increasing particles sizes and by thermal annealing. The green-to-red ratio of the multifunctional nanomaterial can be adjusted by varying the particle size and by varying the elemental composition of the nanoparticles.

As a result, the Er (0.002%)-, Eu (2%)-, and Yb (18%)-doped NaGd(80%)F<sub>4</sub> nanoparticles combines all characters to be a MRI contrast agent, a downconversion material, and an upconversion material.

## Summary

This work develops a new class of multifunctional nanoparticles which can be used not only as magnetic resonance imaging (MRI) contrast agents but also as dual-emission fluorescent agents that can be excited by both ultraviolet and near infrared radiation. Nanoparticles containing Gd, Eu, Er, and Yb are investigated regarding their magnetic and optical properties.

Regarding the magnetic properties of nanoparticles, this work shows that an annealing process is able to enhance the magnetization on two different kinds of nanoparticles, Eu-doped  $Gd_2O_3$  and Er-, Eu-, and Yb-doped  $NaGdF_4$ , as probed by the methods of superconducting quantum interference device (SQUID). In addition, orbital and spin magnetic moments of Gd ions within Eu-doped  $Gd_2O_3$  samples are determined by sum rules according to the results obtained from X-ray magnetic circular dichroism (XMCD). The results indicate that the orbital magnetic moment and the spin magnetic moment of Gd ions are anti-parallel to each other, and an annealing process enhances both, the spin and orbital magnetic moments. In addition, a comparison on relaxometry measurements between Magnevist<sup>®</sup> and Er-, Eu-, and Yb-doped  $NaGdF_4$  nanoparticles shows that the Er-, Eu-, and Yb-doped  $NaGdF_4$  nanoparticles have potential to be a  $T_1$ -weighted MRI contrast agent. However, due to the particle size of the sample under study ( $16\pm 3$  nm), this sample is rather a better  $T_2$ -weighted MRI contrast agent than a  $T_1$ -weighted MRI contrast agent.

Regarding the optical properties of the nanoparticles under study, the Er-, Eu-, and Yb-doped  $NaGdF_4$  nanoparticles can be excited by both ultraviolet and near infrared radiations. Ultraviolet radiation is able to excite Eu ions which gives rise to yellow and red emissions whereas near infrared radiation is able to excite Er ions by an energy transfer from Yb ions, so that the Er ions show green and red emissions. The emission lifetime of Eu reaches up to 6.5 ms and that of Er is about 1 ms, but both are much longer than is observed for quantum dots and organic dyes. The fluorescence efficiency of Eu emissions can be enhanced by increasing the particles size, but their lifetimes are

hard to be further increased. The upconversion efficiency can be enhanced by an increase in Er concentration or by thermal annealing, in which the crystal structure changes from cubic to hexagonal. The green-to-red ratio of this multifunction material can be adjusted by changing the crystal structure, varying the particle size, and varying the elemental composition of the nanoparticles.

# Zusammenfassung

In dieser Arbeit wird die Entwicklung neuartiger Nanopartikel und deren Eigenschaften vorgestellt. Diese kann man nicht nur als MRI-Kontrastmittel einsetzen, sondern sie können auch als Doppemissionsfluoreszenzmittel dienen, das sowohl von ultraviolettem als auch von nahem Infrarot-Licht angeregt werden kann. Die Gd, Eu, Er sowie Yb enthaltenden Nanopartikel wurden bezüglich ihrer magnetischen und optischen Eigenschaften untersucht.

Bezüglich der magnetischen Eigenschaften der im Rahmen dieser Arbeit untersuchten Nanopartikel konnte gezeigt werden, dass die thermische Behandlung der Partikel die Magnetisierung verstärkt. Dies trifft vor allem für die Eu-dotierten  $Gd_2O_3$  und Er-, Eu- sowie Yb-dotierten  $NaGdF_4$  - Partikel zu, wofür SQUID-Experimente zum Einsatz kamen. Ebenso wurden die magnetischen Bahn- und Spinmomente von Gd-Ionen innerhalb der Eu-dotierten  $Gd_2O_3$ -Partikel mittels zirkularem magnetischem Röntgenzirkulardichroismus unter Nutzung von Summenregeln bestimmt. Das Ergebnis zeigt, dass die magnetischen Bahn- und Spinmomente von Gd-Ionen antiparallel zueinander einstellen, wobei die thermische Behandlung der Proben zu einer Verstärkung der magnetischen Bahn- und Spinmomente führt. Darüber hinaus wurden relaxometrische Messungen der im Rahmen dieser Arbeit hergestellten Proben im Vergleich zum kommerziellen Magnevist<sup>®</sup> durchgeführt. Es zeigt sich einerseits, dass Er-, Eu- sowie Yb-dotiertes  $NaGdF_4$ -Nanopartikel als,  $T_1$ -gewichtete MRI-Kontrastmittel einsetzbar sind. Andererseits kann die untersuchte Probe aufgrund der Partikelgröße ( $16 \pm 3$  nm) ebenso als ein verbessertes  $T_2$ -gewichtetes MRI-Kontrastmittel genutzt werden.

Bezüglich der optischen Eigenschaften können Er-, Eu- und Yb-dotiertes  $NaGdF_4$  Nanopartikel sowohl von UV-Licht als auch durch nahe Infrarotstrahlung angeregt werden. Dabei kann das UV-Licht die Eu-Ionen anregen, so dass sie gelbe und rote Emissionen liefern. Im Fall der Er-Ionen können diese im nahen Infrarot-Bereich nach Energieübertragung von Yb-Ionen angeregt werden, so dass die Er-Ionen grüne und rote Emissionen emittieren können. Die Lebensdauer der Emission von Eu beträgt bis zu 6,5

ms, die von Er ca. 1 ms, was viel länger ist als die von Quantenpunkten und organischen Farbstoffen. Die Fluoreszenzausbeute der Eu-Emissionen lässt sich durch die Vergrößerung der Partikel erhöhen, ohne aber die Lebensdauer zu verlängern. Die Upconversion-Ausbeute kann durch eine Erhöhung der Er-Konzentration oder durch thermische Behandlung erhöht werden, wobei sich die Kristallstruktur von einem kubischen zu einer hexagonalem Gitter ändert. Das Grün-zu-Rot-Emissionsverhältnis dieses Multifunktionsmaterials kann durch Änderung der Kristallstruktur, die Partikelgröße sowie durch Variation der elementaren Zusammensetzung der Nanopartikel eingestellt werden.

## References

- 1 H. Xing, X. Zheng, Q. Ren, W. Bu, W. Ge, Q. Xiao, S. Zhang, C. Wei, H. Qu, Z. Wang, Y. Hua, L. Zhou, W. Peng, K. Zhao, and J. Shi, *Sci. Rep.* 3, 1751 (2013).
- 2 H. B. Na, I. C. Song, and T. Hyeon, *Adv. Mater.* 21, 2133 (2009).
- 3 H. Chen, D. C. Colvin, B. Qi, T. Moore, J. He, O. T. Mefford, F. Alexis, J. C. Gore, and J. N. Anker, *J. Mater. Chem.* 22, 12802 (2012).
- 4 L. Sudheendra, G. K. Das, C. Q. Li, D. Stark, J. Cena, S. Cherry, and I. M. Kennedy, *Chem. Mater.* 26, 1881 (2014).
- 5 G. Chen, H. Qju, P. N. Prasad, and X. Chen, *Chem. Rev.* 114, 5161 (2014).
- 6 H. Guo, Z. Q. Li, H. S. Qian, Y. Hu, and I. N. Muhammad, *Nanotechnology* 21, 6 (2010).
- 7 N. J. J. Johnson, W. Oakden, G. J. Stanisiz, R. S. Prosser, and F. C. J. M. van Veggel, *Chem. Mater.* 23, 3714 (2011).
- 8 F. Li, W. Gu, H. Wang, Y. Qi, Y. Deng, N. Xiao, Y. Liu, Q. Xu, and L. Ye, *R. Soc. Chem. Adv.* 3, 5386 (2013).
- 9 C. Dong, J. Pichaandi, T. Regier, and F. van Veggel, *J. Phys. Chem. C* 115, 15950 (2011).
- 10 R. Nagarajan, *Nanoparticles: Building Blocks for Nanotechnology* (American Chemical Society, Washington, DC, 2008).
- 11 S. P. Gubin, *Magnetic nanoparticles* (Wiley-VCH Verlag GmbH & Co. KGaA, Weinheim, 2009).
- 12 S. Shylesh, V. Schunemann, and W. R. Thiel, *Angew. Chem. Int. Ed.* 49, 3428 (2010).
- 13 A. K. Gupta and M. Gupta, *Biomaterials* 26, 3995 (2005).
- 14 S. H. Sun, *Adv. Mater.* 18, 393 (2006).
- 15 A.-H. Lu, E. L. Salabas, and F. Schueth, *Angew. Chem. Int. Ed.* 46, 1222 (2007).
- 16 T. Iwaki, Y. Kakihara, T. Toda, M. Abdullah, and K. Okuyama, *J. Appl. Phys.* 94, 6807 (2003).
- 17 F. Bodker, S. Morup, and S. Linderoth, *Phys. Rev. Lett.* 72, 282 (1994).

- 18 D. Wachenschwanz, W. Jiang, E. Roddick, A. Homola, P. Dorsey, B. Harper, D. Treves, and C. Bajorek, *IEEE Trans. Magn.* 41, 670 (2005).
- 19 P. M. Paulus, H. Bonnemann, A. M. van der Kraan, F. Luis, J. Sinzig, and L. J. de Jongh, *Eur. Phys. J. D* 9, 501 (1999).
- 20 M. J. Ruedas-Rama, J. D. Walters, A. Orte, and E. A. H. Hall, *Anal. Chim. Acta* 751, 1 (2012).
- 21 M. J. Murcia and C. A. Naumann, *Biofunctionalization of Fluorescent Nanoparticles in Nanotechnologies for the Life Sciences*, edited by C. S. S. R. Kumar (Wiley-VCH Verlag GmbH & Co. KGaA, Weinheim, 2005).
- 22 T. J. Bukowski and J. H. Simmons, *Crit. Rev. Solid State Mater. Sci.* 27, 119 (2002).
- 23 Y. Zhang and T.-H. Wang, *Theranostics* 2, 631 (2012).
- 24 J. Liu, X. Yang, X. He, K. Wang, Q. Wang, Q. Guo, H. Shi, J. Huang, and X. Huo, *Sci China Chem.* 54, 1157 (2011).
- 25 F. Meiser, C. Cortez, and F. Caruso, *Angew. Chem. Int. Ed.* 43, 5954 (2004).
- 26 R. A. Poorley, *RadioGraphics* 25, 1087 (2005).
- 27 S. Månsson, A. Björnerud, *Physical principles of medical imaging by nuclear magnetic resonance in The chemistry of contrast agents in medical magnetic resonance imaging*, edited by A. E. Merbach, E. Toth (Wiley, Chichester, 2001)
- 28 P. Caravan, J. J. Ellison, T. J. McMurry, *Chem. Rev.* 99, 2293 (1999).
- 29 D. Hao, T. Ai, F. Goerner, X. Hu, V. M. Runge, and M. Tweedle, *J. Magn. Reson. Imaging* 36, 1060 (2012).
- 30 J. W. Lichtman and J. A. Conchello, *Nat. Methods* 2, 910 (2005).
- 31 U. Noomnarm and R. M. Clegg, *Photosynth. Res.* 101, 181 (2009).
- 32 M. Sauer, J. Hofkens, and J. Enderlein, *Handbook of Fluorescence Spectroscopy and Imaging: From Ensemble to Single Molecules* (Wiley-VCH Verlag GmbH & Co. KGaA, Weinheim, 2011).
- 33 M. Kasha, *Chem. Rev.* 41, 401 (1947).
- 34 P. A. Jursinic, *Delayed Fluorescence-Current Concept and Status in Light emission by plants and bacteria*, edited by J. Ames (Elsevier Academic Press, Orlando, 1986).
- 35 A. Hayer, H. Bassler, B. Falk, and S. Schrader, *J. Phys. Chem. A* 106, 11045 (2002).

- 36 A. D. McNaught, A. Wilkinson, *Compendium of Chemical Terminology* (Blackwell Scientific Publications, Oxford, **1997**).
- 37 F. Auzel, *Chem. Rev.* 104, 139 (**2004**).
- 38 R. Scheeps, *Prog. Quant. Electron.* 20, 271 (**1996**).
- 39 M. V. DaCosta, S. Doughan, Y. Han, and U. J. Krull, *Anal. Chim. Acta* 832, 1 (**2014**).
- 40 F. E. Auzel, *Proc. IEEE* 61, 758 (**1973**).
- 41 F. Wang, R. Deng, J. Wang, Q. Wang, Y. Han, H. Zhu, X. Chen, and X. Liu, *Nat. Mater.* 10, 968 (**2011**).
- 42 K. N. Shinde, S. J. Dhoble, H. C. Swart, and K. Park, *Phosphate Phosphors for Solid-State Lighting* (Springer-Verlag, Berlin, **2012**).
- 43 M. Haase and H. Schaefer, *Angew. Chem. Int. Ed.* 50, 5808 (**2011**).
- 44 D. A. Atwood, *The rare earth elements- fundamentals and applications* (John Wiley & Sons Ltd., Oxford, **2012**).
- 45 H. Liang, G. Chen, L. Li, Y. Liu, F. Qin, and Z. Zhang, *Opt. Commun.* 282, 3028 (**2009**).
- 46 Y. Dwivedi, S. N. Thakur, and S. B. Rai, *App. Phys. B* 89, 45 (**2007**).
- 47 A. A. Pushkar, T. V. Uvarova, and V. V. Kiiko, *Opt. Spectrosc.* 111, 273 (**2011**).
- 48 M. Tinkham, *Introduction to superconductivity* (McGraw-Hill, New York, **1975**).
- 49 J. Bardeen, *Phys. Rev.* 97, 1724 (**1955**).
- 50 M. Mcelfresh, *Fundamentals of magnetism and magnetic measurements featuring Quantum Design's magnetic property measurement system* (Quantum Design, Purdue University, **1994**).
- 51 T. Mallah, *The Quantum Design Magnetic Property Measurement System*. (Université Paris-Sud, Paris, **2014**).
- 52 J. I. Hoppee, *J. Chem. Educ.* 49, 505 (**1972**).
- 53 E. C. Stoner, *Rep. Prog. Phys.* 13, 83 (**1950**).
- 54 R. Reininger, J. C. Woicik, S. L. Hulbert, and D. A. Fischer, *Nucl. Instrum. Meth. A* 649, 49 (**2011**).
- 55 J. E. Penner-Hahn, *X-ray Absorption Spectroscopy* (Wiley Online Library, **2005**).

- 56 P. A. Lee, P. H. Citrin, P. Eisenberger, and B. M. Kincaid, *Rev. Mod. Phys.* 53, 769 (1981).
- 57 R. C. Nelson and J. T. Miller, *Catal. Sci. Tech.* 2, 461 (2012).
- 58 J. G. Chen, *Surf. Sci. Rep.* 30, 1 (1997).
- 59 H. Saisho, Y. Gohshi, *Applications of Synchrotron Radiation to Materials Analysis* (Elsevier Science, Amsterdam, 1996).
- 60 H. Wende and C. Antoniak, *X-Ray Magnetic Dichroism* (Springer, Berlin, 2010).
- 61 T. E. Westre, P. Kennepohl, J. G. DeWitt, B. Hedman, K. O. Hodgson, and E. I. Solomon, *J. Am. Chem. Soc.* 119, 6297 (1997).
- 62 D. Cahen, A. Kahn, and E. Umbach, *Mater. Today* 8, 32 (2005).
- 63 J. Stöhr, *J. Magn. Magn. Mater.* 200, 470 (1999).
- 64 T. Funk, A. Deb, S. J. George, H. X. Wang, and S. P. Cramer, *Coord. Chem. Rev.* 249, 3 (2005).
- 65 J. Stöhr, *J. Electron. Spectrosc. Relat. Phenom.* 75, 253 (1995).
- 66 R. M. Petoral, Jr., F. Soderlind, A. Klasson, A. Suska, M. A. Fortin, N. Abrikosova, L. Selegard, P.-O. Kall, M. Engstrom, and K. Uvdal, *J. Phys. Chem. C* 113, 6913 (2009).
- 67 J.-L. Bridot, A.-C. Faure, S. Laurent, C. Riviere, C. Billotey, B. Hiba, M. Janier, V. Josserand, J.-L. Coll, L. Vander Elst, R. Muller, S. Roux, P. Perriat, and O. Tillement, *J. Am. Chem. Soc.* 129, 5076 (2007).
- 68 F. Wang, Y. Han, C. S. Lim, Y. Lu, J. Wang, J. Xu, H. Chen, C. Zhang, M. Hong, and X. Liu, *Nature* 463, 1061 (2010).
- 69 R. Heathcote, J. A. S. Howell, N. Jennings, D. Cartlidge, L. Cobden, S. Coles, and M. Hursthouse, *Dalton Trans.* 13, 1309 (2007).
- 70 J. J. Shephard, S. A. Dickie, and A. J. McQuillan, *Langmuir* 26, 4048 (2010).
- 71 W. Liu, A. B. Greytak, J. Lee, C. R. Wong, J. Park, L. F. Marshall, W. Jiang, P. N. Curtin, A. Y. Ting, D. G. Nocera, D. Fukumura, R. K. Jain, and M. G. Bawendi, *J. Am. Chem. Soc.* 132, 472 (2010).
- 72 J.-C. Boyer, M.-P. Manseau, J. I. Murray, and F. C. J. M. van Veggel, *Langmuir* 26, 1157 (2010).
- 73 T. J. Kim, K. S. Chae, Y. Chang, and G. H. Lee, *Curr. Top. Med. Chem.* 13, 422 (2013).

- 74 D. Magana, S. C. Perera, A. G. Harter, N. S. Dalal, and G. F. Strouse, *J. Am. Chem. Soc.* 128, 2931 (2006).
- 75 E. A. Merritt, *X-ray absorption edges* (Biomolecular Structure Center at UW, Washington, 2010).
- 76 C. Jeynes and G. W. Grime, *Atomic Excitation Exploited By Energetic-Beam Characterization Methods in Characterization of Materials*, edited by (Wiley Online Library, Guildford, 2012).
- 77 G. Kaindl, G. Kalkowski, W. D. Brewer, B. Perscheid, and F. Holtzberg, *J. Appl. Phys.* 55, 1910 (1984).
- 78 B. T. Thole, G. Vanderlaan, J. C. Fuggle, G. A. Sawatzky, R. C. Karnatak, and J. M. Esteve, *Phys. Rev. B* 32, 5107 (1985).
- 79 S. Qiao, A. Kimura, H. Adachi, T. Kambe, K. Yoshikawa, K. Yaji, C. Hirai, H. Sato, Y. Takeda, H. Namatame, M. Taniguchi, A. Tanaka, T. Muro, S. Imada, and S. Suga, *Physica B* 351, 333 (2004).
- 80 D. R. Lee, Y. Choi, C. Y. You, J. C. Lang, D. Haskel, G. Srajer, V. Metlushko, B. Ilic, and S. D. Bader, *Appl. Phys. Lett.* 81, 4997 (2002).
- 81 M. Martins, M. Reif, L. Glaser, and W. Wurth, *Eur. Phys. J. D* 45, 539 (2007).
- 82 S. Qiao, A. Kimura, H. Adachi, K. Iori, K. Miyamoto, T. Xie, H. Namatame, M. Taniguchi, A. Tanaka, T. Muro, S. Imada, and S. Suga, *Phys. Rev. B* 70, 134418 (2004).
- 83 L. Du`o, M. Finazzi, and F. Ciccacci, *Magnetic Properties of Antiferromagnetic Oxide Material* (Wiley-VCH Verlag GmbH & Co. KGaA, Weinheim, 2010).
- 84 P. Carra, B. T. Thole, M. Altarelli, and X. D. Wang, *Phys. Rev. Lett.* 70, 694 (1993).
- 85 S. Mangin, C. Bellouard, S. Andrieu, F. Montaigne, P. Ohresser, N. B. Brookes, and B. Barbara, *Phys. Rev. B* 70, 014401 (2004).
- 86 R. Hull, *Spectroscopic Properties of Rare Earths in Optical Materials* (Springer-Verlag, Berlin, 2005).
- 87 J. Stöhr and H. König, *Phys. Rev. Lett.* 75, 3748 (1995).
- 88 M. Petersen, J. Hafner, and M. Marsman, *J. Phys. Condens. Matter* 18, 7021 (2006).
- 89 S. Simon, I. G. Deac, and M. Coldea, *J. Optoelectron. Adv. Mater.* 9, 583 (2007).
- 90 S.-H. Kung, *Annealing effects on Mn-doped CdSe nanoparticles*, (Freie Universität Berlin, Berlin, 2009).

- 91 T. Nakamura, T. Hirono, T. Kinoshita, Y. Narumi, M. Hayashi, H. Nojiri, A. Mitsuda, H. Wada, K. Kodama, K. Kindo, and A. Kotani, *J. Phys. Soc. Jpn.* 81, 103705 (2012).
- 92 V. Kachkanov, M. J. Wallace, G. van der Laan, S. S. Dhesi, S. A. Cavill, Y. Fujiwara, and K. P. O'Donnell, *Sci. Rep.* 2, 969 (2012).
- 93 R. S. Selinsky, D. J. Keavney, M. J. Bierman, and S. Jin, *Appl. Phys. Lett.* 95, 202501 (2009).
- 94 B. J. Ruck, H. J. Trodahl, J. H. Richter, J. C. Cezar, F. Wilhelm, A. Rogalev, V. N. Antonov, B. Do Le, and C. Meyer, *Phys. Rev. B* 83, 174404 (2011).
- 95 V. V. Krishnamurthy, D. J. Keavney, D. Haskel, J. C. Lang, G. Srajer, B. C. Sales, D. G. Mandrus, and J. L. Robertson, *Phys. Rev. B* 79, 014426 (2009).
- 96 H. Ott, S. J. Heise, R. Sutarto, Z. Hu, C. F. Chang, H. H. Hsieh, H. J. Lin, C. T. Chen, and L. H. Tjeng, *Phys. Rev. B* 73, 094407 (2006).
- 97 C.-C. Huang, T.-Y. Liu, C.-H. Su, Y.-W. Lo, J.-H. Chen, and C.-S. Yeh, *Chem. Mater.* 20, 3840 (2008).
- 98 G. H. Jaffari, A. Ceylan, H. P. Bui, T. P. Beebe, Jr., S. Ozcan, and S. I. Shah, *J. Phys. Condens. Matter* 24, 336004 (2012).
- 99 T. Trindade, A. L. Daniel-Da-Silva, *Biofunctional Composites of Polysaccharides Containing Inorganic Nanoparticles* in *Advances in Nanocomposite Technology*, edited by A. Hashim (Intech, 2011).
- 100 H. J. Huang, S. H. Yang, and X. X. Zhang, *J. Phys. Chem. B* 104, 1473 (2000).
- 101 W. M. Haynes, *CRC Handbook of Chemistry and Physics*, 93 ed. (CRC Press, 2012).
- 102 S. Aime, M. Botta, and E. Terreno, *Adv. Inorg. Chem.* 57, 173 (2005).
- 103 C. Dong, A. Korinek, B. Blasiak, B. Tomanek, and F. C. J. M. van Veggel, *Chem. Mater.* 24, 1297 (2012).
- 104 C. Zhang, L. Sun, Y. Zhang, and C. Yan, *J. Rare Earth* 28, 807 (2010).
- 105 M. Lin, Y. Zhao, S. Q. Wang, M. Liu, Z. F. Duan, Y. M. Chen, F. Li, F. Xu, and T. J. Lu, *Biotechnol. Adv.* 30, 1551 (2012).
- 106 W. G. J. H. M. van Sark, J. de Wild, J. K. Rath, A. Meijerink, and R. E. I. Schropp, *Anoscale Res. Lett.* 8, 81 (2013).
- 107 J. C. G. Bunzli and C. Piguet, *Chem. Soc. Rev.* 34, 1048 (2005).

- 108 P. Ptacek, H. Schafer, K. Kompe, and M. Haase, *Adv. Funct. Mater.* 17, 3843  
(2007).
- 109 M. Dejneka, E. Snitzer, and R. E. Riman, *J. Lumin.* 65, 227 (1995).
- 110 Y. Zhang and X. Liu, *Nat. Nanotech.* 8, 702 (2013).
- 111 X. Li, B. Chen, R. Shen, H. Zhong, L. Cheng, J. Sun, J. Zhang, H. Zhong, Y.  
Tian, and G. Du, *J. Phys. D* 44, 335403 (2011).
- 112 Vanuiter.Lg and L. F. Johnson, *J. Chem. Phys.* 44, 3514 (1966).
- 113 G. Chen, T. Y. Ohulchanskyy, W. C. Law, H. Agren, and P. N. Prasad,  
*Nanoscale* 3, 2003 (2011).
- 114 F. Song, G. Y. Zhang, M. R. Shang, H. Tan, J. Yang, and F. Z. Meng, *Appl.*  
*Phys. Lett.* 79, 1748 (2001).
- 115 A. K. Hagan and T. Zuchner, *Anal. Bioanal. Chem.* 400, 2847 (2011).
- 116 I. Hemmila, S. Dakubu, V. M. Mukkala, H. Siitari, and T. Lovgren, *Anal.*  
*Biochem.* 137, 335 (1984).
- 117 J. R. Lakowicz, *Principles of Fluorescence Spectroscopy* (Springer, New York,  
2006).
- 118 L. Wang, X. Xue, H. Chen, D. Zhao, and W. Qin, *Chem. Phys. Lett.* 485, 183  
(2010).
- 119 D. K. Sardar, K. L. Nash, R. M. Yow, and J. B. Gruber, *J. Appl. Phys.* 101,  
113115 (2007).
- 120 M. Y. Berezin and S. Achilefu, *Chem. Rev.* 110, 2641 (2010).
- 121 F. Wang and X. Liu, *Chem. Soc. Rev.* 38, 976 (2009).
- 122 Z. H. Bai, M. Fujii, K. Imakita, and S. Hayashi, *Microporous Mesoporous Mater.*  
173, 43 (2013).
- 123 L. F. Liang, H. Wu, H. L. Hu, M. M. Wu, and Q. Su, *J. Alloys Compd.* 368, 94  
(2004).
- 124 Y. Dwivedi, A. Rai, and S. B. Rai, *J. Lumin.* 129, 629 (2009).
- 125 Y. Q. Sheng, J. Liu, L. L. Xu, D. Zhai, Z. G. Zhang, and W. W. Cao, *Solid State*  
*Commun.* 150, 1048 (2010).
- 126 J. F. Suyver, J. Grimm, M. K. van Veen, D. Biner, K. W. Kramer, and H. U.  
Gudel, *J. Lumin.* 117, 1 (2006).

- <sup>127</sup> C. Liu, Z. Gao, J. Zeng, Y. Hou, F. Fang, Y. Li, R. Qiao, L. Shen, H. Lei, W. Yang, and M. Gao, *Acs Nano* 7, 7227 (2013).
- <sup>128</sup> D. Magde, R. Wong, and P. G. Seybold, *Photochem. Photobiol.* 75, 327 (2002).
- <sup>129</sup> J. Shan and Y. Ju, *App. Phys. Lett.* 91, 123103 (2007).
- <sup>130</sup> J. Zhao, Z. Lu, Y. Yin, C. McRae, J. A. Piper, J. M. Dawes, D. Jin, and E. M. Goldys, *Nanoscale* 5, 944 (2013).
- <sup>131</sup> S.-N. Shan, X.-Y. Wang, and N.-Q. Jia, *Nanoscale Res. Lett.* 6, 539 (2011).
- <sup>132</sup> P. Sahu and B. L. V. Prasad, *Langmuir* 30, 10143 (2014).